EFFICIENT CONTINUOUS ELECTROKINETIC DEWATERING AND IMPEDANCE
RESPONSE OF INTERDIGITATED ELECTRODES

By

ARTHUR DIZON

To my parents and my wife

ACKNOWLEDGMENTS

TABLE OF CONTENTS

LIST OF TABLES

LIST OF FIGURES

13

LIST OF SYMBOLS

Roman

A_{IDE} interdigitated electrode area in cm^2

a geometric constant for continuous dewatering, dimensionless

C capacitance, $\mathrm{F/cm}^2$

C_0 initial cost $\$/\mathrm{m}^2$

C_{annual} annualized cost, $\$/\mathrm{year}$

C_{cap} capital cost $\%/\mathrm{metric\ ton}$

C_{dl} double-layer capacitance, $\mathrm{F/cm}^2$

C_{op} operational cost, $\$/\mathrm{metric\ ton}$

C_{total} total cost, $\$/\mathrm{metric\ ton}$

C_{v} compressibility coefficient, cm^2/s

c_i concentration of species i, M

$c_{i\infty}$ bulk concentration of species i, M

D_i diffusion coefficient of species i cm^2/s

d_1 feed-side electrode gap length, cm

d_2 collection-side electrode gap length, cm

d_{r} dimensionless electrode gap ratio

$\mathbf{E}$ electric field vector, V/cm

E_{req} energy per dry mass of clay kWh/metric ton

F   Faraday's constant 96485.332 C/mol

f frequency, Hz

$\mathbf{f}$ body force vector, $\mathrm{N/m}^3$

f_{c} characteristic frequency, Hz

g gravitational acceleration 9.80665 $\mathrm{m/s}^2$

H electrode height, cm

H_{dom} domain height, $\mu\mathrm{m}$

H_u unyielded clay height, cm

h distance between electrodes, cm

I average total current, A

I_max maximum current, A

i interest rate, %

$\mathbf{i}$ current density vector A/m^2

K frequency, dimensionless

K_cell electrical cell constant, cm^{-1}

k permeability, cm/s

k_0 yield strength intercept, dimensionless

k_e electro-osmotic permeability cm^2/s V

k_τ yield strength slope constant wt.%$^{-1}$

L electrode length, cm

m wet-clay production rate kg/h m^2

m_C extrapolation slope for capacitance in Fμm$^{n_\mathrm{C}}$/cm^2

m_R extrapolation slope for resistance, Ωcm$^2\mu$m$^{n_\mathrm{R}}$

$\mathbf{N}_i$ molar flux of species i, mol/cm^2 s

n number of years

n_C extrapolation exponent for capacitance, dimensionless

n_IDE number of digits of an interdigitated electrode

n_R extrapolation exponent for resistance, dimensionless

p pressure, N/m^2

p_k characteristic consolidation pressure, N/m^2

p_c characteristic consolidation pressure, N/m^2

p_e characteristic electro-osmotic pressure, N/m^2

p_s solids-phase volume-averaged pressure, N/m^2

Q constant-phase element coefficient, s$^\alpha$/Ωcm^2

q_{in} volumetric feed rate, cm^3/s

R   universal gas constant 8.314 J/mol K

R_{e} ohmic resistance, Ω/cm^2

ΔR_{e} difference in ohmic resistance, Ω/cm^2

r_0 radius, cm

s maximum surface element size, μm

T temperature, K

u excess pore pressure N/m^2

u_i ionic mobility of species i, s mol/kg

V volume between electrodes, cm^3

$\mathbf{v}$ velocity vector, cm/s

v_{belt} conveyor belt speed cm/min

v_{e} electro-osmotic velocity cm/s

v_{h} hydraulic velocity, cm/s

v_{ℓ} liquid velocity, cm/s

V_{max} maximum electrical potential, V

w_{c} solids content, wt.%

x_{eff} effective value of property x

x_{in} property x of feed clay

x_{out} property x of product cake

$\langle x \rangle$ average of x

$\overline{x}$ steady-state variable x

$\tilde{x}$ oscillating variable x

$\text{Im}\{x\}$ imaginary part of x

$\text{Re}\{x\}$ real part of x

W electrode width, cm

$|Z|$ modulus of Z, Ωcm^2

Z_r real part of Z $\Omega\mathrm{cm}^2$

Z_j imaginary part of Z $\Omega\mathrm{cm}^2$

z_i charge number of species i

Greek

α constant-phase element exponent, dimensionless

γ coefficient of effective electrode surface area, dimensionless

γ_w unit weight of water, $\mathrm{N/m}^3$

δ characteristic dimension, $\mu\mathrm{m}$

ϵ porosity, dimensionless

ϵ_r relative dielectric constant, dimensionless

ϵ_0 permittivity of vacuum, 8.854×10^{-14} F/cm

ϵ_∞ limiting porosity, dimensionless

ζ dimensionless height

η dimensionless length

κ conductivity, S/cm

λ Debye length, nm

ξ dummy variable

ρ_ℓ liquid density, cm/s

ρ_e charge density, $\mathrm{C/m}^3$

ρ_s dry-clay density, $\mathrm{g/cm}^3$

ρ_w density of water, $\mathrm{g/cm}^3$

ρ_m mass-averaged clay-water density, $\mathrm{g/cm}^3$

σ' effective stress, Pa

σ total stress, Pa

τ stress tensor, Pa

τ	dimensionless time
τ_0	yield strength, Pa
τ_r	residence time, h
τ_c	time constant of compressibility, s
Φ	electrical potential, V
φ	phase angle, degrees
ψ	dimensionless excess pore pressure
ω	angular frequency, rad/s

Abstract of Dissertation Presented to the Graduate School
of the University of Florida in Partial Fulfillment of the
Requirements for the Degree of Doctor of Philosophy

EFFICIENT CONTINUOUS ELECTROKINETIC DEWATERING AND IMPEDANCE
RESPONSE OF INTERDIGITATED ELECTRODES

By

Arthur Dizon

August 2018

Chair: Mark E. Orazem
Major: Chemical Engineering

Mathematical modeling of electrochemical processes provides insight into physical mechanisms and spurs the development of new technologies. The first example in the dissertation is the development of a continuous electrokinetic dewatering (EKD) process for the solid-liquid separation of a dilute effluent clay-water effluent associated with phosphate mining. The second is the study of interdigitated micro-electrodes. These micro-electrodes have applications as chemical sensors due to their high sensitivity and diminutive size which allows measurement of small sample sizes.

The objective of this research was to develop an efficient EKD process for phosphatic clay suspensions and a mathematical model to provide insight on scale-up and design criteria. Rheological-behavior regimes as functions of solids content were identified in yield strength measurements. The single-stage continuous prototype yielded a cake with a solids content of 35 wt.% and a dry-solids production rate of 4.5 kg/h m^2. The mathematical model showed excellent agreement with experimental data collected from the prototype operation. An cost-minimization method was developed using the continuous EKD model to estimate the operation parameters of an industrial-scale process.

The second part of the dissertation is a study of the geometric effect on the electrochemical impedance spectra of interdigitated electrodes. The use of interdigitated microelectrodes is attractive because electrochemical measurements can be obtained with small sample sizes. The impedance response of the interdigitated microelectrodes in

contact with organic and aqueous liquids was simulated via finite-element methods and measured experimentally. The simulations provided explanations for the experimental deviations from ideal impedance responses. For low-conductivity organic liquids, the influence of the substrate on dielectric measurements increased the effective measured capacitance. In dilute electrolytes, the presence of the electrical double layer decreased the solution resistance near the surface of the electrodes. Experimental measurements were performed to extract a cell constant for the interdigitated electrode. The ohmic resistance was not observable in the measurable frequency range for dilute aqueous electrolytes, the cell constant was determined indirectly though application of a model that accounted for other contributions to the real part of the impedance. The cell constant obtained experimentally was in agreement with the cell constant derived from finite-element simulations.

CHAPTER 1
INTRODUCTION

The present work involves the study of two different applications of electrochemical systems. The commonality between the two projects is in the fundamental application of electrochemical engineering. Both projects involve the observation and experimentation of a direct application of electrochemistry and explanations through fundamental mathematical modeling.

The first work involves the mitigation of the environmental impacts resulting from phosphate mining. Phosphate is an essential nutrient used in industrial fertilizers. A dilute clay-water suspension is generated from the beneficiation of the mined ore by froth flotation. The current method of separating the waste slurry by gravity sedimentation of the particles in large settling impoundments called clay settling areas (CSA). In Florida, CSA occupy 150 sq. mi. of land. The objective of the work was the design and modeling an efficient scalable electrokinetic dewatering process to eliminate the need for CSA. Kong[1] developed a fully continuous prototype but lacked scalability due to high capital costs that resulted from low dry-clay production rates. The current work was completed in two stages. The first was to design a prototype and demonstrate that a continuous dewatering process was economical on the prototype scale. The design and experimental operation of the proposed prototypes are in Chapter 4. The second stage of the work was the development of a mathematical model describing continuous dewatering which is in Chapter 5. The model agreed with the experimental data generated from the lab-scale prototype. In Chapter 6, a theoretical scale-up of electrokinetic dewatering of the effluent generated in a typical Florida phosphate mine was performed to examine the economic viability of continuous electrokinetic dewatering.

The second half of the present work focused the study of interdigitated electrodes. These electrodes were designed as electrochemical sensors for bio-impedance applications. A review of electrochemical impedance spectroscopy is in Chapter 8. The objective of

the work was to understand the effect of geometry on electrochemical impedance spectra. An improved understanding of the impedance spectra of interdigitated microelectrodes allowed for a better interpretation of experimental data. In Chapter 9, a mathematical framework was established to simulate the electrochemical impedance response of the interdigitated geometry using COMSOL Mutliphysics®. The simulations were performed assuming the properties of organic liquids, aqueous KCl solutions, and deionized water. In Chapter 10, the simulations presented in Chapter 9 were compared to experimental measurements of the impedance spectra of common organic liquids, aqueous KCl solutions, and deionized water. The analysis has demonstrated the limitations of using interdigitated microelectrodes and proposed a modified electrode for use in solutions with higher conductivities. An example of a application of the proposed use of the interdigitated microelectrodes is presented in the analysis of impedance spectra where 3T3 cells were immobilized on commercially available interdigitated electrodes in Chapter 12. The analysis provides a more comprehensive analysis of using interdigitated microelectrodes in label-less detection of immobilized cells.

CHAPTER 2
PHOSPHATIC CLAY DEWATERING

Phosphorus is an essential nutrient used in fertilizer. The U.S. Geological Survey reports that in 2017 the United States was the third largest producer of phosphate.[2] China and Morocco and Western Sahara were the first and second largest producers, respectively. The current global production of phosphate is shown in Figure 2-1. The U.S. Geological Survey suggests that, given current consumption patterns, the distribution of phosphate mining will shift to locations where phosphate reserves are in abundance.[2] Currently, the top three phosphate producing countries account for 75% of the current production. In contrast, Morocco and Western Sahara hold 75% of the global phosphate reserves; whereas, the U.S. and China account for only 6% of the global reserve. Phosphate mining must move to regions with abundant phosphate reserved like in North Africa due to the increasing global demand which is only expected to increase.[3]
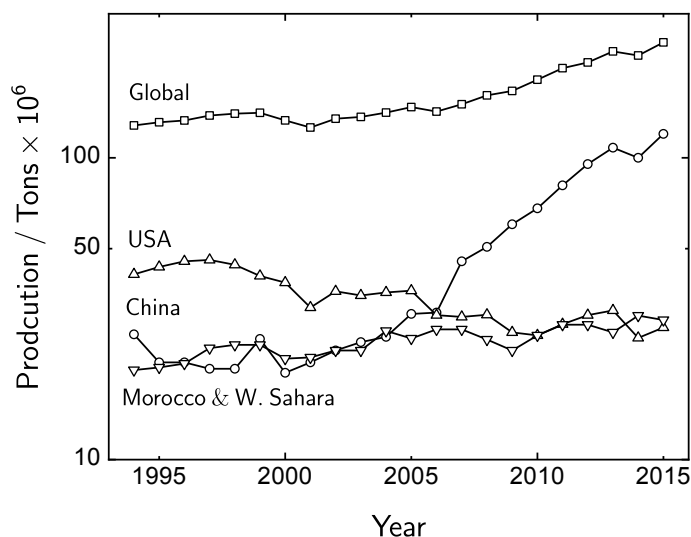
Figure 2-1. The phosphate production in major counties from 1994 to 2016. All data from U.S. Geological Survey, Mineral Commodity Summaries, Phosphate Rock [2, 4–24].

2.1 Phosphate Industry

Phosphate mining has a long history in Florida starting in the late 19th century in the Peace River region near Arcadia, FL. Through industrial development, the capacity

of Florida phosphate mining increased due to the introduction of electric drag-line excavators replacing the initial manual shovel and handpick mining. The increased mining was accompanied with increased generation of waste streams such as phosphatic clay. Phosphate mining occurs in seven locations in Florida, and Florida mines accounted for 65% of domestically-mined phosphate.[25] The accompanying environmental impacts, such as CSAs, demand on local water, and land used for mining, are a concern for the industry.[26] Over 390 km^2 of CSAs are present in Florida. [27]

2.2 Phosphate Mining Process

Phosphate fertilizers are manufactured from phosphoric acid extracted from mining deposits that contain clay minerals and phosphate. [28] Phosphate mining is a strip-mining process in which drag lines expose the 10–20 feet of phosphate-rich matrix which lies below 15–20 feet of overburden.[29] The phosphate-rich matrix consists of phosphate ore, clay, and sand in approximately equal proportions.[30] A flotation process is used to separate the desired phosphate ore from the mined matrix leaving behind the sand and clay as waste streams. The phosphate ore is further processed to phosphoric acid, the sand is reinserted into the open-pit mines, and the phosphatic clay is transferred to the CSAs to begin the long dewatering process by gravity settling.

As a result of industry growth and mining technology development, the area allocated to CSAs increased. The problem of growing CSAs was identified by Tyler and Waggaman who suggested further processing of phosphatic slimes can remove remaining phosphate and decrease the volume of effluent destined for CSAs.[31] Continued concern resulted in the intervention of the Florida government in the Phosphate Land Reclamation Act 28.378(2) that aimed to address the CSAs by mandating the restoration of mined lands and the development of technologies to expedite dewatering.

2.3 Electrokinetic Phenomena

The process of electrokinetic separation of clay and water can be divided into two main categories: electrophoresis and electro-osmosis. Electrophoresis is the movement

of a charged particle in an electrolyte; whereas, electro-osmosis is the movement of an electrolyte in a charged channel. In both systems, the solid is charged, creating an electrical double layer. In the case of phosphatic clays, the negative charge of the particles attract and adsorb anions to the surface and repel cations. Just outside the adsorbed layer, a diffuse region of charge exists where the electrolyte is partly movable. When an electric field is applied, a coulombic force acts on the fluid in the diffuse region and causes movement of the fluid. In dilute clay suspensions, electrophoresis is the mechanism of movement in which the negatively charged particle moves toward the anode. When the clay fabric forms a tortuous porous media, known as a cake, the coulombic forces act on the diffuse region, causing movement of the fluid toward the cathode. In the case of electrokinetic dewatering, electrophoresis is the primary mechanism by which a cake is formed by settling; whereas, electro-osmosis is the mechanism by which additional water in the cake may be removed.

2.3.1 Electrochemistry

The electrochemical reactions involved with EKD are oxygen and hydrogen gas evolution. At the cathode, hydrogen gas is evolved according to the reaction

$$H_2O + e^- \rightarrow \frac{1}{2}H_2 + OH^- \tag{2-1}$$

The anodic reactions reaction are

$$H_2O \rightarrow \frac{1}{2}O_2 + 2H^+ + 2e^- \tag{2-2}$$

and

$$M_a \rightarrow M_a^{n+} + ne^- \tag{2-3}$$

where M represents the metal atom used for the anode and n is the valence of the metal atom. At the cathode, hydrogen gas evolution creates a alkaline environment in the vicinity of the cathode whereas the oxygen evolution at the anode create an acidic environment. A pH gradient is formed in the region between the electrode during the EKD

process. To avoid corrosion of the anode, anodic materials are used that are corrosion resistant.

The interface between the water and the charged clay particle is characterized by an electrical double layer where ionic species in the water are attracted to the particle-water interface. In the diffuse region of charge, ions are attracted to the charged surface but can still be moved under the effect of an tangential electric field.

2.3.2 Fluid Mechanics

The observed electrokinetic phenomena of electrophoresis and electro-osmosis can be quantified using the Navier-Stokes equation

$$\rho_\ell \left(\frac{\partial \mathbf{v}}{\partial t} + \mathbf{v} \cdot \nabla \mathbf{v} \right) = -\nabla p - \nabla \cdot \boldsymbol{\tau} + \mathbf{f} \tag{2-4}$$

where ρ_ℓ is the fluid density, $\mathbf{v}$ is the fluid velocity vector, p is pressure, $\boldsymbol{\tau}$ is the stress tensor, and $\mathbf{f}$ in an external body force acting on the fluid. In the case of electrokinetic phenomena, the body force is

$$\mathbf{f} = \rho_e \mathbf{E} \tag{2-5}$$

where $\mathbf{E}$ is the electric field and ρ_e is charge density.

2.3.3 Soil Mechanics

For saturated soils, Terzaghi's principle [32]

$$\sigma' = \sigma - u \tag{2-6}$$

relates the effective stress σ' to the difference between the total stress σ and the excess pore pressure u. The total stress is the portion of effective stress that acts on the solid phase and can be represented by a solid pressure p_s. The excess pore pressure or pore pressure is the force exerted on the particle soil matrix by the pore fluid. Pore pressure gradients cause redistribution of the pore fluid in a saturated soil. By means of a force balance, the intrinsic phase-averaged pressures, p_c and u, are related to the effective stress
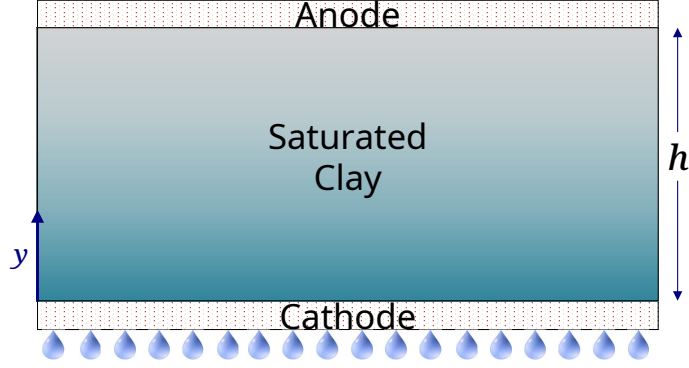
Figure 2-2. A schematic representation of one-dimensional consolidation associated with electrokinetic dewatering.

by

$$\sigma' = (1 - \epsilon)(p_s - u) \tag{2-7}$$

where ϵ is the porosity.[33] A constitutive relationship is assumed to exist between the porosity ϵ and the effective stress σ'.

Esrig extended the principle of effective stress to account for electrokinetic forces.[34] A schematic representation of one-dimensional EKD is illustrated in Figure 2-2, where saturated clay is sandwiched between two electrodes and dewatered in a batch process. The top electrode is the anode, considered to be impenetrable to solids and liquid but allowing transfer of gases produced by the electrochemical reaction. The bottom electrode is the cathode, which was assumed to be open and free to the flow of water. The flow of pore water was assumed to result from the sum of hydraulic forces and electrokinetic forces. The hydraulic velocity v_h is expressed in terms of a pressure-driven fluid velocity,

$$v_h = -\frac{k}{\gamma_w} \nabla u \tag{2-8}$$

where k is the permeability and γ_w is the unit weight of the pore fluid. The electrokinetic velocity v_e was expressed using the Helmholtz-Smoluchowski relation [35], i.e.

$$v_e = -k_e \nabla \Phi \tag{2-9}$$

where Φ is the potential and k_{e} is the electro-osmotic permeability. Under the assumption that the two velocities are additive, the change in pore pressure in one dimension is given by

$$\frac{k}{\gamma_{\mathrm{w}} C_{\mathrm{v}}} \frac{\partial u}{\partial t} = k_{\mathrm{e}} \frac{\partial^2 \Phi}{\partial y^2} + \frac{k}{\gamma_{\mathrm{w}}} \frac{\partial^2 u}{\partial y^2} \tag{2-10}$$

where C_{v} is the coefficient of compressibility.[34]

The boundary conditions were that the fluid velocity is equal to zero at the anode and the pore pressure is equal zero at the cathode. By use of a variable substitution and a separation of variables, Esrig found that

$$u = -\frac{k_{\mathrm{e}} \gamma_{\mathrm{w}}}{k} V(y) + \frac{2 k_{\mathrm{e}} \gamma_{\mathrm{w}} V_{\max}}{k \pi^2} \sum_{n=0}^{\infty} \frac{(-1)^n}{\left(n + \frac{1}{2}\right)^2} \sin \left[\left(n + \frac{1}{2}\right) \frac{\pi y}{h}\right] \exp \left[-\left(n + \frac{1}{2}\right)^2 \pi^2 \tau\right] \tag{2-11}$$

where the dimensionless time τ is defined as

$$\tau = \frac{t}{\tau_{\mathrm{c}}} \tag{2-12}$$

and the batch time constant is defined as

$$\tau_{\mathrm{c}} = \frac{h^2}{C_{\mathrm{v}}} \tag{2-13}$$

Esrig's expression for the time-dependent pore pressure was the basis for the continuous EKD model developed in the present work.[34]

2.4 Dewatering Technologies

The search for improved dewatering methods has led industry and researchers to evaluate an array of methods, including flocculation, which is employed mainly in water clarification applications, and various mechanical dewatering methods, which are used for clay thickening.

2.4.1 Flocculation

Flocculation is a common liquid–solid separation method utilized in water treatment, paper, and mining operations. Sedimentation is achieved by agglomerating the particles

through the addition of flocculating agents. Flocculating agents are often molecules of high molecular weight such as polyethylene oxide and polyacrylamide.[36] The agglomerates called flocs can then be mechanically separated from the dispersing liquid.[37] Recent work on sludge dewatering using ultra-high-molecular-weight flocculants like methyl acrylate-based flocculants shows the continuing interest in the method.[38]

The effect of flocculating agents, specifically Unique Molecular Architecture flocculant, have been observed on phosphatic clay.[39] Currently in the phosphate mining, flocculation is used as the first phase of dewatering phosphatic clay and can produce a 10 wt.% sludge from the initial 2-3 wt.% slurry. Flocculation serves to accelerate the initial sedimentation, but cannot produce cake with high solids content.

2.4.2 Mechanical Dewatering

The most common methods for solid–liquid separation use mechanical energy. Use of mechanical methods is widespread in processing waste water sludge. Mechanical methods primarily remove the water in the free and interstitial layers. A review of these methods on activated sludge was performed by Vaxelaire and Cézac.[40]

Mechanical methods such as filter presses and centrifuges apply mechanical forces to cause dewatering by the removal of free water.[41, 42, 42, 43] The extent of dewatering by mechanical methods is limited because primarily the free water is removed, leaving behind the more closely bound layers of water. Mechanical dewatering is often supplemented with methods that utilize electricity, thermal energy, magnetism, and acoustics. An example is the electrokinetic belt filter that has a conductive filter medium.[44] Thermal drying also has been added to assist in dewatering the discharge sludge from centrifuge processes.[45] Magnetic and acoustic techniques are also under development.[46]

2.4.3 Electrokinetic Separation

The movement of clay particles under the influence of an electric field was reported by Reuss.[47] This observation was explained by the mathematical concept of a double

layer.[48] In 1942, a thorough evaluation of electrokinetic phenomena was performed using kaolin.[49]

Phosphatic clay represents a difficult medium for traditional dewatering methods. Flocculation is only applicable for initial sedimentation up to a solid content of about 10 wt.%. In processing clay for land remediation, the addition of flocculants is not desired. Mechanical methods alone can achieve significant dewatering, but use of mechanical methods to achieve greater than 20 wt.% is cost prohibitive. Electrokinetic dewatering has shown promise in becoming an efficient and economically viable method which has supported our continued work in developing the process.

The use of electrokinetic phenomena in geotechnical applications has been a continuous topic of study in recent decades. For example, heavy-metal contaminants in soils can be leached utilizing electro-osmosis. Electrokinetic remediation of contaminated soil has been employed for removal of zinc, nickel [50], copper, chromium, and arsenic [51, 52]. Electro-osmosis has been used to deposit additives into low-permeability clay contaminated with chlorinated solvents.[53]

Interest in the development of electrokinetics for dewatering is also widespread, as it may be applicable to many types of mine effluent or tailings. In addition to phosphate mining, examples include Canadian oil sands [54, 55], African diamond mines [56], glass-sand plant tailings in Turkey [57], and various metal and petroleum mining operations in South Africa and Western Australia [58, 59]. Clarification using electrophoresis has been studied on effluent from coal washing.[60] The work in coal washing resulted in the creation of a prototype capable of batch or semi-continuous operation as well as the development of a numerical model for electrophoresis. [61]

Shang demonstrated that electrokinetic methods can be used to dewater phosphatic clays to yield a cake suitable for use of a soil cover.[62] She used a bench-top cell to explore the dewatering of Florida phosphatic, Canadian brown, and Canadian grey clays under the influence of an electric field.[63] Geometric configuration, current density, and

electrode materials were found to influence electrokinetic dewatering.[64] The efficiency of electrokinetic dewatering can be optimized with increased understanding relevant factors.

Incremental developments to improve the applicability of electrokinetic phenomena have sustained continued work. Conductive polymers were proposed as electrode materials suitable for electrokinetic dewatering of sewage sludge.[65] Other modifications to existing dewatering technologies include the rotating anode [66], the electrokinetic belt filter press [44, 67, 68], the electrokinetic bag filter [69], and in-situ electrokinetic consolidation [58].

Fourie noted that, while the concept of dewatering soft clays has been used with some success, "difficulties with corrosion of electrodes, loss of contact between soil and electrodes, excessive energy consumption and logistical problems of water collection and management have precluded the widespread use of the technology." [70]

CHAPTER 3
CLAY PROPERTIES

The difficulty of sedimentation and consolidation of phosphatic clay can be attributed to the particle-water interactions and clay particle geometry. The applicability and efficacy of dewatering clay particle requires knowledge of the nature of the solid liquid interaction.

3.1 Phosphatic Clay

The water surrounding particles can be categorized into four layers. The closest layer of water is the water of hydration which is characterized as being chemically bound to the molecules of the clay particle and can only be removed by thermal means. The next layer consists of vicinal water which is loosely bound to the surface of the clay particle. The interstitial water is the next layer that is bound into the agglomerated structures of the particle. This layer of water can be released if the agglomerated structure is destroyed. The last layer is free water which is the bulk water of the suspension that is characterized by free movement and minimal interactions with the particles.[71]

The clay minerals comprising phosphatic clays consist of layers of alumina and silica. Due to lattice defects and ion exchange, the particles develop an overall negative charge which contributes to the strong adherence of hydrating water and the binding of vicinal water. The layered molecular structure results in flat particles that are on average 10 μm in length and less than a 1 μm in thickness with a high surface area of 786 m^2/g.[72] The particle charge and shape create a highly tortuous clay fabric which impedes settling and consolidation as observed in the scanning electron microscopy image of 2-3 wt.% phosphatic clay shown in Figure 3-1.

3.2 Yield Strength of Phosphatic Clay

Using the rheometer developed by Pashias et al.[74], a relationship between the yield strength of the clay as a function of solids content was quantified. The yield strength provides an estimate of the solids content at which the clay-water mixture behaved like a pseudoplastic solid. The method of testing used a PVC pipe with an inside diameter and
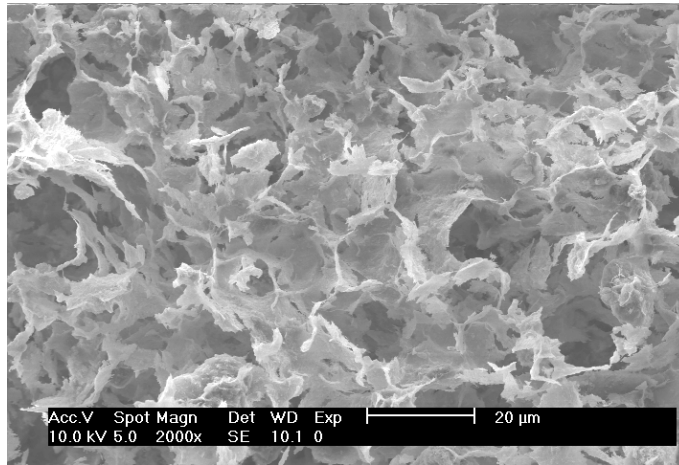
Figure 3-1. Scanning electron microscope image of phosphatic clay suspension before dewatering. Image courtesy of Han Lai.[73]
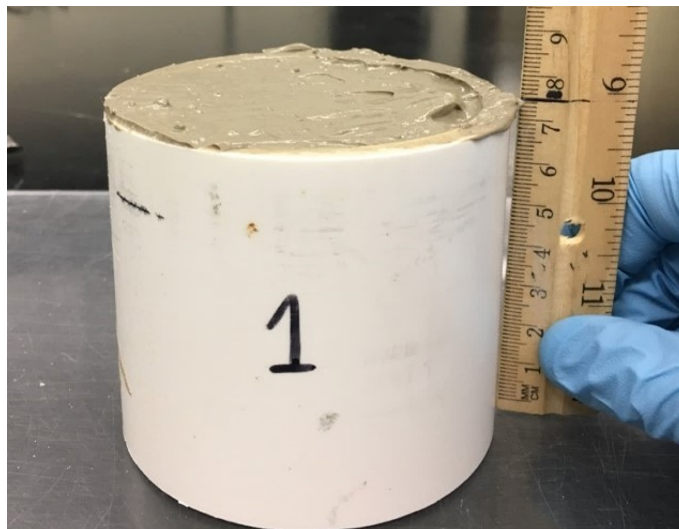
Figure 3-2. Initial state of sample for slump height measurement. Photograph courtesy of Jeremy Kleiman.

height of 3 inches. The cylinder was placed on a flat surface and filled with a clay-water mixture with a known solids content as shown in Figure 3-2. The cylinder was then lifted upwards leaving behind the clay on the flat surface as shown in Figure 3-3. Under self-weight stress, the clay yielded and slumped. The height of the slumped clay was measured as shown in Figure 3-4. The slump height was found to be related to the yield

Figure 3-3. Photograph of the slump test in progress. Photograph courtesy of Jeremy Kleiman.
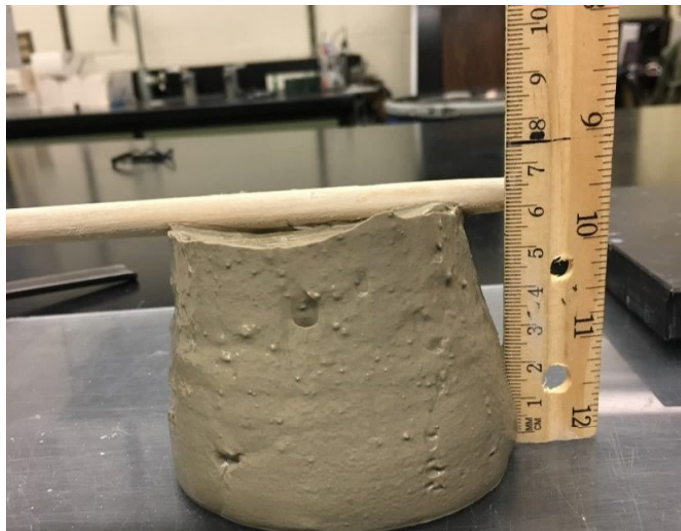
Figure 3-4. Photograph of a yielded clay sample. The slumped height of the clay sample was recorded and related to the yield strength. Photograph courtesy of Jeremy Kleiman.
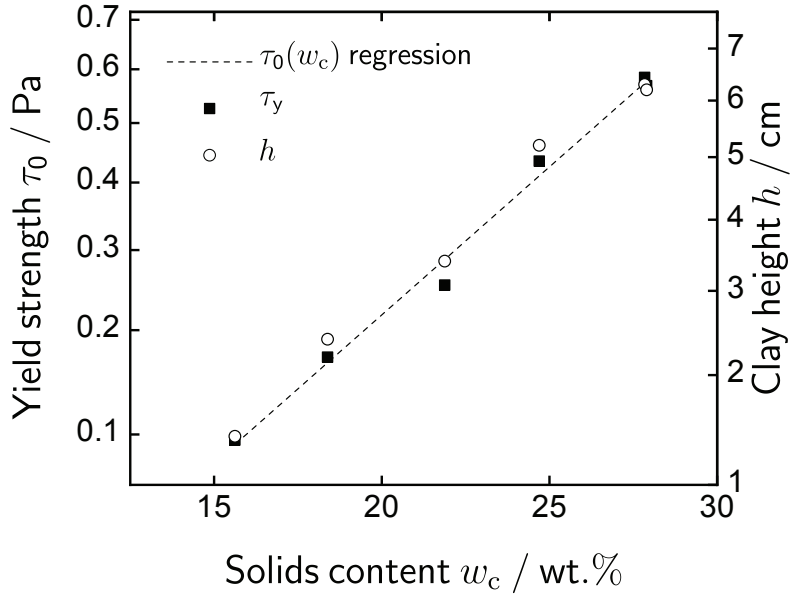
Figure 3-5. Yield strength and slump height as a function of solids content. The dashed line was the result of a linear regression of the square root of yield strength as a function of solids content (see equation (3-1)) with an adjusted R^2 of 0.99. Clay cake with solids content in excess of 29 wt.% did not slump suggesting that the clay cake was behaving like a plastic solid.

strength by

$$\sqrt{\frac{\tau_0}{\rho_s g H_u}} = k_\tau w_c - k_0 \tag{3-1}$$

where g is the acceleration due to gravity, H_u is the unyielded height of the clay sample, k_τ is a constant with units of wt.%$^{-1}$, and k_0 is a dimensionless constant.

Yield strength measurements suggested a minimum solids content where the cake behaved like a plastic solid which was a solids content of 29 wt.%. A simple rheometer developed by Pashias et al.[74] was used to measure the yield strength of a clay sample a function of the slump height. The empirical relationship in equation (3-1) related the yield strength as a function solids content. In Figure 3-5, the yield strength and slump height are shown as a function of solids content where τ_0 is the yield strength and h is the cake slump height. A linear regression between the square root of yield strength and solids content resulted in a fit with an adjusted R^2 of 0.99. The regressed values of k_τ and

k_0 were found to be 1.17 wt.%$^{-1}$ and 8.75, respectively. Clay cake samples with a solids content in excess of 29 wt.% did not have a measurable slump height, suggesting that the onset of plastic behavior had occurred. By extrapolation, a phosphatic clay with a solids content of 7.5 wt.% had a predicted yield strength of zero. The extrapolation suggested that a phosphatic clay with a solids content of 7.5 wt.% can support stress and indicated the onset of viscoelastic-solid behavior.

CHAPTER 4
CONTINUOUS ELECTROKINETIC DEWATERING EXPERIMENTS

Fabrication of continuous electrokinetic dewatering prototypes were developed in two configurations. The first configuration consisted of a two-stage design, a thickening stage and a dewatering stage. The second configuration developed was a single-stage design, where dewatering was carried out in one operation.

4.1   Optimization of Continuous Electrokinetic Dewatering

An optimized process had to produce a pseudoplastic cake at sufficiently high production rate to offset the capital cost required to implement EKD on an industrial scale. The first approach was to separate the EKD process into an electrophoresis stage where the clay was thickened and the electro-osmosis stage where water was driven. Both required the application of an applied electric field.

4.1.1   Thickening-Stage Prototype

The purpose of the first unit was to produce a thickened sludge from the dilute feed. The sludge produced was collected and transferred to the second unit under the constraint that the sludge production rate must be sufficiently high to supply the second unit. A review of common thickener designs led to a system in which a belt system transports clay between two electrodes within a horizontal basin, as shown in Figure 4-1.   The design shown in Figure 4-1 is similar to the horizontal section of the two-zone prototype.[1] The dilute feed clay suspension is fed on the left-hand side of Figure 4-1 and solids-rich sludge is collected on the right-hand side. The belt transports the cake formed on the anode to the sludge collection area. Both electrodes were made of iridium-oxide-coated titanium. The bottom electrode was a solid plate and served as the anode. The top electrode was an expanded-metal mesh and served as the cathode. A standpipe weir collected supernatant water that accumulated at the top of the suspension.

The phosphatic clay had an initial solids content of 4 wt.%, and was left to gravity settle. The supernatant water was decanted, leaving behind 7.5 wt.% clay that was used
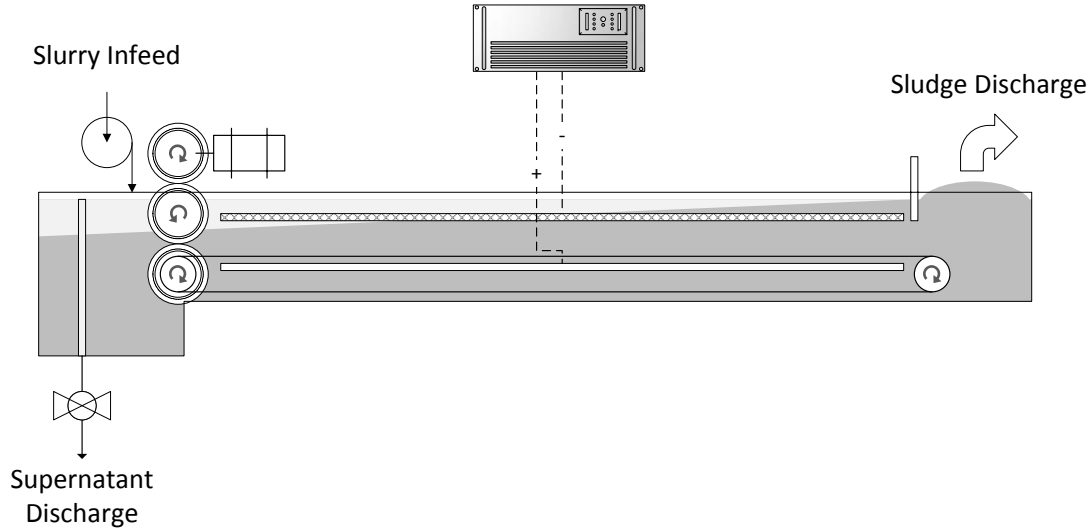
Figure 4-1. A schematic representation of the thickening unit.

as feed for the thickening unit. In a typical experimental run of the thickening unit, the basin was filled with the 7.5 wt.% clay. The electric field was activated and caused clarified water to form at the top of the tank. The DC-power-supply potential ranged from 4.2 to 8.0 V, which, for a measured line resistance of 1.2 Ω, corresponded to a working potential difference of 3.2 V to 5.0 V. The applied potential between the electrodes yielded electric fields between 1.0 and 1.5 V/cm for an electrode separation of 3.4 cm. Prior to activating the belt conveyor, the suspension was allowed to dewater under the applied electric field for 1 hour. After the initial start-up period, the belt motor and feed pumps were activated which caused clarified water to flow towards the feed side of the unit into the standpipe weir. The belt speeds ranged from 0.5 to 1.7 cm/min. The feed volumetric flow rate ranged from 20 to 28 mL/min. A visible one-inch-thick clear-water layer can be seen in the photograph (Figure 4-2) taken after a steady state was reached. The water flowed to the feed side by displacement, due to sludge accumulation at the collection end of the machine as shown in Figure 4-3. While continuous removal of the thickened sludge is envisioned, a batch-wise removal of the thickened sludge was performed. The sludge collection area just after collection is shown in Figure 4-4.
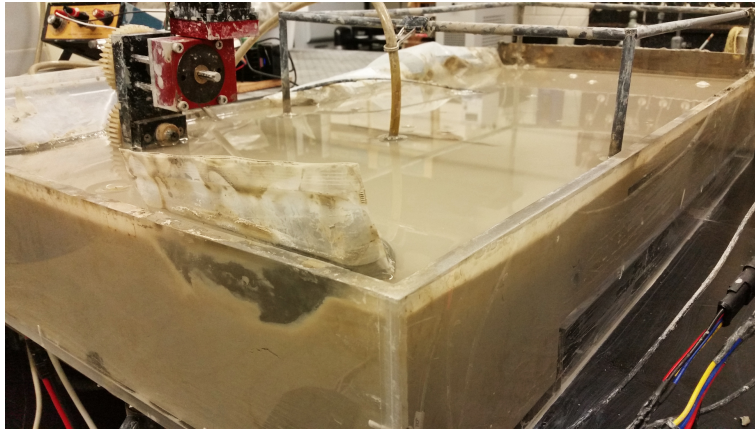
Figure 4-2. The feed side of the thickening unit after the electric field and belts were activated. A clear water layer accumulated on the feed side and was collected using the standpipe weir. The tank was filled and fed a feed with a solids content of 7.5 wt.% and dewatered under a 1.2 V/cm electric field for 1 hour with the conveyor belt off. Image was taken approximately 10 minutes after starting the conveyor belt at 1.3 cm/min. Photograph courtesy of author.
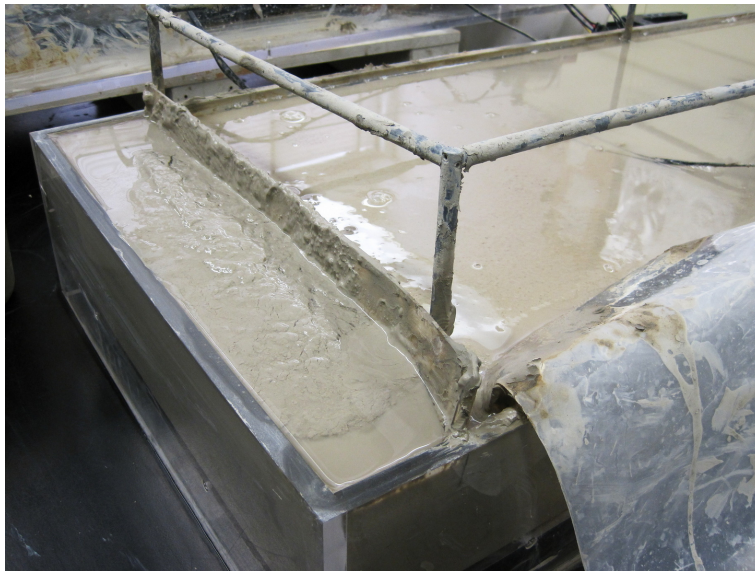
Figure 4-3. Collection area of the clay thickening unit showing an accumulation of thickened sludge produced at an electric field of 1.2 V/cm, a feed rate of 20 mL/min, and a belt speed of 1.3 cm/min. Sludge accumulated for approximately 30 minutes. Photograph courtesy of author.

Figure 4-4. Collection area of the clay thickening unit after batch-wise collection of the thickened sludge. The sludge production continued at the same operating parameters as stated in Figure 4-3 until a sufficient amount accumulated prompting the next collection. Photograph courtesy of author.

Specific changes were made to the thickening unit to improve performance. The dead space in the tank was reduced with water-filled ziplock bags. A standpipe weir was added to collect the top layer of supernatant water. A rigid scrapper made from acrylic was added to the end of the conveyor belt to remove the accumulated sludge from the belt. An acrylic dam added to partition the collection area from the rest of the tank prevented supernatant water from re-suspending the sludge. A two degree tilt in the longitudinal axis of the electrode frame was added to facilitate escape of the bubbles formed at the anode.

The thickening unit was able to produce sludge up to a solids content of 20 wt.%. As shown in Figure 4-5, the solids content obtained for a given applied electric field and retention time was substantially larger than that predicted by the constitutive relations presented by McKinney and Orazem.[75] The residence time τ_r is calculated as

$$\tau_\mathrm{r} = \frac{V}{q_\mathrm{in}} \tag{4-1}$$
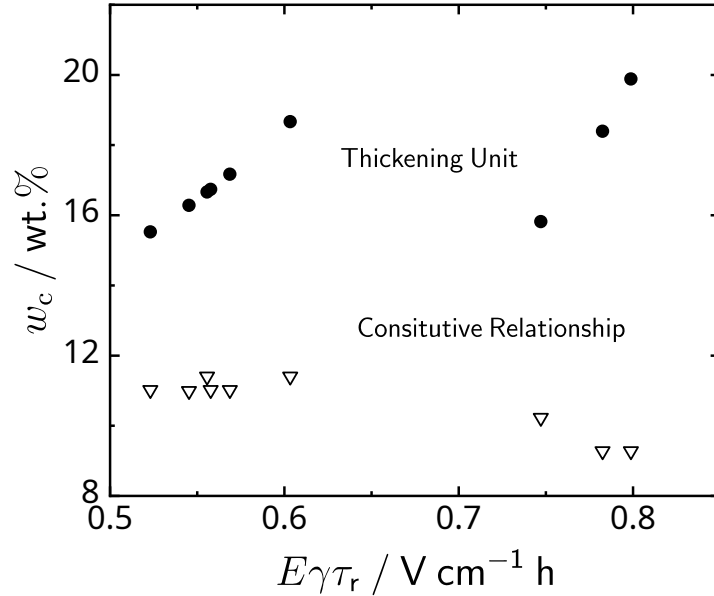
Figure 4-5. Thickening-unit sludge final solids content (circles) and predicted solids content (triangle), calculated using the constitutive relationship [75] as a function of applied electric field and retention time.

where V is the volume between the electrodes and q_{in} is the feed volumetric flow rate. The fraction of active electrode surface area γ, estimated by

$$\gamma = \frac{I}{I_{max}} \tag{4-2}$$

accounted for the electrode surface not blocked by bubbles formed gas evolution. In equation (4-2), I is the steady-state current and I_{max} is the maximum observed current. The electrode area covered by gas bubbles was smaller at lower potentials, due to reduced gas evolution, and was reduced by tilting the electrode assembly, as shown in Figure 4-6. After the electrodes were tilted to facilitate removal of gas bubbles, the average value of γ increased 10% from 0.80 to 0.88. The 10% increase in γ represents a 40% reduction in the area of the electrodes blocked by bubbles.

The supernatant water was collected using an standpipe overflow weir. Turbidity samples were collected after the initiation of the electric field. Within two hours, the turbidity of the water was less than 100 NTU. Mixing associated with gas evolution caused spikes in the turbidity measurements, as shown in Figure 4-7. The samples were
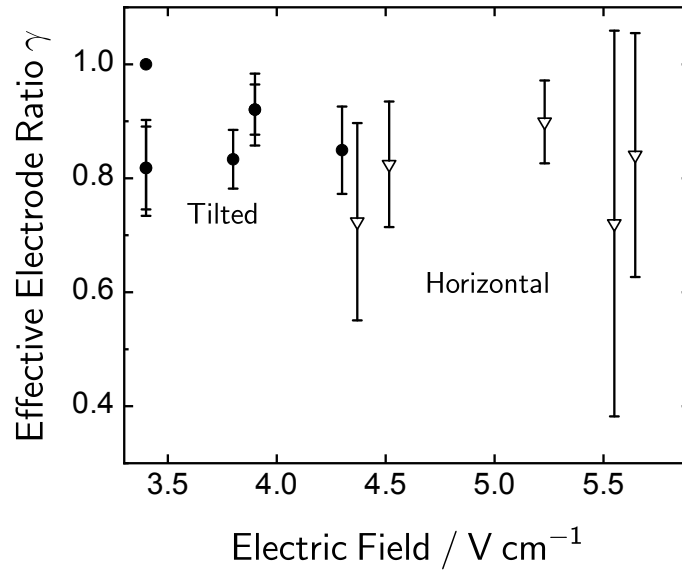
Figure 4-6. Average γ as a function of electric field. When the unit was horizontal, the values of γ (triangle) were higher due to bubble accumulation beneath the belt. By tilting the conveyor frame, the values of γ (circle) were less variable. The reduced variability can also be partially attributed to operating at lower electric fields.
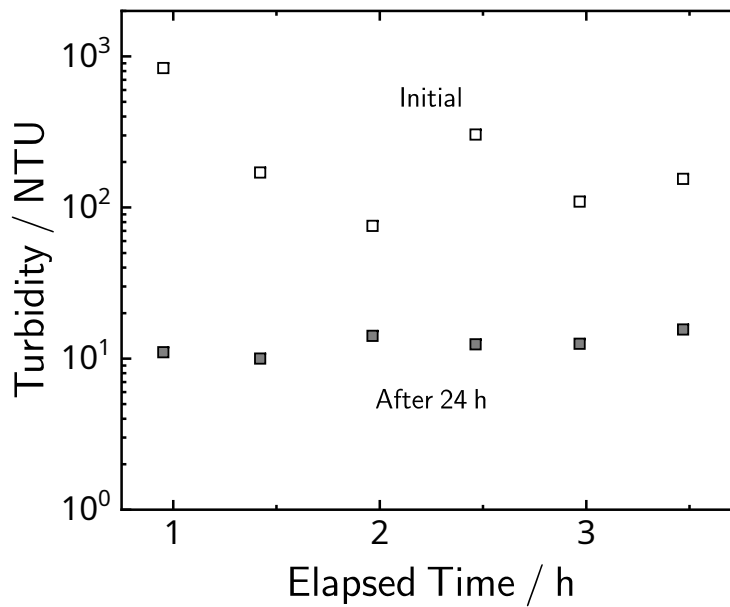
Figure 4-7. Turbidity measurements for supernatant water collected from the thickening unit as a function of elapsed time. The white squares are turbidity measurements taken immediately after sampling and the gray squares are the turbidity measurements 24 hours after sampling.
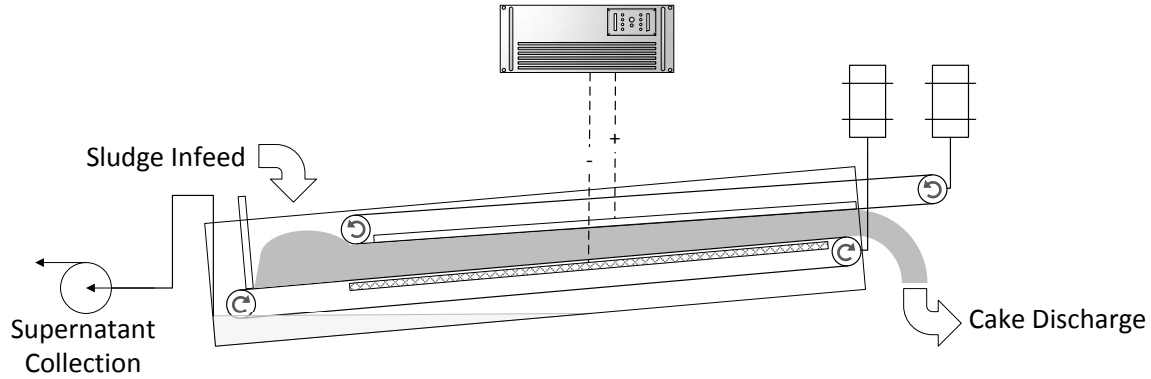
Figure 4-8. A schematic representation of the dewatering unit from the two-stage design.

stored for 24 hours after which the turbidity was remeasured. As observed with previous work, the supernatant water clarified further due to sedimentation.[76].

4.1.2 Dewatering-Stage Prototype

The output of the thickening unit was fed into a dual-belt feed-through continuous machine, shown in Figure 4-8. Two nylon-mesh belts and electrodes sandwiched the clay and allowed for steady movement of the cake. The electrodes were both expanded metal meshes made of iridium-oxide-coated titanium. The gap between the electrodes was tapered, ensuring adequate clay-electrode contact as the clay cake moved through the unit. At the discharge, the electrodes were not fixed in position and were supported by a tensioner that applied a compression force on the clay cake. The polarity of the electrodes was reversed such that the supernatant water moved downward. As the cake moved between the electrodes, the supernatant water flowed through the false-bottom cathode, was collected in the back of the retaining acrylic tank, and removed by use of a peristaltic pump. This approach was found to reduce the rehydration of clay by the supernatant water.

The dewatering unit was typically operated at applied potentials of 15 to 20 V from a DC power supply. When the line resistance of 1.0 Ω was taken into account, the working potential between the electrodes ranged from 10.6 to 14.2 V. The feed-side gap of the electrodes was set at a constant 6.2 cm. Since the electrode gap was tapered, the electric

Figure 4-9. Clay cake with a solids content of 40 wt.% produced in the bench-top cell using a false-bottom cathode as the bottom electrode with constant electric field of 4 V/cm over 5 hours. Photograph courtesy of author.

field increased as the cake progressed down the length of the unit. The feed-side electric field ranged from 1.7 to 2.3 V/cm and was dependent on the working potential. The electrode gap at the discharge ranged from 2.8 to 3.4 cm with an average of 3.4 cm and depended on the working potential, final solids content, and feed rate. The discharge-side electric field ranged from 3.4 to 5.2 V/cm and was a function of the working potential and cake thickness. The belt speed ranged from 0.38 to 0.8 cm/min, and the supernatant water collection rate ranged from 60 to 80 mL/min.

The reversal of the electrode polarities (placing the cathode on the bottom) allowed gravity flow to facilitate the removal of supernatant water. The proof-of-concept for a false-bottom cathode was obtained on the bench-top dewatering cell and resulted in a cake with a solids content of 40 wt.%, as shown in Figure 4-9. The bench-top test was conducted with a batch cell inspired by Shang[77] where expanded-metal meshes were used for the top and bottom electrodes. The bottom electrode was covered with the nylon-fabric mesh to contain the sludge. A potential difference was applied to the

electrodes to maintain a constant electric field of 4 V/cm. As the clay dewatered, water moved through the false-bottom cathode. The anode was then lowered to ensure electrical contact while the applied potential was reduced to maintain a constant electric field. After an elapsed time of 5 hours, a clay cake with a solids content of 40 wt.% was recovered.

The anode configuration was modified to improve dewatering. A tensioner was added to the upper electrode that utilized the belt tension to apply a compression force on the cake. Without adequate compression, approximately the last quarter of the electrode area did not contact the clay. The tensioner improved contact and allowed dewatering along the entire length of the electrodes. Images of the dewatering unit with the anode and top belt removed are shown in Figures 4-10 and 4-11, showing the progression of the sludge to dewatered cake as the clay traveled the length of the machine.

The final modified dewatering unit was able to produce a dewatered cake with a solids content up to 36 wt.%. A maximum wet-cake production of 6.5 kg/hr was observed. The turbidity of the supernatant at steady-state was measured at 39 NTU. After 24 hours of settling, the turbidity measurement was reduced to less than 1 NTU. An image of the dewatered cake collected is shown in Figure 4-12.

4.1.3 Single-Stage Prototype

Experiments were performed to determine if the dewatering unit of the two-stage design was capable of operating with an unthickened feed. The dewatering unit was fed using a peristaltic pump. The primary concern of the operational mode was leakage of the unthickened clay through the open area of false-bottom mesh belt. In the design for the dewatering unit of the two-stage unit, the frame for the electrodes and belt, and the acrylic tank were inclined 2° in the lateral axis to facilitate the flow of supernatant water to the collection area of the acrylic tank. In utilizing only the dewatering unit as shown in Figure 4-13, the frame for the belt and electrodes was inclined -2° in the lateral axis to improve the contact between the fluid clay and anode while the 2° incline of the acrylic

Figure 4-10. Dewatering unit from the feed side without the top frame. The feed-side electric field was 2.1 V/cm and the belt speed was 0.38 cm/min. The unit was fed sludge with a solids content of 13 wt.%. This image was taken from an experiment used to troubleshoot the prototype and was not used in the economic analysis. Photograph courtesy of author.
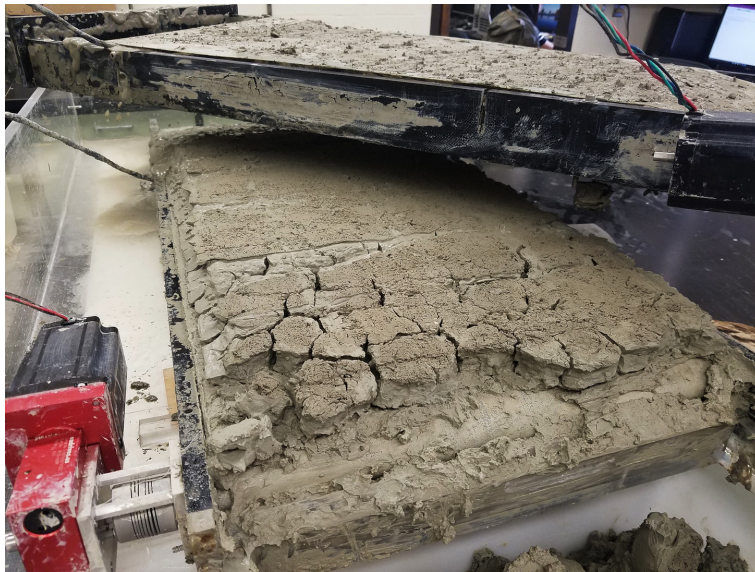
Figure 4-11. Dewatering unit from the collection side. The discharge-side electric field was 4.8 V/cm and the belt speed was 0.38 cm/min. The unit produced cake with a solids content of 36 wt.%. This image was taken from an experiment used to troubleshoot the prototype and was not used in the economic analysis. Photograph courtesy of author.

Figure 4-12. Collected clay cake collected at the discharge of the dewatering unit in the two-stage design. The photograph was taken on the same experimental run as the images shown in Figures 4-10 and 4-11. The unit produced cake with a solids content of 36 wt.% at 3.2 kg/hr which corresponds to a dry-clay production rate of 1.2 kg/hr. This image was taken from an experiment used to troubleshoot the prototype and was not used in the economic analysis. Photograph courtesy of author.
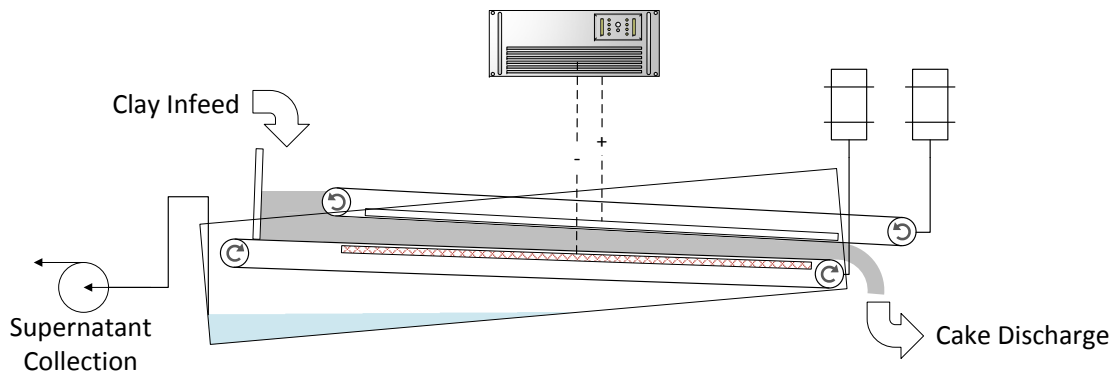
Figure 4-13. A schematic representation of the dewatering unit operation with unthickened feed clay.
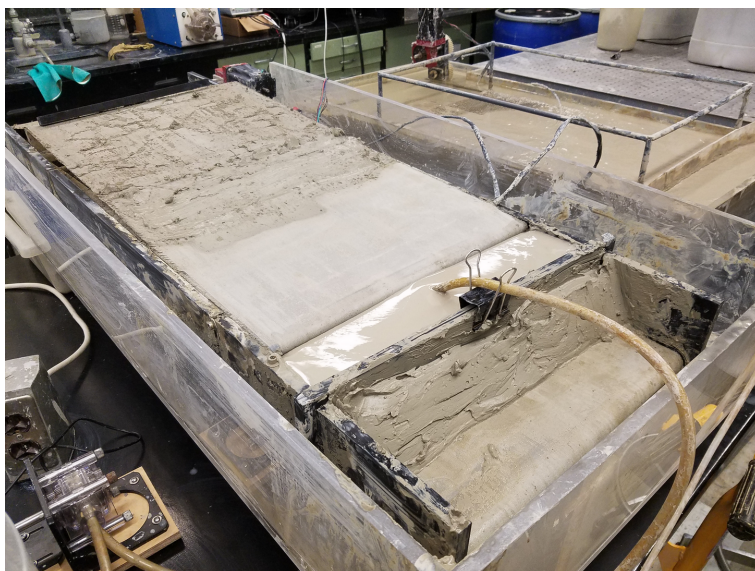
Figure 4-14. The dewatering unit was fed unthickened clay. Dewatered cake was used to make a retaining dam to prevent the dilute feed from leaking. The unit was operated under an effective potential of 15.4 V, a belt speed of 0.56 cm/min, and a volumetric feed rate of 130 mL/min. Photograph courtesy of author.

tank was maintained. The feed section of the dewatering zone was sealed with dewatered clay to prevent leakage of the unthickened clay as shown in Figure 4-14.

A typical operation in the single-stage dewatering unit with unthickened feed produced cake with a final solids content that ranged from 31 to 38 wt.% as pictured in Figure 4-15. The maximum observed wet-clay production rate was 3.6 kg/hr. The applied potentials were increased, in comparison to the two-stage operation, to maintain effective dewatering and ranged from 17.5 to 22.5 V. The effective potential ranged from 12.6 to 16.5 V when the 1 Ω line resistance was taken into account. The feed-side gap was maintained at 6.23 cm, which resulted in a feed-side electric field from 2.0 to 2.7 V/cm. Due to the lower solids-content of the feed, the average cake thickness was decreased to 2 cm resulting in a discharge-side electric field that ranged from 5.2 to 8.3 V/cm. The turbidity of the supernatant fluid increased in comparison to the two-stage configuration. The supernatant turbidity was measured at 1400 NTU. The larger turbidity was attributed to leakage of feed suspension into the stream of clarified water. As with previous supernatant samples, the suspended clay in the supernatant settled within 24
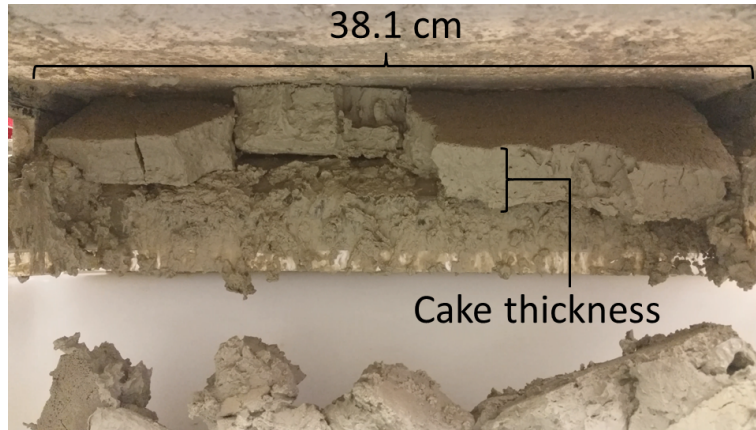
Figure 4-15. The cake produced from a typical experimental run taken at the discharge of the dewatering unit. The dewatered clay cake thickness was a function of the feed solids content, belt speed, and electric field. At the discharge, the two-stage design produced clay at an average thickness of 3.4 cm and the single-stage design produced cake at an average thickness of 2 cm. The image was taken from the experiment labeled as "s" in Table 4-1. Photograph courtesy of author.

hours, resulting in a measured turbidity of 1 NTU. The conversion of the suspension from a 10 wt.% feed to a solid cake can be seen in Figure 4-16, showing the clay after the upper anode frame was removed. The fingers of low solids-content cake at the discharge can be attributed to the clay sticking to the anode when the upper frame was removed. The progressive dewatering as the clay traveled down the unit is evident.

4.2 Dewatering Efficacy of a Carbon-Steel Cathode

Experiments with carbon steel serving as the cathode were completed for the purpose of cost reduction in electrode materials. All previous prototypes utilized dimensionally stable anodes (DSA) made of titanium coated with iridium oxide for both the cathode and anode. Bench-top EKD tests were performed utilizing a 1008 carbon-steel expanded-metal cathode on the cell developed by McKinney.[78] The tests showed comparable currents resulted between the DSA and the carbon-steel cathodes at elapsed times greater than 1 hour, shown in Figure 4-17, where the cell current is presented as a function of elapsed operation time. A constant electric field of 4 V/cm was maintained in the bench-top test. The low current observed for the carbon-steel electrode during the first hour of operation

49

Figure 4-16. The dewatering unit was operated under the same conditions as in Figure 4-14. The fingers of low solids-content cake at the discharge was due to the clay sticking to the anode when the upper frame was removed. The progressive dewatering as the clay travels down the unit is observed. Photograph courtesy of author.
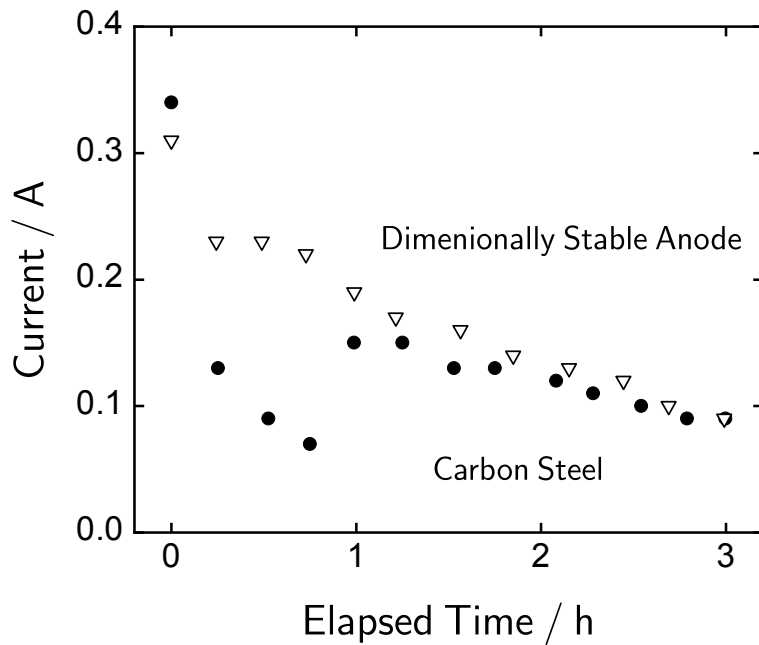
Figure 4-17. Measured current as a function of elapsed time using the bench-top cell operating at a constant electric field of 4 V/cm where the false-bottom cathode was DSA (triangle) and carbon steel (circles).

can be attributed to the removal of the metal-oxide film on the cathode surface. After the film was removed in the first hour of operation, the operating current increased and was similar to the operating current of the DSA cathode. The resulting solids content for the carbon-steel cathode was 2 wt. % lower than obtained using the DSA cathode. The reduction in final solids content was attributed to the initial low current during the removal of the metal-oxide film. These experiments indicate that use of a carbon-steel cathode did not reduce EKD efficacy.

4.3   Economic Analysis of Prototypes

The estimated total energy of the two-stage and single-stage designs were comparable to the energy used in the two-zone design. The applied energy on a dry-clay basis E_{req} is calculated as

$$E_{\text{req}} = \frac{100 I V_{\text{eff}}}{w_c m} \tag{4-3}$$

where the average steady-state current is I, the working potential is V_{eff}, and mass production rate of wet-cake is m. The final solids content for the two-zone, two-stage, single-stage is presented in Figure 4-18 as a function of energy required on a dry solids basis. The data reported and used for the economic analysis of the two-stage and single-stage designs is from experiments where the process was fully optimized which amounted to 9 experimental runs of the total 18 experimental operations.

The dry-clay production rate of the two-zone, two-stage, and single-stage designs are compared in Figure 4-19.   A linear decrease in final solids content was observed as the dry-clay production rate increased for all three designs. The two-stage design showed that dry-clay production rate increased while maintaining high final solids content. At a solids content of 35 wt.%, the production rate increased approximately 5 fold when compared to the two-zone design. The single-stage design had an approximate 8 fold increase in the production rate of cake with a solids content of 35 wt.% when compared to the two-zone design.
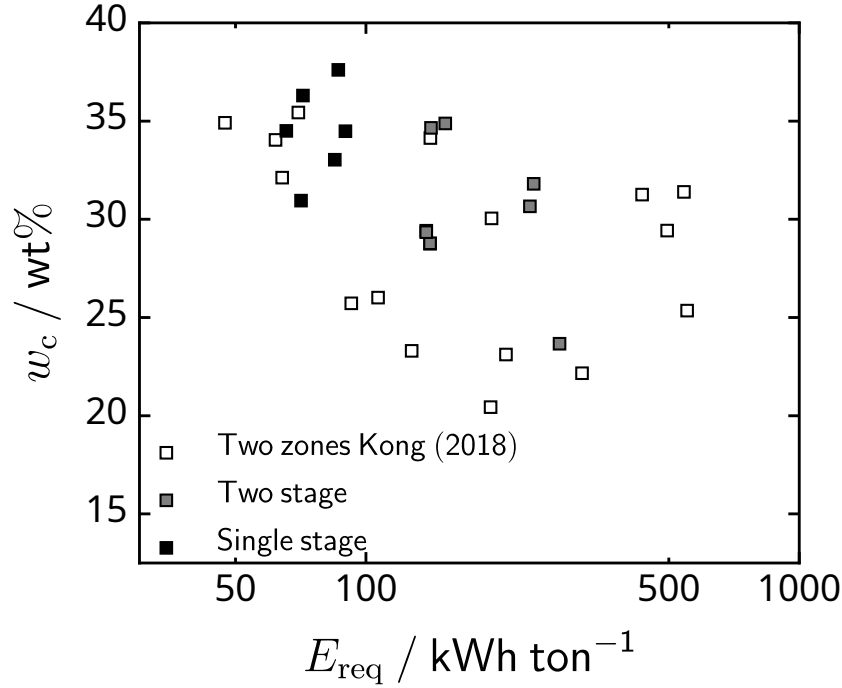
Figure 4-18. Final solids content as a function of the energy required on a dry-clay basis produced in the two-zone Kong (2018) (white), two-stage design (gray), and single-stage (black).

A reduction of the capital costs of industrial EKD can be achieved by increasing the throughput. The capital cost to produce a ton of dry clay in $/tons dry solids, represented by C_{cap}, is calculated by

$$C_{\text{cap}} = \frac{100 C_{\text{annual}}}{w_{\text{c}} m} \tag{4-4}$$

where the annualized capital cost C_{annual} is

$$C_{\text{annual}} = C_0 \frac{i \left(1 + i\right)^n}{\left(1 + i\right)^n - 1} \tag{4-5}$$

The capital cost was calculated assuming a 10% interest rate, represented by i, and a term of 20 years which is represented by n. The present value of the capital investment at installation is C_0 in units of $/m². The decrease of capital cost with increasing the process throughput is shown in Figure 4-20.[80]

The experiments with the carbon-steel cathode showed comparable performance when compared to the DSA. The cost of DSAs used in the bench-top experiments is on the
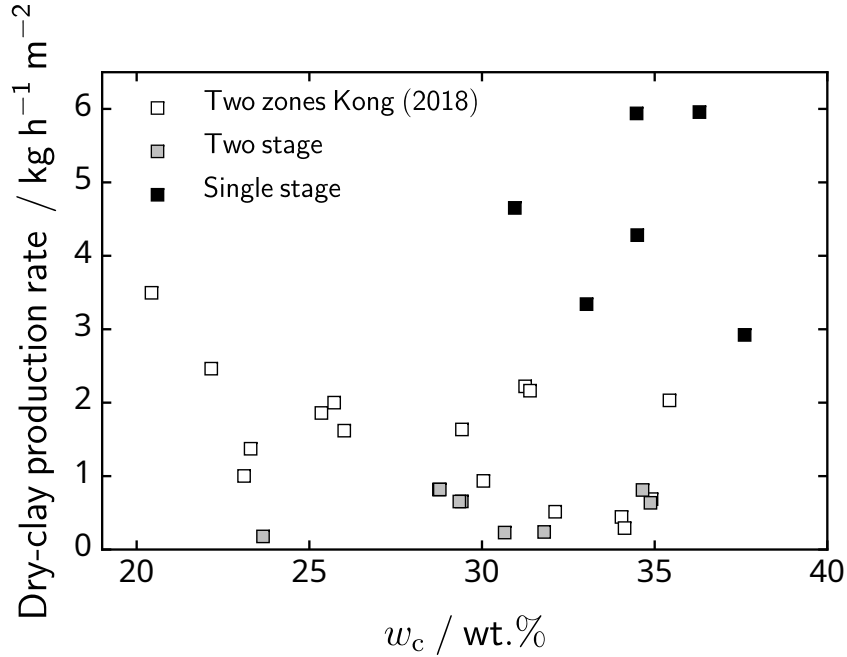
Figure 4-19. Dry-clay production rate per unit area of electrode as a function of the final solids content produced in the Kong two-zone design[79] (white), two-stage (gray) design, and single-stage design (black). Each data point is labeled with the feed solids content.

order of 4,000 USD/m²; whereas, the cost of expanded-mesh carbon-steel electrodes is on the order of 4 USD/m². The use of carbon-steel cathodes will reduce the capital cost of the dewatering unit.

The installation cost per unit area was estimated at \$2000/m². The cost of electricity was estimated at \$0.062/kWh. The estimated electrical cost C_{op} required to process one metric ton of dry clay can therefore be calculated as

$$C_{\mathrm{op}} = C_{\mathrm{elec}} E_{\mathrm{req}} \tag{4-6}$$

The primary cost of operation was assumed to be due to cost of electricity. The cost of electricity, represented by C_{elec}, was assumed to be \$0.062/kWh. As shown in Figure 4-21, a low electrical operational cost was maintained at the highest production rates in the latest design.
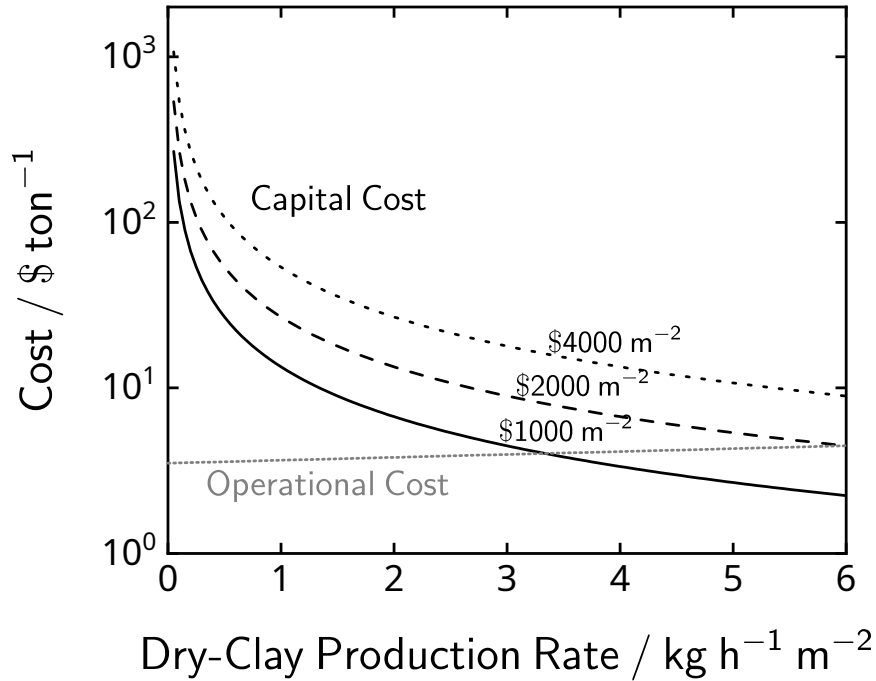
Figure 4-20. Capital cost per ton of dry-clay as a function of dry-clay production rate per unit area with the present-value of the capital investment C_0 as parameter. The gray line is the estimated electrical cost per ton of dry solids as a function of the dry-clay production rate and was fit using the 2nd unit power consumption data.

The total cost per ton of dry clay C_{total} was estimated by

$$C_{\text{total}} = C_{\text{cap}} + C_{\text{op}} \qquad (4\text{-}7)$$

The total cost per ton of dry-clay is represented as function of dry-clay production rate per unit area of electrode in Figure 4-22. A substantial reduction in the total cost is projected with the single-stage design, which is a result of increased throughput at high solids content, cheaper carbon-steel cathodes, and lower power consumption due to reduced electrode area. Under the assumed capital cost, the cost per metric ton of dry clay is projected to be on the order of $11-12/metric ton of dry-clay, with a solids content of 38 wt.%.
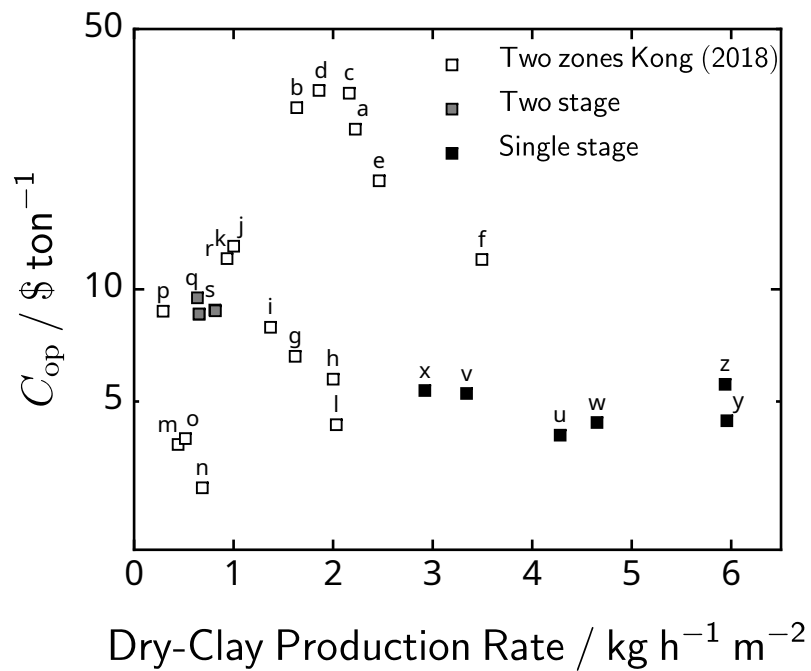
Figure 4-21. Operational cost as a function of dry-clay production rate per unit area of electrode of the Kong two-zone design[79] (white), two-stage (gray) design, and single-stage design (black) assuming an electrical cost of $0.062/kWh. Each data point is labeled with an letter index which refers to the operating conditions listed in Table 4-1.

Table 4-1. The operating conditions, feed solids content, final solids content, and electric field, for each of experimental runs presented in Figures 4-21 and 4-22. The columns on the left are operational data from the previous two-zone design.[1] The columns on the right represent data from the current work with the two-stage and single-stage designs. The electric field $E_{\min}$ presented is the electric field calculated from the effective potential and the feed-side electrode gap.

Two Zone[1]				Two Stage			
Index	w_{in} wt.%	w_{out} wt.%	$E_{\min}$ V/cm	Index	w_{in} wt.%	w_{out} wt.%	$E_{\min}$ V/cm
a	10	31	4.0	q	19	34	2.0
b	10	29	4.0	r	18	35	2.0
c	10	31	4.0	s	19	29	1.7
d	10	25	4.0	t	16	29	1.9
e	10	22	4.0				
f	10	20	4.0				
g	10	26	2.0		Single Stage		
h	10	26	2.0	Index	w_{in} wt.%	w_{out} wt.%	$E_{\min}$ V/cm
i	10	23	2.0				
j	10	23	2.0	u	10	35	2.0
k	10	30	2.0	v	10	33	2.5
l	10	35	2.0	w	10	31	2.4
m	10	34	1.0	x	12	38	2.6
n	10	35	1.0	y	16	36	2.7
o	10	32	1.0				
p	10	34	1.0				

Figure 4-22. Total cost as a function of dry-clay production rate per unit area of electrode of the two-zone design (white), two-stage design (gray), and single-stage design (black). The initial cost was estimated at \$2000/m^2. The capital cost calculation assumed 10% interest over 20 years and an electrical cost of \$0.062/kWh. Each data point is labeled with an letter index which refers to the operating conditions listed in Table 4-1.

CHAPTER 5
MATHEMATICAL MODEL OF CONTINUOUS ELECTROKINETIC DEWATERING

Estimation of full industrial-scale continuous EKD required the development of a mathematical model. The model incorporated knowledge of soil mechanics, transport, and electrochemistry to quantify the forces acting on the fluid. The solids content distribution between the electrodes was achieved by first calculating the excess pore pressure distribution of the fluid. The pore pressure distribution was utilized to calculate the average change in porosity due to the redistribution and removal of the pore fluid. A constitutive relationship that related the effective stress to the porosity was defined, allowing calculation of the solids content distribution.

5.1 Previous Work

The electrokinetic velocity of a fluid is proportional to the applied electric field, as shown by the Smoluchowski-Helmholtz relation.[35, 81] The electric field interacts with the fluid in the electrical double layer, resulting from the inherent charge of the suspended particle, in the form of a body force that generates movement of the fluid with respect to the particle.[82]

The application of EKD in soils has been in consolidation and stabilization via a batch in-situ EKD process. The efficacy of electro-osmosis as an enhanced consolidation method was assessed by the evaluation of the ratio of k_e and k, which are respectively the electro-osmotic permeability and permeability of the soil.[83] A mathematical treatment of electrokinetic forcing on the excess pore pressure of a saturated soil produced an analytical solution to time-dependent consolidation via EKD.[34] Shang[84] developed a model for batch consolidation of saturated clay using a surcharge load and electro-osmotic flow where vertical electrodes inserted into clay impoundment act as drains. Hu et al.[85] accounted for anisotropic permeability in the electrokinetic consolidation of clay. Yuan et al.[86] developed a model of batch 1-D electrokinetic consolidation that accounted for clay consolidation where large deformations occurred. The efficiency of the vertical electrode

configuration in electrokinetic consolidation was modeled where various patterns of vertical drain cathodes and anodes were assessed.[87]

Analytical expressions of the electrokinetic permeability were developed to quantify the fluid velocity resulting from an applied electric field.[35] Shang [88] proposed an empirical linear relationship between the electro-osmotic permeability of the clay fabric and zeta potential of the particle in modeling electrokinetic flow in clay media. Electro-osmotic permeability was observed to be a function of the pore fluid salinity in the work of Mohamedelhassan and Shang[89] which was then used to estimate the power consumption of EKD.

Applications of electrokinetic sedimentation to seal leaks in walls of impoundments was modeled using Stoke's Law and electrokinetic forces.[90] McKinney and Orazem[91] developed a constitutive relationship between solids content, applied electric field, and residence time which was used in the performing an economic assessment of industrial EKD which determined that the large energy requirement caused batch EKD to be uneconomical.[92]

5.2   2-D Model of Excess Pore Pressure

The schematic representation of the continuous EKD process, presented in Figure 5-1, consisted of two planar mesh electrodes that sandwiched the saturated clay. A belt system transported the clay between the electrodes. The feed-side gap d_1 (left) was larger than the collection-side gap d_2 (right). The top electrode served as the anode, and the bottom electrode of length L served as the cathode. Under an applied potential, the water was discharged through the cathode. The assembly was tilted to prevent loss of the feed clay suspension. The roller at the collection side of the top belt was not fixed in place, allowing the anode to pivot, rest on the moving clay, and maintain electrical contact.
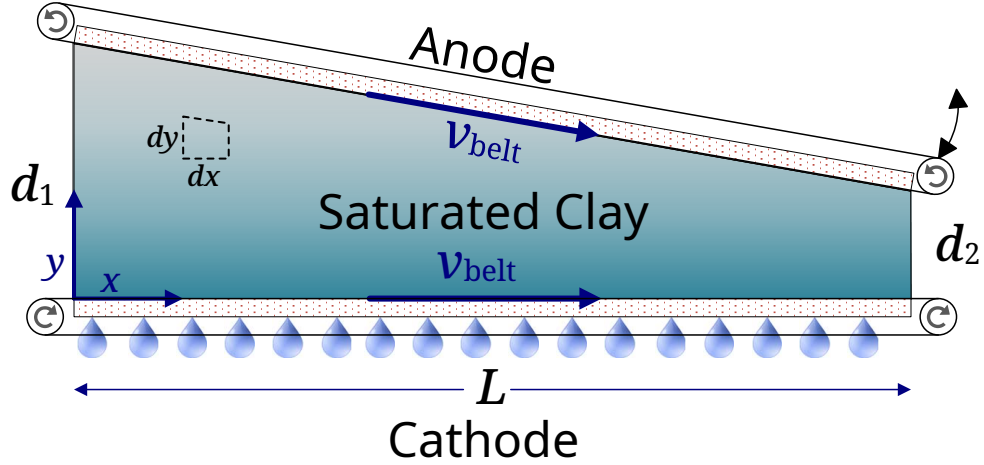
Figure 5-1. A schematic representation of a two-dimensional continuous EKD process. A belt system transports the clay between the electrodes of length L at a constant speed v_{belt}. The feed side gap d_1 (left) was larger than the collection-side gap d_2 (right). The roller at the collection side of the top belt was not fixed in place, allowing the anode to pivot as indicated by the curved double arrow. The material volume element is indicated by the dotted trapezoid.

For the steady-state operation, equation (2-10) can be applied to a material volume that moves with the belt. Thus,

$$\frac{k}{\gamma_{\text{w}} C_{\text{v}}} \frac{\mathrm{D}u}{\mathrm{D}t} = k_{\text{e}} \frac{\partial^2 \Phi}{\partial y^2} + \frac{k}{\gamma_{\text{w}}} \frac{\partial^2 u}{\partial y^2} \tag{5-1}$$

where

$$\frac{\mathrm{D}u}{\mathrm{D}t} = \frac{\partial u}{\partial t} + v_{\text{belt}} \frac{\partial u}{\partial x} \tag{5-2}$$

Under assumption of a steady state,

$$\frac{\mathrm{D}u}{\mathrm{D}t} = v_{\text{belt}} \frac{\partial u}{\partial x} \tag{5-3}$$

The horizontal position was scaled by the cathode length L as

$$\eta = \frac{x}{L} \tag{5-4}$$

60

The gap between electrodes was a function of horizontal position; i.e.

$$h = d_1 \left[1 - \left(1 - \frac{d_2}{d_1} \right) \eta \right] \tag{5-5}$$

and the dimensionless normal position was given by

$$\zeta = \frac{y}{h} \tag{5-6}$$

Under assumption of a linear potential distribution,

$$\Phi = V_{\max} \zeta \tag{5-7}$$

where $V_{\max}$ is the applied potential difference.

Equations (5-1)–(5-7) were used to create a 2-D analog of the time-dependent electrokinetic consolidation presented by Esrig[34] in equation (2-10). The equation governing steady-state operation of the system shown in Figure 5-1 can be expressed with a dummy variable ξ as

$$\frac{\partial^2 \xi}{\partial \zeta^2} = \frac{h^2 v_{\text{belt}}}{L C_{\text{v}}} \frac{\partial \xi}{\partial \eta} \tag{5-8}$$

where

$$\xi = \frac{\gamma_{\text{w}} k_{\text{e}}}{k} \Phi + u \tag{5-9}$$

The boundary conditions were that $\xi = 0$ at $\zeta = 0$ for all η, $\partial \xi / \partial \zeta = 0$ at $\zeta = 1$ for all η, and $\xi = 0$ at $\eta = 0$ for all ζ. The problem is similar to that solved by Esrig[34] with the exception that h is a function of position η. The solution to the dummy variable ξ was obtained by separation of variables. By elimination of ξ with equation (5-9), an expression for dimensionless pore pressure ψ was found to be

$$\psi = -\zeta + \frac{2}{\pi^2} \sum_{n=0}^{\infty} \frac{(-1)^n}{(n+\frac{1}{2})^2} \sin \left[\left(n + \frac{1}{2} \right) \pi \zeta \right] \exp \left\{ -\frac{\left(n + \frac{1}{2} \right)^2 \pi^2 \tau_{\text{r}} \eta}{\tau_{\text{c}} \left[1 - (1 - d_{\text{r}}) \eta \right]} \right\} \tag{5-10}$$

where the dimensionless pore pressure is defined as

$$\psi = \frac{k}{k_{\text{e}} \gamma_{\text{w}} V_{\max}} u \tag{5-11}$$

61

the characteristic time constant τ_c for the continuous process, similarly to the batch process, is defined as

$$\tau_c = \frac{d_1^2}{C_v} \tag{5-12}$$

and the residence time τ_r is defined as

$$\tau_r = \frac{L}{v_{\text{belt}}} \tag{5-13}$$

The gap ratio d_r is defined by

$$d_r = \frac{d_2}{d_1} \tag{5-14}$$

and was calculated from the physical dimensions of the system. A mass balance was used to express d_r as a function of solids content, i.e.

$$d_r = \frac{\langle w_{\text{in}} \rangle \left[\langle w_{\text{in}} \rangle \rho_s + (100 - \langle w_{\text{in}} \rangle) \rho_w \right]}{\langle w_{\text{out}} \rangle \left[\langle w_{\text{out}} \rangle \rho_s + (100 - \langle w_{\text{out}} \rangle) \rho_w \right]} \tag{5-15}$$

where the densities of the pore water and dry clay are represented by ρ_w and ρ_s, respectively. The normally averaged solids content of the feed clay-water suspension and product clay cake are represented by $\langle w_{\text{in}} \rangle$ and $\langle w_{\text{out}} \rangle$ respectively in units of wt.%.

The temporal evolution of pore pressure in the 1-D batch system is presented in dimensionless form in Figure 5-2A, and the spatial evolution of the pore pressure in the 2-D continuous system is shown in Figure 5-2B. Comparison of Figures 5-2A and 5-2B shows a similar functionality, indicating that the time dependence of the 1-D batch process has been successfully transformed into a 2-D continuous process.

5.3   Average Porosity

A relationship between pore pressure and the porosity for a material volume was obtained from a volume-averaged equation of continuity under the assumption that the liquid was incompressible, i.e.

$$\frac{\mathrm{D}\epsilon}{\mathrm{D}t} = -\nabla \cdot \langle v_\ell \rangle \tag{5-16}$$
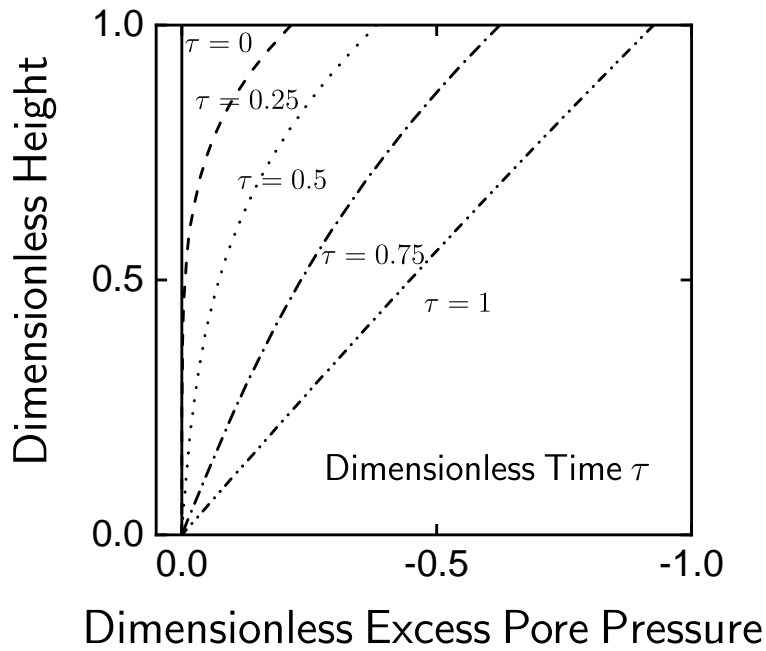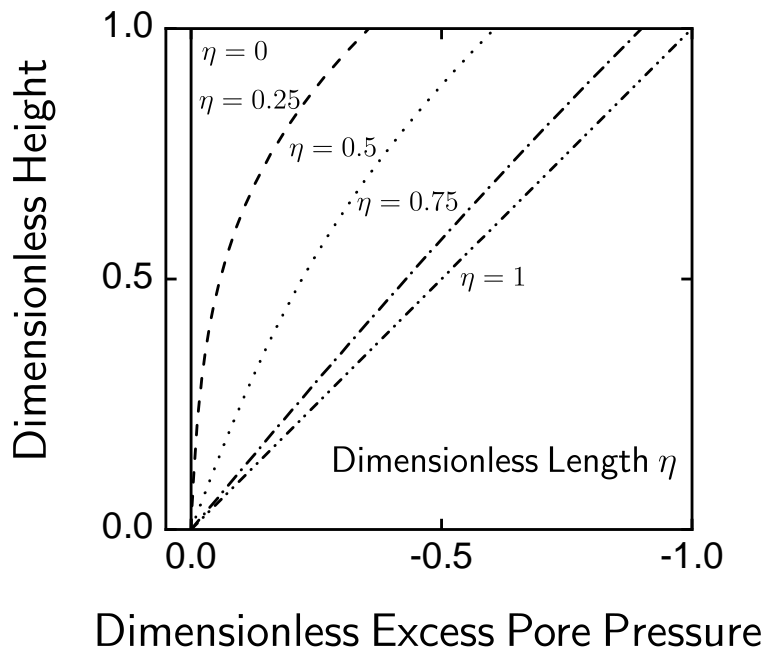
Figure 5-2. Dimensionless excess pore pressure as a function of dimensionless time and position: (a) calculated from equation (2-11) for a batch 1-D EKD process with dimensionless time as a parameter and (b) calculated from equation (5-10) for a continuous EKD process with dimensionless horizontal position as a parameter.

The electro-osmotic velocity and the hydraulic velocity were assumed to be additive and were substituted into equation (5-16), resulting in

$$\frac{D\epsilon}{Dt} = \frac{2k_e V_{\max}}{\pi^2 h^2} \frac{\partial^2}{\partial \zeta^2} \sum_{n=0}^{\infty} \frac{(-1)^n}{\left(\frac{n+1}{2}\right)^2} \sin\left[\left(\frac{n+1}{2}\right)\pi\zeta\right] \exp\left\{-\frac{\left(\frac{n+1}{2}\right)^2 \pi^2 \tau_r \eta}{\tau_c \left[1 - (1 - d_r)\eta\right]}\right\} \qquad (5\text{-}17)$$

Equation (5-17) relates the change of porosity to the second derivative of the pore pressure, given as equation (5-10). Under assumption of a steady state, equation (5-17) may be written as

$$\frac{d\epsilon}{d\eta} = -\frac{2k_e V_{\max}\tau_r}{C_v \tau_c \left[1 - (1 - d_r)\eta\right]^2} \sum_{n=0}^{\infty} (-1)^n \sin\left[\left(\frac{n+1}{2}\right)\pi\zeta\right] \exp\left\{-\frac{\left(\frac{n+1}{2}\right)^2 \pi^2 \tau_r \eta}{\tau_c \left[1 - (1 - d_r)\eta\right]}\right\}$$
$$(5\text{-}18)$$

Equation (5-18) provides the rate of change of porosity in the continuous single-stage EKD process. The normally averaged porosity was obtained by integration of equation (5-18) over the interval from $\zeta=0$ to 1 followed by numerical integration from 0 to η. Thus, the normally averaged porosity $\langle\epsilon\rangle$ was defined to be

$$\langle\epsilon\rangle = \langle\epsilon_{in}\rangle - \frac{2k_e V_{\max}\tau_r}{\pi C_v \tau_c} \int_0^{\eta} \frac{1}{\left[1 - (1 - d_r)\eta\right]^2} \sum_{n=0}^{\infty} \frac{(-1)^n}{\left(\frac{n+1}{2}\right)} \exp\left\{-\frac{\left(\frac{n+1}{2}\right)^2 \pi^2 \tau_r \eta}{\tau_c \left[1 - (1 - d_r)\eta\right]}\right\} d\eta \quad (5\text{-}19)$$

where $\langle\epsilon_{in}\rangle$ is the normally averaged porosity of the feed at η equal to zero. The normally averaged porosity was found to be a function of dimensionless length and was related to solids content in wt.% according to

$$w_c = \frac{100}{\left[\frac{\rho_w}{\rho_s}\left(\frac{\epsilon}{1-\epsilon}\right) + 1\right]} \qquad (5\text{-}20)$$

The solids content is presented in the present work in terms of wt.% because this unit is more common industrially and may be easily obtained by experiment.

5.4   Comparison of Model to Experimental Results

The constants k_e and C_v were obtained by a generalized reduced gradient algorithm in minimizing the sum of square errors of simulation data calculated by equations (5-19) and (5-20) with experimental data. The values of k_e and C_v were found to be
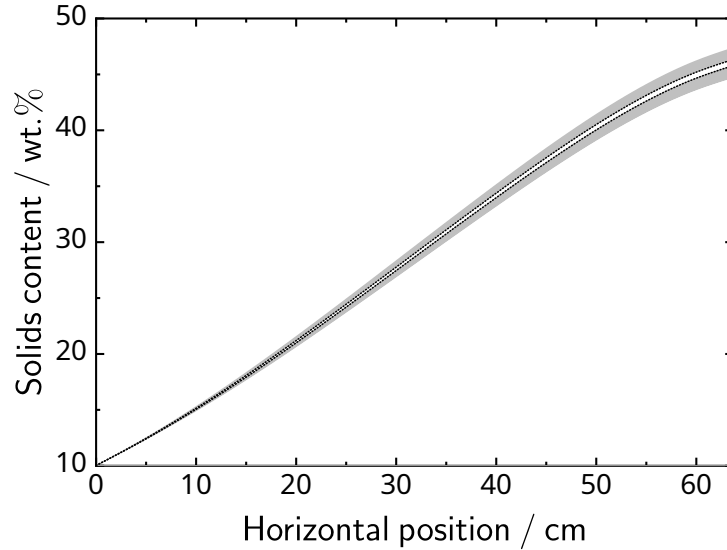
Figure 5-3. Solids content as a function of horizontal position with k_e as a parameter. The white region enclosed by the dotted line was calculated by varying k_e by 1%. The gray region was calculated by varying k_e by 5%.

3.84×10^{-5} cm^2/V s and 1.14×10^{-3} cm^2/s, respectively. These and other assumed parameter values are presented in Table 5-1. The regressed values for k_e and C_v are in good agreement with values from literature which are on the order of 2×10^{-5} cm^2/ V s and 1×10^{-3} cm^2/s, respectively.[84, 85] The sensitivity of the simulation output on the extracted constants k_e and C_v were evaluated by varying the regressed value by 1% and 5%, shown in Figures 5-3 and 5-4 respectively. Figures 5-3 and 5-4 suggest that the rate of dewatering is dominated by the value of k_e and the extent of dewatering is a function of both k_e and C_v. The experimental solids content of samples taken from the feed side, conveyor belt, and collection side at various operating applied potentials and belt speeds are presented in Figure 5-5 as functions of calculated solids contents using equations (5-19) and (5-20). A linear fit of actual solids content to calculated solids content resulted in a slope of 1.0 with an adjusted R^2 value of 0.99.

The experimental data reported by Dizon and Orazem [93] from operation of the continuous prototype were divided into two categories: manually fed and pump fed. In preliminary experiments, the single-stage unit was fed manually providing an intermittent
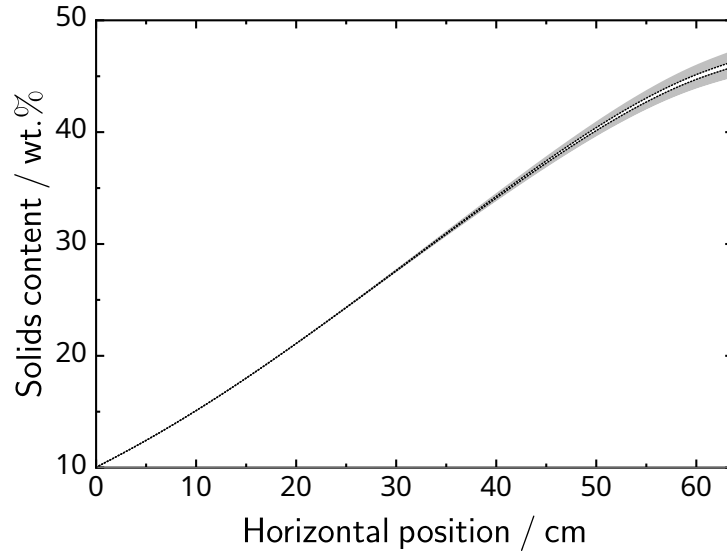
Figure 5-4. Solids content as a function of horizontal position with C_v as a parameter. The white region enclosed by the dotted line was calculated by varying C_v by 1%. The gray region was calculated by varying C_v by 5%. The effect of varying C_v is primarily observed in the final solids content.

Table 5-1. Constants for EKD simulation

Constant	Value
unit weight of pore fluid γ_ℓ	980 g/s^{2}cm^2
density of water ρ_ℓ	1 g/cm^3
density of clay ρ_s	2.65 g/cm^3 [a]
permeability k	8×10^{-4} cm/s [b]
electro-osmotic permeability k_e	3.84×10^{-5} cm^2/V s [c]
compressibility C_v	1.14×10^{-3} cm^2/s [c]
constitutive relation characteristic pressure p_e	20 kPa [c]
solid-pressure constant a	0.023 [c]
yield strength slope k_τ	1.17 wt.%$^{-1}$ [c]
yield strength y-intercept k_0	8.75 [c]

[a] Typical value for clay materials. [72]

[b] Typical value for clay materials. Calculated at $\epsilon =0.80$.[85]

[c] Value obtained by regression to experimental data.
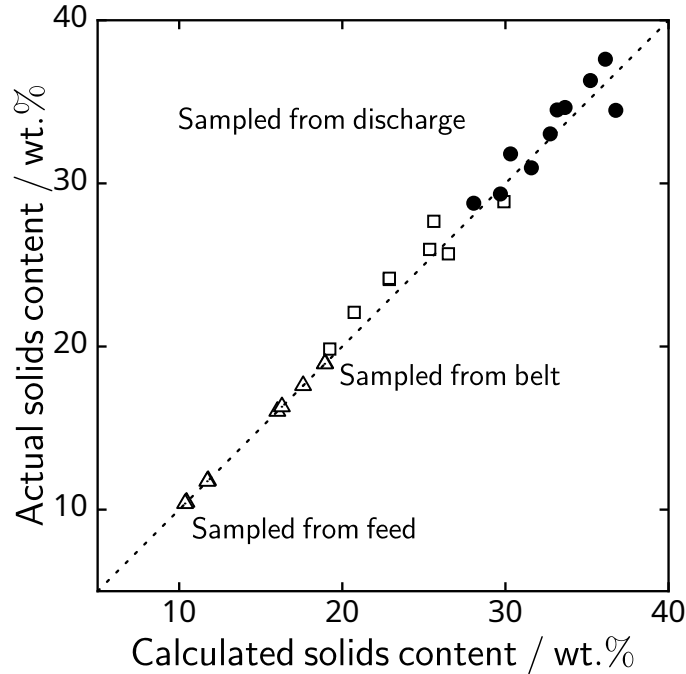
Figure 5-5. Experimental solids content of samples taken from the feed-side, conveyor belt, and collection bin at various operating applied potentials and belt speeds as a function of values calculated from equations (5-19) and (5-20). A linear fit of actual solids content to calculated solids content resulted in a slope of 1.0 with an adjusted R^2 value of 0.99. The approximately linear relationship suggests that the model adequately describes the lab-scale continuous EKD process. Regressed values are shown in Table 5-1.

pseudo-steady-state operation. After the addition of a peristaltic feed pump, the unit became fully continuous and was capable of operating at a steady state. Data collected from the manually fed system was categorized as manually fed. For the manually fed data, the observed and calculated values for dry-clay production rates and energy requirements were in poor agreement. Analysis of the fully continuous data showed excellent agreement between the observed and calculated values. The observed and calculated dry-clay production rates per area electrode were linearly fit with an adjusted R^2 of 0.99 as shown in Figure 5-6. The observed and calculated energy required per mass of dry clay are presented in Figure 5-7, and linear regression yielded an adjusted R^2 of 0.96. Figures 5-5, 5-6, and 5-7 suggest that the developed model adequately describes the operational modes of the single-stage unit.
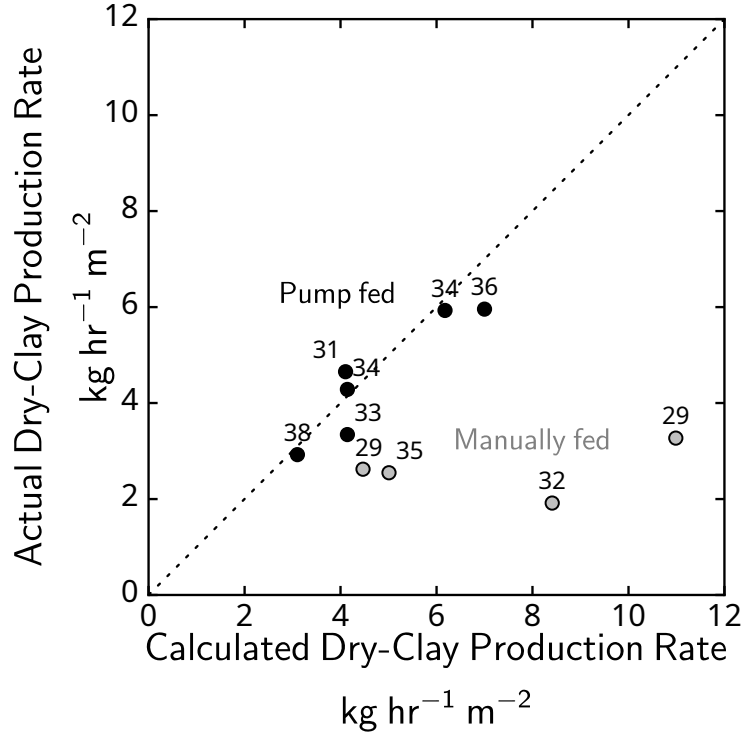
Figure 5-6. Experimental dry-clay production rate per area of electrode as a function of the values calculated from equations (5-19) and (5-20). A linear fit of actual production rates to calculated production rates resulted with an adjusted R^2 value of 0.99 with the exclusion of gray data points labeled "Not Continuous". The black data points collected during fully continuous operation are labeled "Fully Continuous". All points are labeled with the final solids content of the clay in units of wt.%.

5.5 Solids Content Distribution

As shown in equation (2-7), the effective stress on the clay-water mixture is related to the solid-liquid pressure difference or effective stress. Previous work in consolidation examined the effect of effective stress on clay materials.[94] A constitutive relationship between porosity and the effective stress was proposed to be of the form

$$\epsilon = \epsilon_\infty + \frac{\epsilon_{\text{in}} - \epsilon_\infty}{1 + \dfrac{(p_{\text{s}} - u)}{p_{\text{c}}}} \tag{5-21}$$

where p_{c} is a characteristic consolidation pressure and ϵ_∞ is the limiting porosity for the specific clay material.[33] The constitutive relation given as equation (5-21) was fit to
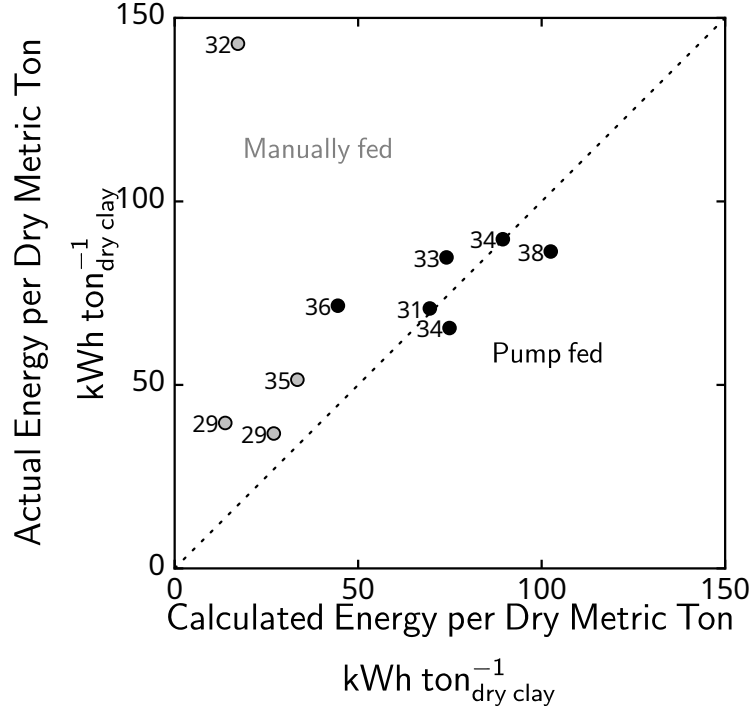
Figure 5-7. Experimental energy demand per mass of dry clay as a function of the values calculated from equations (5-19) and (5-20). A linear fit of actual energy consumption to calculated energy consumption resulted with an adjusted R^2 value of 0.96 with the exclusion of gray data points labeled "Not Continuous". The black data points collected during fully continuous operation are labeled "Fully Continuous". All points are labeled with the final solids content of the clay in units of wt.%.

experimental saturated-clay consolidation data reported by Craig [94]. The resulting fit, shown in Figure 5-8, indicates that equation (5-21) provides a good account for the influence of the solid-liquid pressure difference on porosity under consolidation, and the characteristic consolidation pressure p_c was found to have a value of 3.53 MPa^{-1}.[33] The pressure differences for the present work are much smaller, and, to allow equation (5-21) to satisfy the input conditions under which the solid matrix does not bear a load, equation (5-21) was modified to be a linear relationship

$$\epsilon = \epsilon_{in} - \frac{(p_s - u)}{p_e} \tag{5-22}$$

69
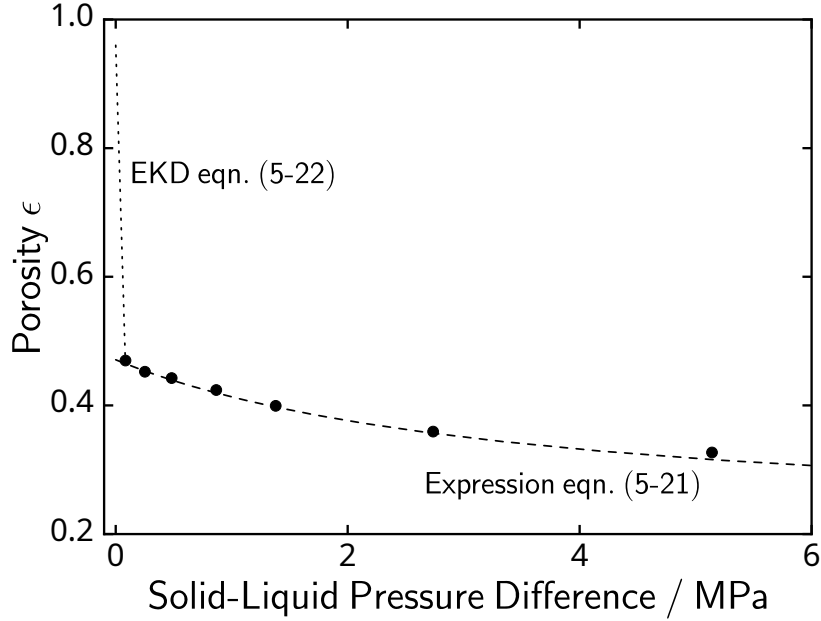
Figure 5-8. Porosity as a function of the solids-liquid pressure difference. The dotted line given by equation (5-22) and is the proposed linear relationship between the porosity and solid-liquid pressure difference during EKD. The data represents experimental data reported by Craig [94], and the dashed line is the fit of equation (5-21) to the data.

where ϵ_{in} is the initial porosity and p_{e} is the characteristic pressure for electro-osmotic dewatering. The pore pressure u was defined by equations (5-10)–(5-15). Under consolidation conditions where the porosity is below 0.8, the constitutive relation, shown as equation (5-21), is applicable. In EKD, the operative porosity range is greater than 0.8 and the pressures are significant smaller. In porosity range between 0.96 to 0.8, the solid pressure p_{s} was assumed to be of the form

$$p_{\text{s}} = a\eta(1 - \zeta)\tau_0 \tag{5-23}$$

where a is a constant of the continuous EKD process and τ_0 is the yield strength. The yield strength as function of solids content was determined by the measurements using a simple rheometer as described by Pashias et al.[74]. Quantification of the yield stress allowed for calculation of the upper limit of solid pressure using equation (2-7). Values of
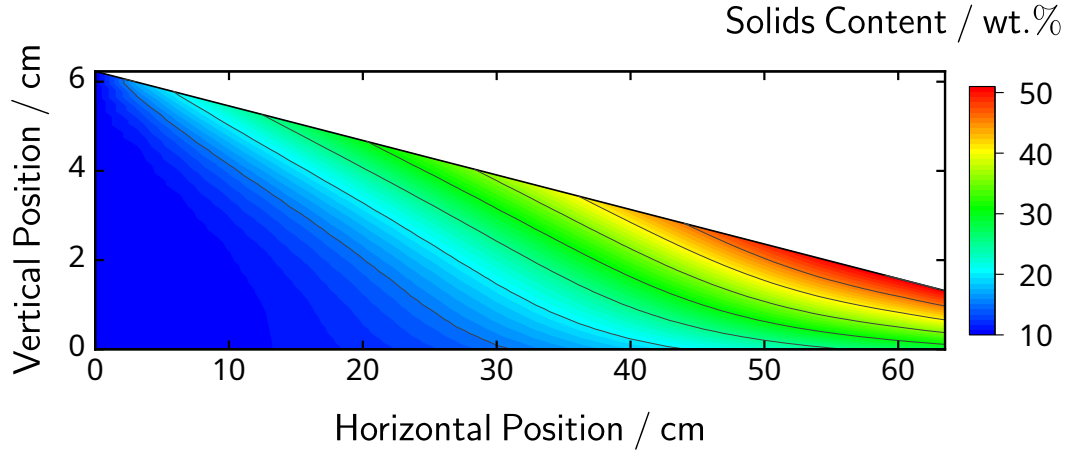
Figure 5-9. Calculated solids content distribution of the continuous single-stage EKD unit using equations (5-19), (5-20), and (5-21) with an applied potential of 20 V, feed clay with a solids content of 10 wt.%, and a belt speed of 0.8 cm/min. The system dimensions and operating conditions were consistent with prototype measurements. Simulations were performed using parameters shown in Table 5-1.

the parameters p_e in equation (5-22) and a in equation (5-23) were obtained by nonlinear regression to experimental data reported by Dizon and Orazem [93]. The solids content distribution was calculated using equations (5-10), (5-22), and (5-23).

The yield strength as a function of solids content adhered to an empirical relationship given as equation (3-1) The values are presented in Table 5-1. The normal distribution was then calculated using the parameters which is shown in Figure 5-9. The vertical solids content distribution was verified by comparing the normally averaged solids content calculated by the constitutive relationship in equation (5-21) and by the model result given as equation 5-19. Both were in agreement and suggests that the constitutive relationship was an acceptable model for estimating the vertical solids content distribution as shown in Figure 5-10. The sensitivity of constant a in equation (5-22) on the simulation output was observed by performing the simulation while varying a by 1% and 5%, shown in Figure 5-11. The deviation from an ideal linear correlation between the solids content of the model and the solids content of the constitutive relation was due to
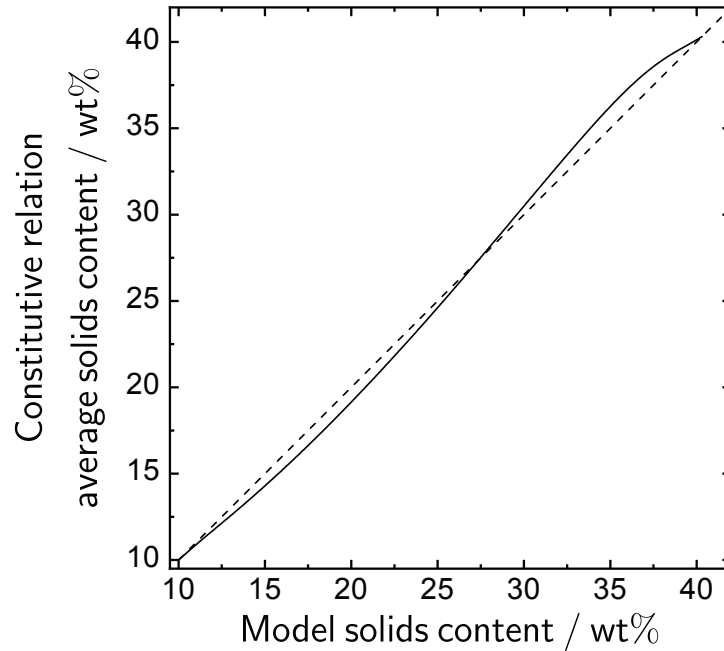
Figure 5-10. Normally averaged solids content calculated by the constitutive relationship in equation (5-21) as a function of the normally averaged solids content calculated by equation (5-19). The dashed line represents the linear approximation given in equation (5-22) and the solid line represents the normally averaged solids content from Figure 5-9. The difference between the two line is the error due to the linear assumption.

the assumptions of porosity given in (5-22) and the assumption of a solid-phase pressure distribution given as equation (5-23).
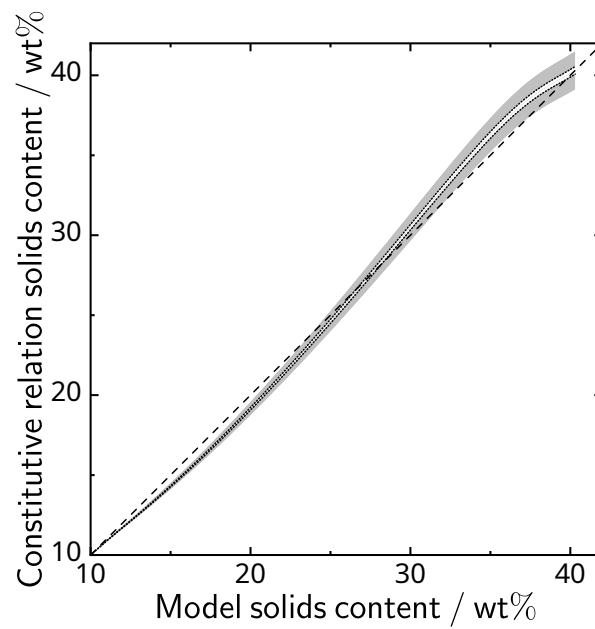
Figure 5-11. Solids content as a function of horizontal position with a as a parameter. The white region enclosed by the dotted line was calculated by varying a by 1%. The gray region was calculated by varying a by 5%.

CHAPTER 6
OPTIMIZATION AND SCALE UP OF CONTINUOUS ELECTROKINETIC DEWATERING

The model described in the present work was used to estimate the electrode area and energy required for a scaled-up continuous EKD operation. The clay resistivity ρ was estimated from experimental potential and current data from the continuous single-stage prototype and had an average value of 20.5 Ω m. The energy required per mass of dry clay E_{req} was calculated by

$$E_{\text{req}} = \frac{200 V_{\text{max}}^2 LW}{\rho_{\text{m}} w_{\text{c}} m \left(d_1 + d_2\right)} \tag{6-1}$$

where W is the electrode width and m is the mass production rate for wet-clay. An assumed electrical cost of 0.062 \$/kWh was used for the calculation of the operating cost using Equation (4-6) The capital cost C_{cap} has units of US dollars per mass of dry clay. The capital cost was calculated using Equations (4-4) and (4-5). Capital cost calculations assumed to have a term of 20 years ($k = 20$), an interest rate of 10% ($i = 0.1$), and an estimated cost C_0 of \$2000/m^2 of electrode. The total cost is the sum of the operating and capital costs as shown in Equation (4-7).

6.1 Scale-Up of Unconstrained Operation

Simulations of a pilot-scale continuous single-stage EKD process were performed using the present model. The pilot-scale operation assumed a continuous single-stage EKD unit that was 10-fold larger in all dimensions as summarized in Table 6-1. The present model was used to estimate the belt speed, applied potentials, and electrode gaps required to generate a dewatered clay cake with a solids content of 35 wt.% from a dilute clay suspension with a solids content of 10 wt.% from a pilot-scale process. The

Table 6-1. Dimensions of the lab-scale prototype and the simulated pilot-scale continuous EKD process

	lab-scale (m)	pilot-scale (m)
L	0.635	6.35
W	0.381	3.81
d_1	0.0623	0.623
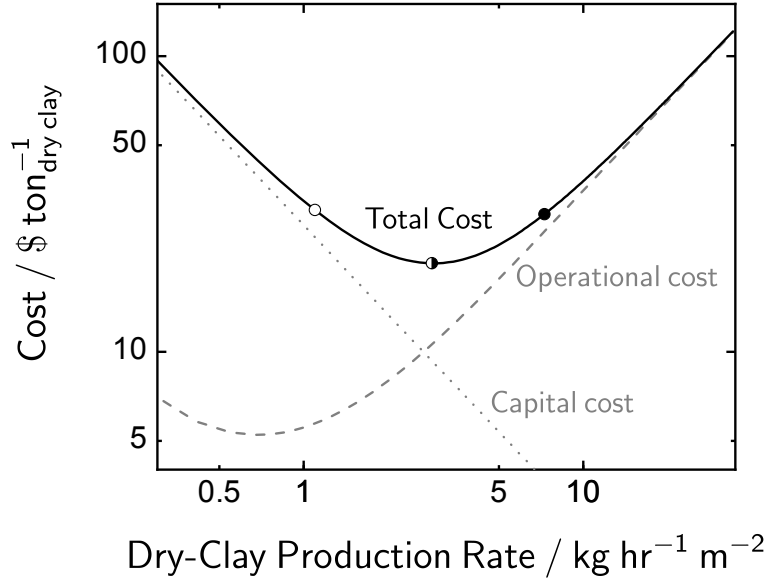
Figure 6-1. Cost for a pilot-scale continuous EKD process producing cake with a solids content of 35 wt.% as a function of dry-clay production rate per electrode area. The gray lines are the operational and capital costs associated with the production of cake with a solids content of 35 wt.%. The estimated operating data for the minimum and the reference points are presented in Table 6-2. Reference points are marked with ○ and ●. The minimum is marked with ◐.

Table 6-2. Operation parameters for reference points and the minimum from Figure 6-1 for the pilot-scale single-stage EKD process producing a cake with a solids content of 35 wt.% from a feed clay with a solids content of 10 wt.%. The maximum electric field $E_{\max}$ is the electric field at the collection end of the machine. The symbols match markers used in Figure 6-1, and the minimum cost is marked by the symbol ◐.

Conditions	$V_{\max}$	$E_{\max}$	d_1	d_2	τ_{r}	$w_{\mathrm{c}}m/100LW$	C_{total}	Symbol
	V	V/cm	cm	cm	hr	kg/hr m^2	\$/metric ton	
Pilot-scale	28	2.13	62.3	13.1	66.1	1.10	30.17	○
Pilot-scale	62	4.70	62.3	13.2	25.2	2.88	19.92	◐
Pilot-scale	152	11.6	62.3	13.1	10.0	7.27	29.22	●

calculated operational parameters were used to estimate the total cost for a scaled-up continuous single-stage EKD process as shown in Figure 6-1. The total cost at low dry-clay production rates were dominated by the capital cost. As the production rate increased, the capital cost decreased and the operational cost increased due to the increased energy demand.
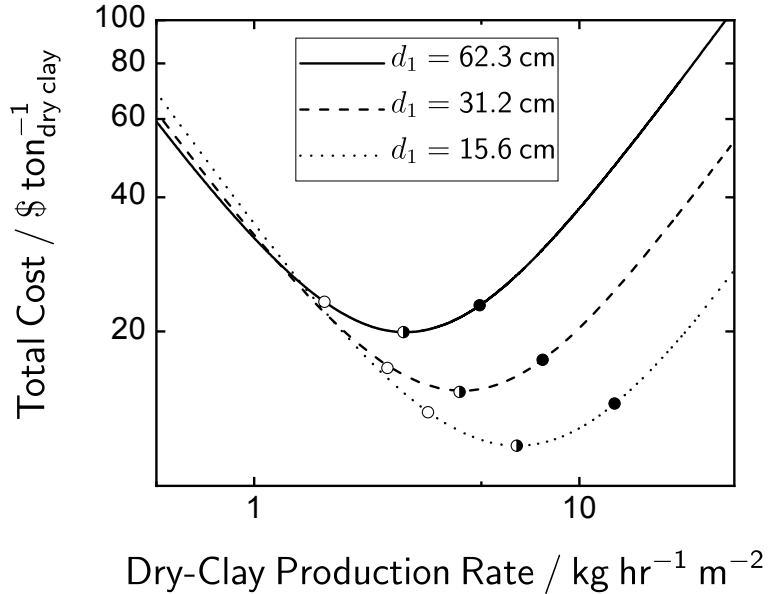
Figure 6-2. The total cost to produce cake with a solids content of 35 wt.% as a function of dry-clay production rate per area of electrode with the feed-side gap as a parameter. The reduction of operating cost was the primary cause of total cost reduction. The operation parameters for the minima and reference points are presented in Table 6-3. Reference points are marked with ○ and ●. The minima are marked with ◗.

6.2   Effect of Electrode Gap on Pilot-Scale Electrokinetic Dewatering

In exploring optimization approaches, the process variables of potential, belt speed, and feed-side gap were varied to find operational modes that reduced the total cost. The most significant reduction on the operating cost was observed when the feed-side gap was reduced as shown in Figure 6-2. The estimated operational data for the minima and reference points are presented in Table 6-3.   The reduction of total cost observed with the reduction of the feed-side gap is attributed to the greater electric fields generated at lower applied potentials. Due to the higher electric field, the reduction of volume between the electrodes was compensated by increased belts speeds, reducing the residence time.

6.3   Pilot-Scale Electrokinetic Dewatering with Electric Field Constraint

The primary driving force for EKD is the electric field. To evaluate the effect of a constant electric field, the applied potential in the simulation was constrained such that

Table 6-3. Operation parameters for reference points and minima from Figure 6-2 for the EKD process with the feed-side gap as a parameter producing a cake with a solids content of 35 wt.% from a feed clay with a solids content of 10 wt.% in Figure 6-2. The symbols match markers used in Figure 6-2, and the cost minima are marked by the symbol ◑.

Conditions	$V_{\max}$ V	$E_{\max}$ V/cm	d_1 cm	d_2 cm	τ_{r} hr	$w_{\mathrm{c}}m/100LW$ kg/hr m^2	C_{total} $/metric ton	Symbol
$d_1 = 62.3$ cm	38	2.88	62.3	13.2	44.1	1.65	23.29	○
$d_1 = 62.3$ cm	62	4.56	62.3	13.6	25.2	2.88	19.92	◑
$d_1 = 62.3$ cm	103	7.89	62.3	13.1	14.7	4.94	22.88	●
$d_1 = 31.2$ cm	31	4.77	31.2	6.5	14.1	2.57	16.55	○
$d_1 = 31.2$ cm	47	7.20	31.2	6.5	8.5	8.47	14.63	◑
$d_1 = 31.2$ cm	81	12.4	31.2	6.5	4.7	7.72	17.27	●
$d_1 = 15.6$ cm	23	7.30	15.6	3.2	5.3	3.42	13.17	○
$d_1 = 15.6$ cm	37	11.3	15.6	3.3	2.8	6.43	11.07	◑
$d_1 = 15.6$ cm	64	20.8	15.6	3.1	1.4	12.9	13.77	●

Table 6-4. Operation parameters for minima and reference points for the EKD process with constant maximum electric fields to produce a cake with a solids content of 35 wt.% from a feed clay of 10 wt.% in Figure 6-3. The symbols match markers used in Figure 6-3, and the cost minima are marked by the symbol ◑.

Conditions	$V_{\max}$ V	$E_{\max}$ V/cm	d_1 cm	d_1 cm	τ_{r} hr	$w_{\mathrm{c}}m/100LW$ kg/hr m^2	C_{total} $/metric ton	Symbol
$E_{\max} = 10$ V/cm	17	10	8.0	1.7	3.2	2.92	15.26	○
$E_{\max} = 10$ V/cm	26	10	12.5	2.6	2.9	5.00	10.93	◑
$E_{\max} = 10$ V/cm	64	10	30.5	6.1	5.8	6.15	15.39	●
$E_{\max} = 15$ V/cm	19	15	6.0	1.3	1.2	5.61	10.14	○
$E_{\max} = 15$ V/cm	27	15	8.5	1.8	1.3	7.58	9.15	◑
$E_{\max} = 15$ V/cm	43	15	13.5	2.9	1.8	8.78	10.74	●
$E_{\max} = 20$ V/cm	20	20	4.7	1.0	0.7	7.93	8.65	○
$E_{\max} = 20$ V/cm	24	20	5.8	1.2	0.7	9.57	8.19	◑
$E_{\max} = 20$ V/cm	38	20	9.1	1.9	0.9	11.45	9.41	●

the maximum electric field was specified. Maximum electric fields of 10, 15, and 20 V/cm were chosen as parameters for simulation. In experiments, an electric field of 15 V/cm produced high-solids-content cake with low ohmic heating such that the cake temperature was less than 100°F. The feed-side gap and belt speed were varied to produce cake with target solids contents of 35 wt.%. The simulation results are shown in Figure 6-3, and the minima and reference point data are presented in Table 6-4.
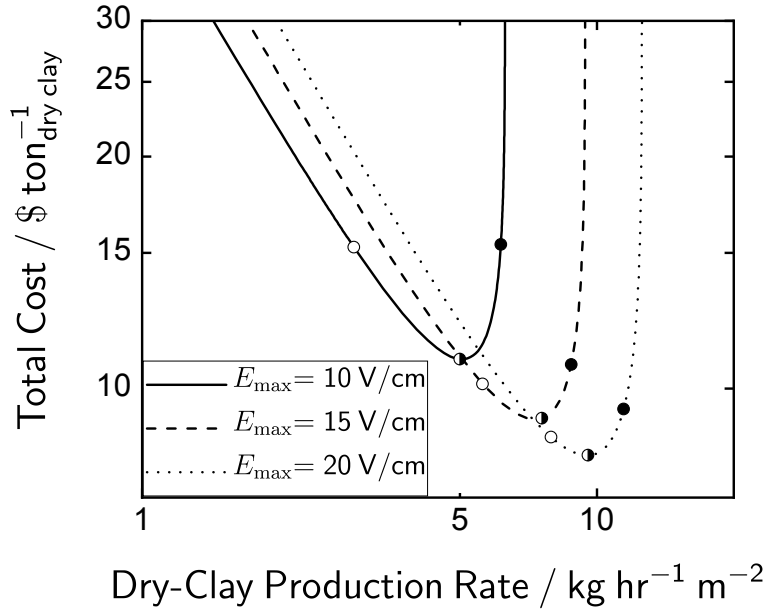
Figure 6-3. The total cost to produce cake with solids contents of 35 wt.% from a feed with a solids content of 10 wt.% with the constraint of a constant maximum electric field of 10, 15, and 20 V/cm. The estimated operating parameters of the minima and reference points are contained in Table 6-4. Reference points are marked with ○ and ●. The minima are marked with ◑.

In Table 6-4, increased electrode gap at a given constant maximum electric field increased the dry-clay production rate. As the gap was increased, a greater applied potential was required to maintain a constant electric field, resulting in a large operational cost. The sharp increase of the total cost at higher dry-clay production rates was dominated by the energy required to maintain the electric field and suggests that there is maximum dry-clay production rate at a given operating electric field. The dependence of the total cost on the feed-side gap is presented in Figure 6-4 where the total cost increased linearly at larger feed-side gaps when maximum electric field is 15 V/cm. Additionally, the residence time also increased linearly with the feed-side gap as shown in Figure 6-5, limiting the dry-clay production rate. The simulations with a constant electric field suggest that the most efficient designs have small electrode gaps and high electric fields while minimizing ohmic heating.
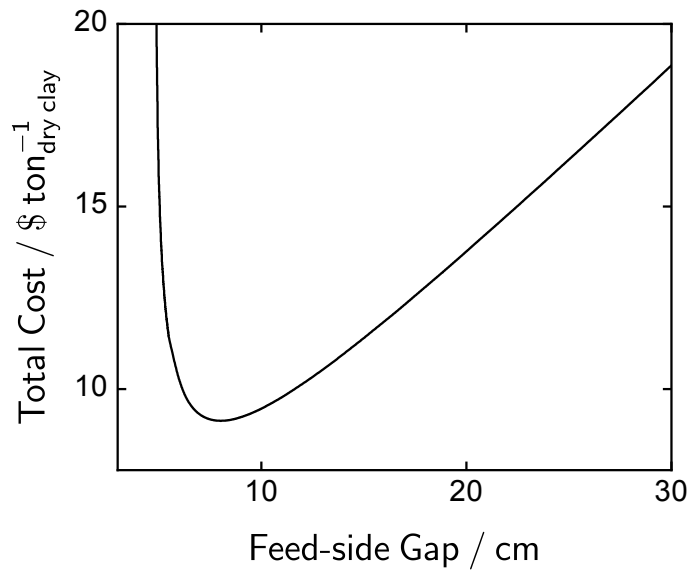
Figure 6-4. The total cost as a function of feed-side gap where the applied potential was constrained to produce a maximum electric field of 15 V/cm. At small feed-side gaps, the total cost increased dramatically due to reduced production rates. At large feed-side gaps, the total cost scales linearly.
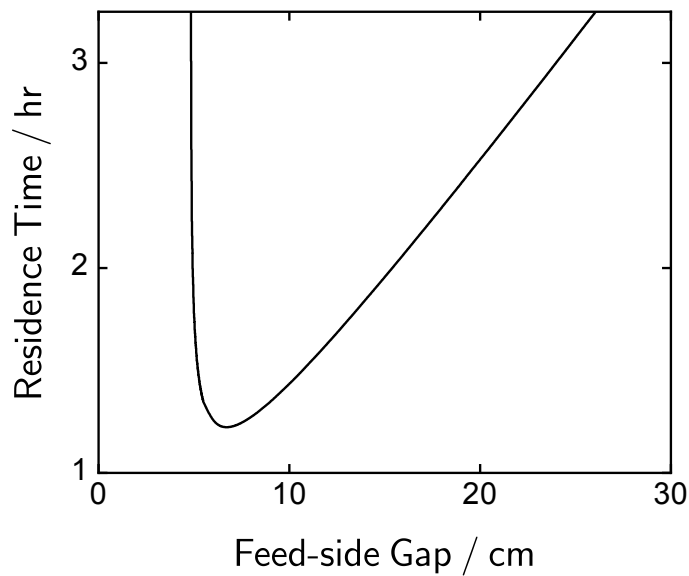
Figure 6-5. The residence time as a function of feed-side gap where the applied potential is constrained to produce a maximum electric field of 15 V/cm. The residence time increases linearly with the feed-side gap. At small feed-side gaps, the residence time increased dramatically due to reduced applied potentials. At large feed-side gaps, the residence time was linearly dependent on the feed-side gap.

The estimated total area of electrode required for full-scale operation was calculated by simulation of a continuous EKD process capable of dewatering the output of a typical phosphate mine. The Mosaic Four Corners Mine produces phosphatic clay with a solids content of 3 wt.% at a rate of 130,00 gallons/min. In order to process the production rate of effluent, a continuous EKD process must produce 1,300 metric tons of dry clay per hour, assuming a final cake solids content of 35 wt.%. Sedimentation of low-solids-content phosphatic clay from a solids content of 3 wt.% to 10 wt.% required on the order of two weeks. The feed for the continuous single-stage EKD process was assumed to have settled to a solids content of 10 w.% prior to performing EKD. The minimal total cost as a function of dry-clay production rate was calculated to determine the required electrode area and operating parameters to produce a cake with a solids content of 35 wt.%. The error in the dry-clay production rate and energy demand were propagated in the calculation of the total cost, total electrode area, and total power demand under the assumption that errors were not correlated.[95]

Simulations result for processing the effluent from the Mosaic Four Corners Mine are presented in Figure 6-6 where the gray region represents the 95% confidence interval estimated by error propagation of the dry-clay production rate and energy demand. The error of the dry-clay production rate and energy demand was obtained from the standard deviation of the experimental values and the values from the data given in Figures 5-5, 5-6, and 5-7. Using the optimal dry-clay production rate, the total electrode area as a function of dry-clay production rate per area of electrode required to treat the Mosaic Four Corners Mine is shown in Figure 6-7. The gray region represents the 95% confidence interval of the electrode area obtained by error propagation of the dry-clay production rate. An estimated 43 acres of electrode are required to treat the effluent from the Four Corners Mine using a maximum electric field of 15 V/cm and producing a cake with a solids content of 35 wt.% from a feed clay with a solids content of 10 wt.%. The simulation results suggest that the opportunities to reduce the required electrode area
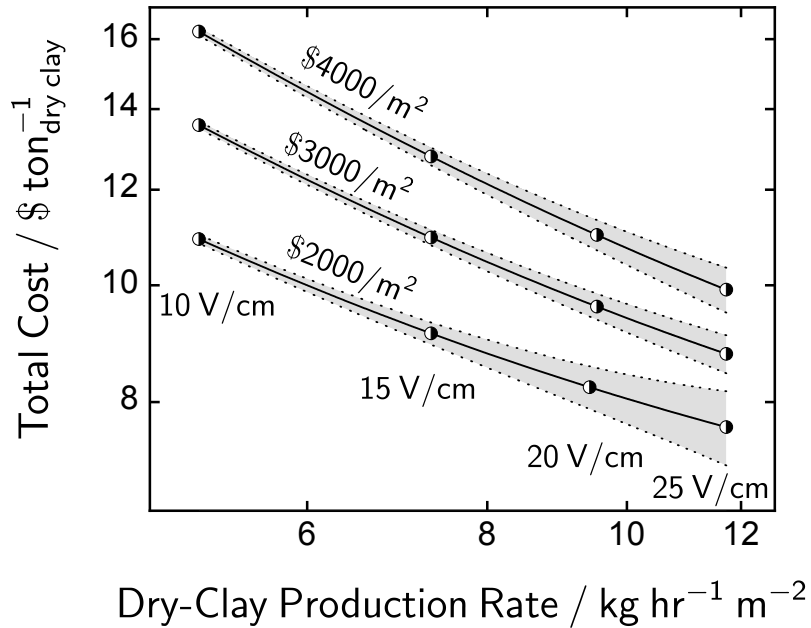
Figure 6-6. Minimal cost to produce a cake with a solids content of 35 wt.% from a feed clay with a solids content of 10 wt.% as a function of dry with initial cost as a parameter. The maximum electric field on the curve is marked by half-black circles ◑. The gray region represents the 95% confidence interval estimated by propagation of error in the energy and dry-clay production rate.

and total cost are in designing a processes capable of operation at greater electric fields. The estimated energy per metric ton of dry clay averaged 110 MW and is shown as a function of dry-clay production rate in Figure 6-8, where the gray region represents the 95% confidence interval estimated by error propagation as described in the generation of Figure 6-6.
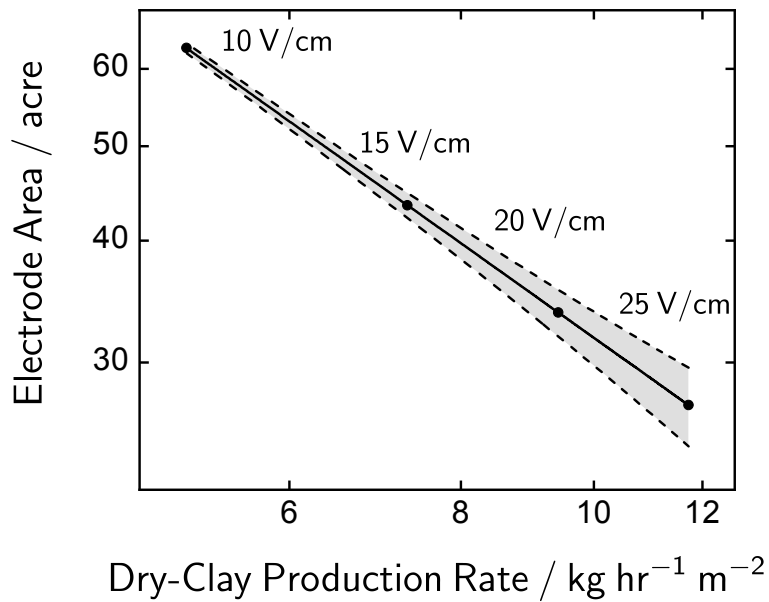
Figure 6-7. The total electrode area required to process the Four Corners Mine as a function of the dry-clay production rate per unit area of electrode using the model based on the scale-up of the optimized continuous EKD process in producing a cake with a solids content of 35 wt.% from a feed clay with a solids content of 10 wt.%. The gray region represents the 95% confidence interval estimated by propagation of error in dry-clay production rate.
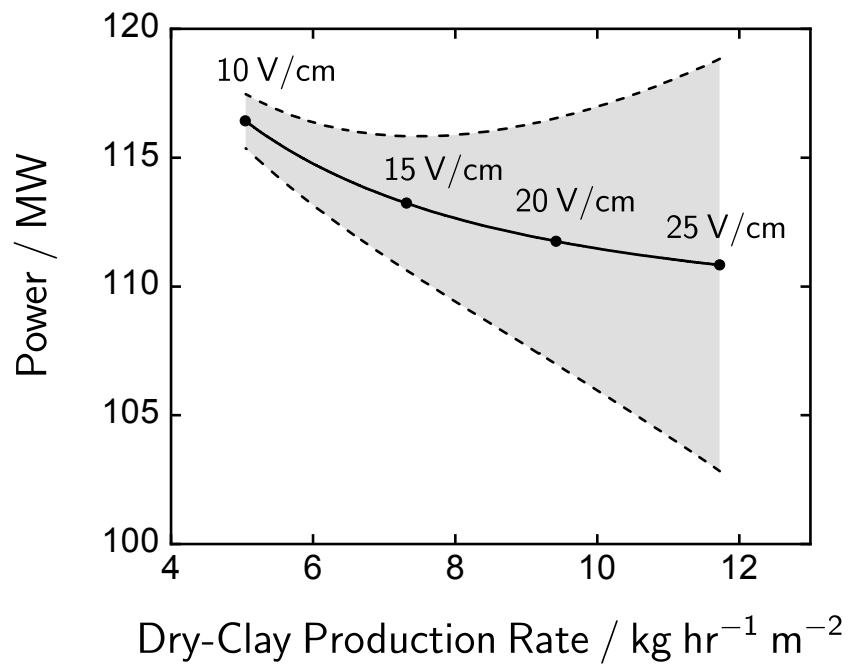
Figure 6-8. The total power required to process the output of the Mosaic Four Corners
Mine to a solids content of 35 wt.% as a function of dry-clay production rate.
The gray region represents the 95% confidence interval estimated by
propagation of error in the energy and dry-clay production rate.

CHAPTER 7
INTERDIGITATED MICROELECTRODES

Interdigitated electrodes (IDE) are microelectrodes deposited onto a substrate such that the working and counter electrodes have the appearance of interlaced electrode fingers separated by a small distance, as shown in Figure 7-1. The micron-scale separation between the working and counter electrodes served to increase the sensitivity for EIS measurements. The high-sensitivity of IDE allows for electrochemical analysis of small sample sizes. The current use of IDE in resistivity measurements requires a value for the cell constant K_{cell}, given by

$$K_{\text{cell}} = \frac{R_{\text{e}}}{\rho} \tag{7-1}$$

where R_{e} is the ohmic resistance of the cell (Ω) and ρ is the resistivity of the electrolyte. The cell constant shown in equation (7-1) has units of cm^{-1}. The cell constant can be related to the a characteristic dimension of the cell δ following

$$\delta = K_{\text{cell}} A_{\text{IDE}} \tag{7-2}$$

where A_{IDE} is the total area of the electrode. The cell constant can be obtained experimentally using equation (7-1) or mathematically by solving Laplace's equation using finite-elements or conformal mapping.

7.1   Previous Work

Zaretsky et al.[96] developed a mathematical framework for the relationship between surface capacitance and the periodic interdigitated electrode microstructure for dielectrometry, which is the measurement of the relative permittivity with alternating current. The earliest fabrication of platinum interdigitated electrodes with a digit width of 3.5 μm and a digit spacing of 2.5 μm was achieved by Chidsat et al.[97] Zou et al. demonstrated the fabrication of nanometer-scale electrodes designed for bioimpedance measurements.[98] Skjolding et al.[99] concluded that optimal signal sensitivity occurred with electrode widths of less than 1 μm through the kinetic studies
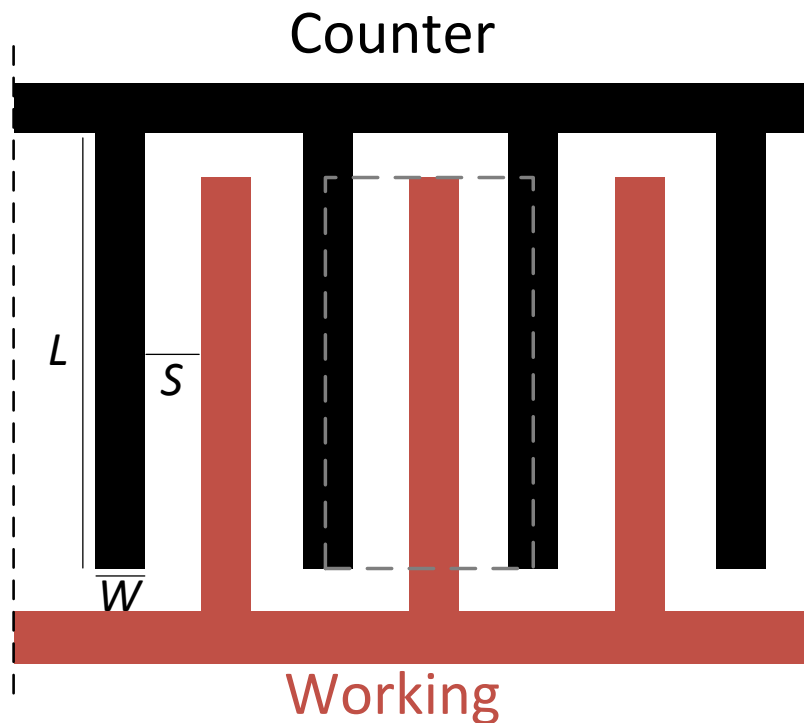
Figure 7-1. Schematic representation of an IDE from a top down view where the width of a digit is represented by W, the length of a digit is represented by L, and the spacing between digits is represented by S. The working electrode is red and the counter electrode is black.

of nano-interdigitated electrodes. Pliquett et al.[100] demonstrated an increase in the noise of impedance measurements with reduced digit width. Ibrahim et al.[101] optimized interdigitated electrode sensitivity through finite-element simulations and concluded that the optimal ratio of digit spacing and width was 0.66. Jeon et al.[102] fabricated nano-gap interdigitated aluminum electrodes and showed that fabrication defects at electrode edges contributed to deviations from predicted results.

Hong et al.[103] attributed experimental departures from theoretically predicted impedance to the dielectric response of the substrate and overlapping of double-layers (fringing). A dual-channel interdigitated electrode was developed by Chen et al.[104] to mitigate the effect of the substrate on capacitive measurements. Tomčík[105] accounted for overlapping diffusion layers of the interdigitated electrodes and the effect on impedance. A mathematical framework for the effect of multiple layers deposited on the surface

of an interdigitated electrode was developed by Blume et al.[106]. MacKay et al.[107] studied increasing the sensitivity of IDEs by performing simulations of gold nano-particles adhered to the surface of gold interdigitated electrodes. The simulations predicted that the nano-particles adhered to the electrode surface disrupted the screening effect of the ions in solutions.

7.2   Applications of Interdigitated Electrodes

The primary use of the interdigitated electrode is as an electrochemical sensor. Bueno and Paixão[108] studied the use of copper interdigitated electrodes to detect adulteration of ethanol with water by the dielectrometry. The analysis showed that the method was accurate in detecting adulteration in mixtures of 10 to 25 vol.% of water in ethanol. Staginus[109] studied the application of interdigitated electrodes for the detection of organic pollutants. Mohamad et al.[110] studied the detection of triglyceride in hexane. Matylitskaya et al.[111] studied the kinetics on nano-scale interdigitated electrodes for lab-on-a-chip applications and observed reduced sensitivity resulting from surface films. Label-less detection of cancer cell and viruses is a common application of interdigitated electrodes where the electrode surfaces are functionalized to detect specific cell types and viruses.[112–117]

7.3   Structure of Interdigitated Electrodes

An IDE is a microelectrode with interlaced fingers, as shown in Figure 7-1. The electrode dimensions of the electrode are given by the width W, the length L, and the spacing between digits S. The number of fingers or digits n_{IDE} can vary depending design. The total area of the electrode is given by

$$A_{\text{IDE}} = n_{\text{IDE}} LW \qquad (7\text{-}3)$$

where $_{\text{IDE}}$ is the number of digit electrode pairs. A side-view cross section of an IDE is shown in Figure 7-2. An scanning transmission electron microscope image of a DropSens IDE (IDEAU5) provided an estimate of 120 nm for the height of an electrode.[118]

86

Counter

½ W

W

Counter

½ W

H

S

Working

Glass Substrate
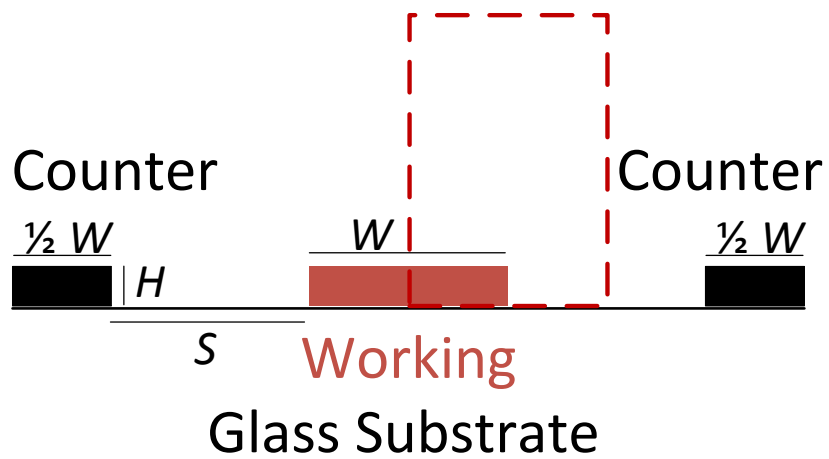
Figure 7-2. Schematic representation of the profile of an IDE where the width of a digit is represented by W, the height of a digit is represented by H, and the spacing between digits is represented by S. The working electrode is red and the counter electrode is black. The red dashed box encapsulates the unit cell for simulations.

CHAPTER 8
ELECTROCHEMICAL IMPEDANCE SPECTROSCOPY

Electrochemical impedance spectroscopy (EIS) is an experimental method used to provide insight into electrochemical processes such as charging, diffusion, and electrochemical reactions. In EIS, a sinusoidal perturbation of electrical potential or current is applied to a an electrochemical system as shown in Figure 8-1. The ratio of the sinusoidal potential perturbation to the complex current response is the frequency-dependent transfer function called impedance. Application of a sinusoidal potential perturbation is referred to as potentiostatic modulation; whereas, imposition of a perturbed current input signal is called galvanostatic modulation.

The input perturbation and resulting response are shown in Figure 8-2. The amplitude of each signal is denoted by the Δ prefix. The phase lag between the input and output waves is represented by the phase angle φ. For an electrical potential sinusoidal input, the time-domain potential can be represented in the frequency domain by

$$\Phi(t) = \bar{\bar{\Phi}} + |\Delta V| \cos{(\omega t)} \tag{8-1}$$

and the time-domain current

$$I(t) = \bar{I} + |\Delta I| \cos{(\omega t - \varphi)} \tag{8-2}$$

where the overbar indicates the steady-state portion of the signal and the cosine term represents the oscillation. The oscillation is characterized by the wave amplitudes, $|\Delta \Phi|$
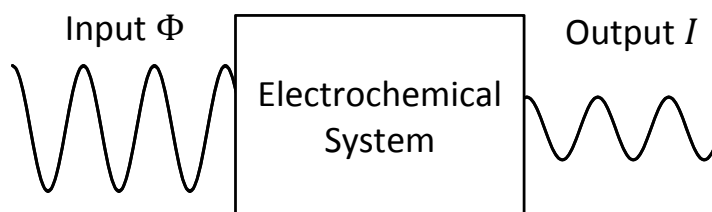
Figure 8-1. A schematic representation of galvaostatic EIS where a sinusoidal electric potential perturbation is applied to an electrochemical system and the sinusoidal current response is measured.
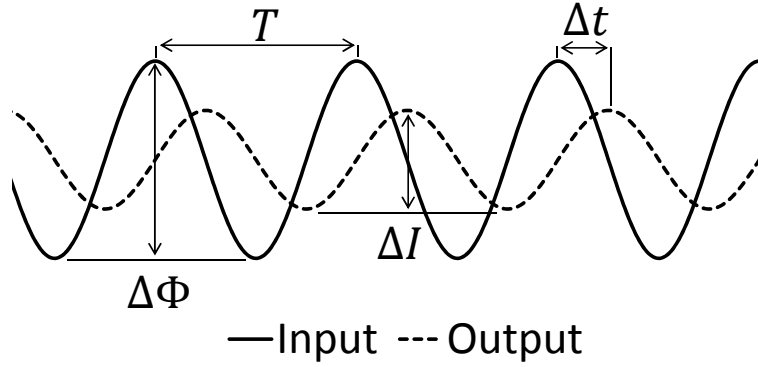
Figure 8-2. A schematic representation of a sinusoidal electrical potential perturbation and the resulting current response.

and $|\Delta I|$, the wave frequency ω, and the phase angle. Equations (8-1) and (8-2) can be expressed in phasor notation as

$$\Phi(t) = \bar{\Phi} + \text{Re}\{\tilde{\Phi}e^{j\omega t}\} \tag{8-3}$$

and

$$I(t) = \bar{I} + \text{Re}\{\tilde{I}e^{j\omega t}\} \tag{8-4}$$

where the time-domain potential and current are expressed respectively as the sum of steady-state potential $\bar{\Phi}$ and current $\bar{I}$ and the real part of the oscillating potential $\text{Re}\{\tilde{\Phi}\exp^{j\omega t}\}$ and oscillating current $\text{Re}\{\tilde{I}\exp^{j\omega t}\}$. $\tilde{\Phi}$ and $\tilde{I}$ are complex numbers. The impedance Z is defined as

$$Z(\omega) = \frac{\Delta\tilde{\Phi}}{\tilde{I}} \tag{8-5}$$

and is a complex number that can be expressed as the sum of the real and imaginary parts,

$$Z_{\text{r}} = |Z(\omega)| \cos(\varphi) \tag{8-6}$$

and

$$Z_{\text{j}} = |Z(\omega)| \sin(\varphi) \tag{8-7}$$

The Δ indicates a potential difference. The frequency dependence of impedance allows insight into the electrochemical processes.

8.1   Graphical Representation

Impedance can be represented graphically in multiple ways which are dependent on the desired information. Bode plots represent the modulus

$$|Z| = \sqrt{Z_r^2 + Z_j^2} \tag{8-8}$$

and phase angle

$$\varphi = \tan^{-1}\left(\frac{Z_j}{Z_r}\right) \tag{8-9}$$

In systems with large ohmic resistances, Bode plots can be misleading at high frequencies.

A Nyquist plot is common method of presenting impedance response and consists of the imaginary part Z_j as a function of the real part Z_r with frequency as a parameter, as shown in Figure 8-3. The real part is commonly associated with resistive properties of the electrical cell; whereas, the imaginary part is associated with inductive and capacitive behaviors. High-frequency features in Nyquist plots can be difficult to discern.

8.2   Characteristic Dimension

The geometry of the electrodes plays a role in the impedance response obtained from the electrochemical cell. In the case of a resistive and dielectric medium between two parallel plate electrodes, the resistance R_e in units of Ωcm^2 is given by

$$R_e = \rho\delta \tag{8-10}$$

where ρ is resistivity of the medium in units of Ωcm and δ is the characteristic dimension of the electrode. For a parallel-plate electrode configuration, the characteristic dimension is the normal distance between the plates. Similarly, the capacitance of the described cell is given as

$$C = \frac{\epsilon_r \epsilon_0}{\delta} \tag{8-11}$$

where ϵ_r is the dielectric constant of the medium, ϵ_0 is the vacuum permittivity, and δ is the characteristic length as equation (8-10). The Nyquist representation of the described cell is a semi-circle, similar to the examples given in Figure 8-3, where the diameter of the

90
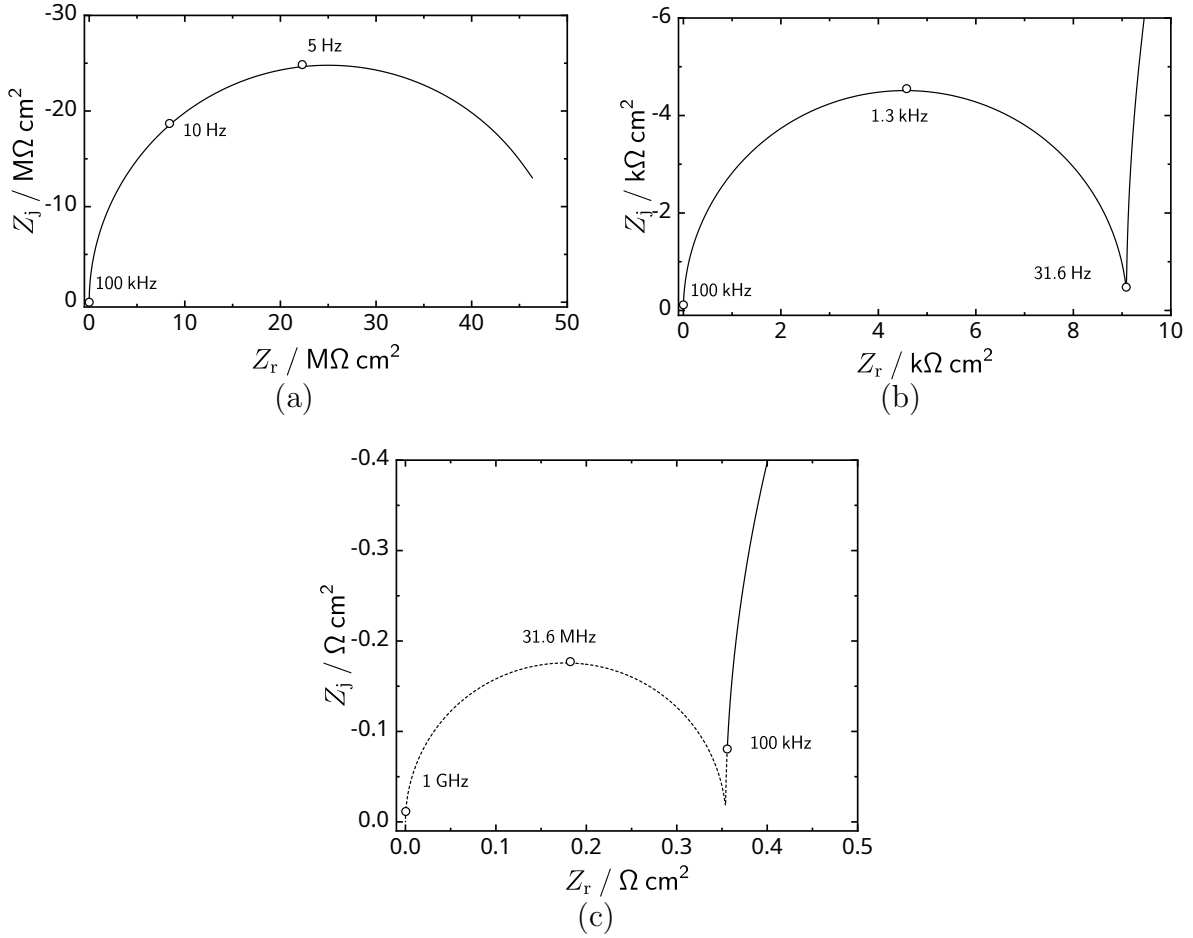
Figure 8-3. Nyquist plots of oil, deionized water, and 10 mM KCl. All plots assumed a double-layer capacitance of 20 μF/cm^2. (a) Nyquist plot for oil with a conductivity of 1×10^{-11} S/cm and a dielectric constant of 4. (b) Nyquist plot for deionized water with a conductivity of 5.5×10^{-8} S/cm and a dielectric constant of 78. (a) Nyquist plot for oil with a conductivity of 1.41×10^{-3} S/cm and a dielectric constant of 78. The dotted line represents impedance data above 100 kHz which is beyond the reliable measurement range for frequency.

circle is the ohmic resistance R_e and the characteristic frequency

$$f_c = \frac{1}{2\pi R_e C} \tag{8-12}$$

corresponds to the top of the semi-circle. The ohmic resistance of a disk electrode embedded in an insulating plane is given by

$$R_e = \frac{\pi \rho r_0}{4} \tag{8-13}$$

where the r_0 is the radius of the disk.[119] The characteristic dimension for a disk electrode is the radius of the disk r_0.

8.3 Frequency Dispersion

Frequency dispersion is observed in experimental and simulated impedance. Fricke[120] used a constant-phase element (CPE) in place of a standard capacitor as a method used to account for the effect of frequency dispersion in an electrochemical system. The CPE is a frequency dependent element given by

$$Z_{\mathrm{CPE}} = \frac{1}{(\mathrm{j}\omega)^{\alpha} Q} \tag{8-14}$$

where α and Q are parameters. When the value of α is equal to unity, the parameter Q is a capacitance. In cases where α is less than unity, the meaning of Q is not fully understood. CPE behavior is attributed to electrochemical cells effected by porous electrodes, geometry, diffusion, or a distribution of resistivity. Alexander et al.[121–123] published a series of papers on the origins of constant-phase element behavior resulting from surface distributions. Constant-phase-element behavior attributed to normal distributions of resistivity and permittivity has been presented in the work of Orazem et al.[124], Musiani et al.[125], and in a series of papers by Hirschorn et al.[126–128]

8.4 Analysis and Interpretation

Measured electrochemical impedance responses were validated by evaluating the consistency between the real and imaginary parts of the impedance using the Kramer–Kronig relations. Conditions for application of the Kramers–Kronig relations are that the system is linear, stable, and causal. If impedance data satisfy the Kramers–Kronig relations, then the data were assumed to be linear, stable, and causal. Consistency with the Kramers–Kronig relations was analyzed by fitting EIS data with a measurement model consisting of Voigt elements as presented in the work by Agarwal et al.[129] Voigt elements are Kramers–Kronig consistent. If impedance data can be successfully fit with Voigt elements, then by extension the data set is Kramers–Kronig consistent. The

nonlinear regression to a series of Voigt elements was achieved via nonlinear regression with a Levenburg–Marquart algorithm. The algorithm allows not only the extraction of parameters but also confidence intervals of the extracted parameters.

CHAPTER 9
FINITE-ELEMENT MODELING OF INTERDIGITATED ELECTRODES

Modeling of IDE was achieved by a 2-D finite-element method using COMSOL®. COMSOL® uses a LU decomposition methods for systems that can be directly solved and conjugate gradient methods for systems requiring an iterative solution. The computer used to perform the calculation was a Dell™ Precision T7500 workstation with two E5620 2.4 GHz Intel® Xeon® processors and 96 GB of RAM.

9.1 Mathematical Development

The equation solved was conservation of current, i.e.,

$$\nabla \cdot \mathbf{i} = 0 \tag{9-1}$$

where $\mathbf{i}$ is the current density vector

$$\mathbf{i} = \kappa \mathbf{E} + \frac{\partial}{\partial t} \mathbf{D} \tag{9-2}$$

κ is the electrical conductivity, $\mathbf{E}$ is the electric field vector, and $\mathbf{D}$ is the electrical displacement vector. The electrical displacement vector was estimated using the constitutive relationship

$$\mathbf{D} = \epsilon_{\mathrm{r}} \epsilon_0 \mathbf{E} \tag{9-3}$$

The electric field vector is related to the electrical potential by

$$\mathbf{E} = -\nabla \Phi \tag{9-4}$$

Substitution of equations (9-2) to (9-4) into equation (9-1) and transformation into the frequency domain, yields

$$\nabla \cdot (\kappa + \mathrm{j}\omega\epsilon_{\mathrm{r}}\epsilon_0) \nabla \Phi = 0 \tag{9-5}$$

Under the assumption of a zero steady-state current, the phasor notation of equation (9-1) is expressed as

$$\nabla \cdot (\kappa + \mathrm{j}\omega\epsilon_{\mathrm{r}}\epsilon_0) \nabla \mathrm{Re}\{\tilde{\Phi} \exp^{\mathrm{j}\omega t}\} = 0 \tag{9-6}$$

The boundary conditions used to calculate the impedance are given by expressions for the current density at the working and counter electrodes. The normal current density at an electrode was expressed in the time domain as

$$\mathbf{n} \cdot \kappa \nabla \Phi = C_{\mathrm{dl}} \frac{\partial}{\partial t} \left(\Phi_{\mathrm{m}} - \Phi \right) \tag{9-7}$$

and in the frequency domain,

$$\mathbf{n} \cdot \kappa \nabla \tilde{\Phi} = \mathrm{j}\omega C_{\mathrm{dl}} \left(\tilde{\Phi}_{\mathrm{m}} - \tilde{\Phi} \right) \tag{9-8}$$

where $\mathbf{n}$ is the unit normal vector and the potential of the metal is Φ_{m}. The resulting boundary conditions for the working and counter electrodes were

$$\mathbf{n} \cdot \kappa \nabla \tilde{\Phi} = \mathrm{j}\omega C_{\mathrm{dl}} \left(\tilde{\Phi}_{\mathrm{m}} - \tilde{\Phi} \right) \tag{9-9}$$

and

$$\mathbf{n} \cdot \kappa \nabla \tilde{\Phi} = \mathrm{j}\omega C_{\mathrm{dl}} \left(-\tilde{\Phi}_{\mathrm{m}} - \tilde{\Phi} \right) \tag{9-10}$$

The amplitude of the perturbation was $2\tilde{\Phi}_{\mathrm{m}}$. The boundary condition for the insulating walls was $\mathbf{n} \cdot \nabla \tilde{\Phi} = 0$.

9.2 Interdigitated Electrode Structure

The unit cell assembled in COMSOL® for simulations is shown in Figure 7-2. The total height of the domain is H_{dom}. A magnified schematic representation of Figure 9-1 near the electrodes is shown in Figure 9-2. The dimensions are also depicted in Figure 7-2. The edges between the working and counter electrodes were designated as insulators. The height of the domain was large enough to ensure that the influence of the top boundary was negligible. The meshing scheme at the electrodes was made fine enough as to ensure accurate calculation of the current.

9.3 Domain and Meshing

The domain size H_{dom} and meshing size at the electrodes were determined by varying the size of each and extracting the effective resistance and capacitance. The resistance and

$$\mathbf{n} \cdot \tilde{\mathbf{i}} = 0$$

$$\mathbf{n} \cdot \tilde{\mathbf{i}} = 0 \qquad \mathbf{n} \cdot \tilde{\mathbf{i}} = 0$$
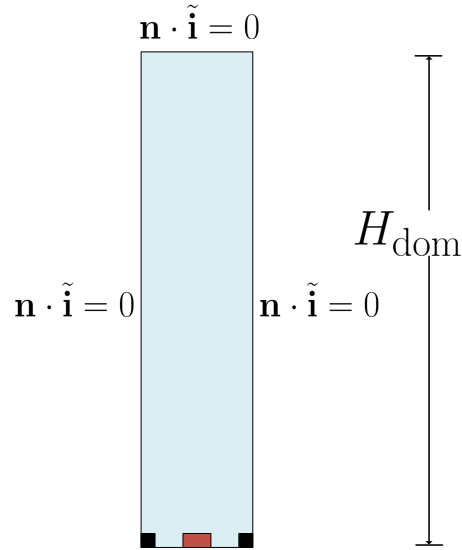
$$H_{\mathrm{dom}}$$

Figure 9-1. Schematic representation of the full simulation domain. The blue region is the 2-D shape used for simulation. The total height of the blue region is represented by H_{dom}. The top, left, and right edges are insulating planes and labeled with the boundary conditions. The working electrode is red and the counter electrode is black. The boundary conditions at the electrodes are shown in Figure 9-1.

$$\mathbf{n} \cdot \tilde{\mathbf{i}} = \mathrm{j}\omega C_0 \left(-\tilde{\Phi}_{\mathrm{m}} - \tilde{\Phi} \right)$$

$$\mathbf{n} \cdot \tilde{\mathbf{i}} = \mathrm{j}\omega C_0 \left(\tilde{\Phi}_{\mathrm{m}} - \tilde{\Phi} \right)$$

$$\mathbf{n} \cdot \tilde{\mathbf{i}} = 0$$
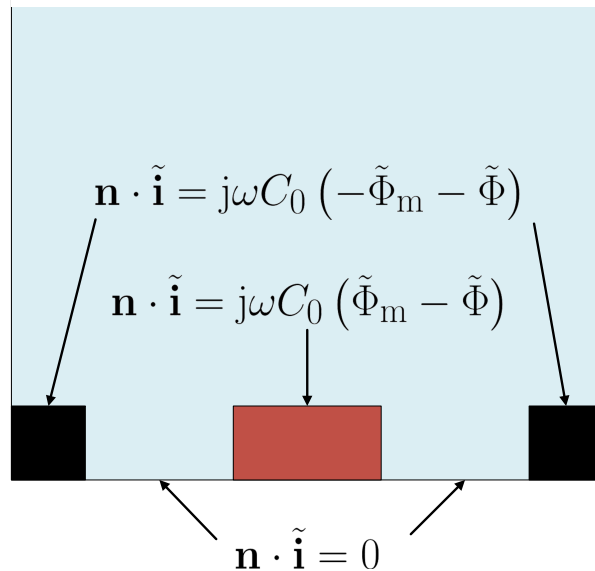
Figure 9-2. Schematic representation of the simulation domain near the electrodes. The blue region is the 2-D shape used for simulation. The working electrode is red and the counter electrode is black. The interior edges of the electrodes are labeled with the phasor boundary conditions stating the passage of current. The dimensions are given as described in Figure 7-2.

Figure 9-3. The resistance and capacitance as a function of the domain size. As the domain size was increased, the resistance and capacitance approached asymptotic values.

capacitance were extracted assuming a total impedance model

$$Z = \frac{R_e}{1 + j\omega R_e C_{\text{eff}}} + \frac{1}{j\omega C_{\text{dl}}} \tag{9-11}$$

As the domain size was increased, the extracted resistance and capacitance approached asymptotic values as shown in Figure 9-3. The asymptotic values for resistance and capacitance obtained by

$$R_e = R_{e,\infty} + m_R H_{\text{dom}}^{-n_R} \tag{9-12}$$

and

$$C_{\text{eff}} = C_{\text{eff},\infty} + m_C H_{\text{dom}}^{-n_C} \tag{9-13}$$

where m_R, m_C, n_R, and n_C are regressed constants that quantify the approach to asymptotic values when $H_{\text{dom}} \to \infty$. The regressed values of $R_{e,\infty}$ and C_{∞} were 6.701±0.0011 Ωcm^2 and 13.855±0.0022 nF/cm^2, respectively. The regressed values of m_R and m_C were 2017±500 Ωcm$^2\mu$m^{n_R} and -2776±610 nFμm^{n_C}/cm^2, respectively. The
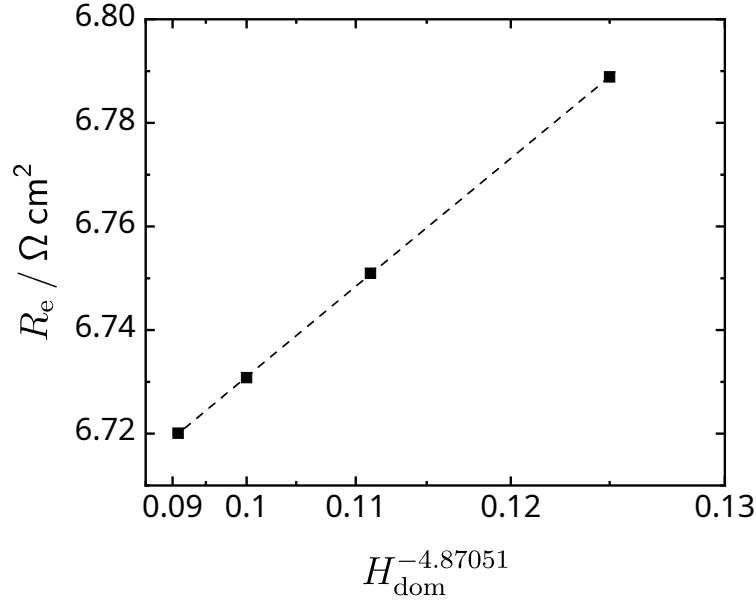
Figure 9-4. The resistance as a function of the domain size. As the domain size was increased, the resistance approached an asymptotic value.

values of n_R and n_C were 4.87±0.13 and 4.63±0.11, respectively. The approach towards asymptotic values of resistance and capacitance are shown in Figures 9-4 and 9-5. The percent error between the asymptotic values of resistance and capacitance were also calculated as a function of domain size as shown in Figures 9-6 and 9-7. A domain size of 50 or 100 μm was used for all simulations which corresponded to an percent error of 0.1% for resistance and 0.01% for capacitance. Due to round-off error and error associated with the mesh used, the resistance and capacitance reached asymptotic values that differed from $R_{e,\infty}$ and C_∞, as shown in Figure 9-3.

The mesh at the electrode was varied by adjusting the dimension of the maximum element size of the bottom edges of the domain. As the maximum element size was decreased, the resistance and capacitance approached asymptotic values as shown in Figures 9-8 and 9-9. The asymptotic values of the effective resistance and capacitance were assumed to be of the form

$$R_e = R_{e,0} + m_R s^{n_R} \tag{9-14}$$

98
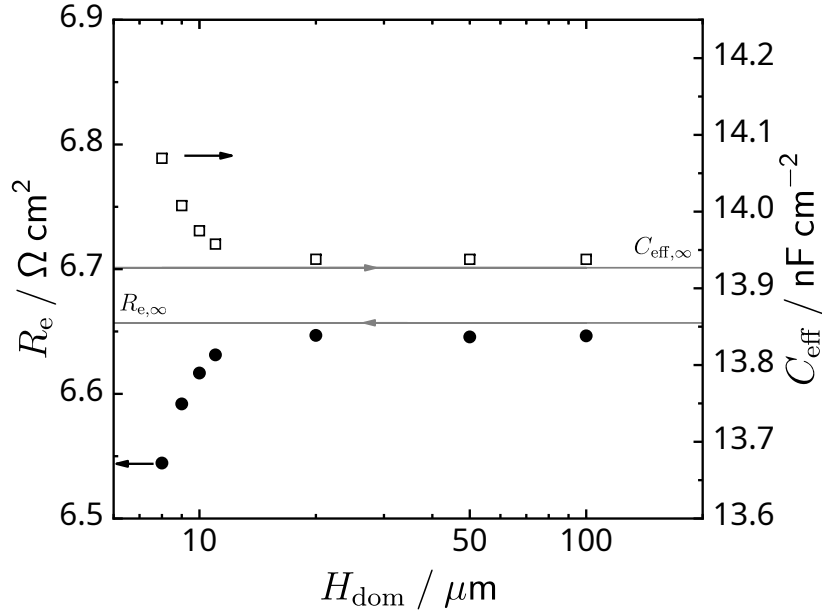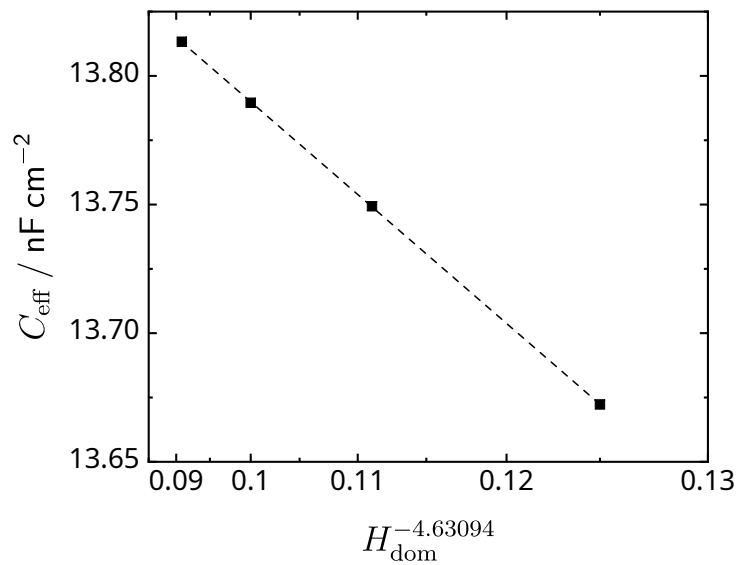
Figure 9-5. The capacitance as a function of the domain size. As the domain size was increased, the capacitance approached an asymptotic value.
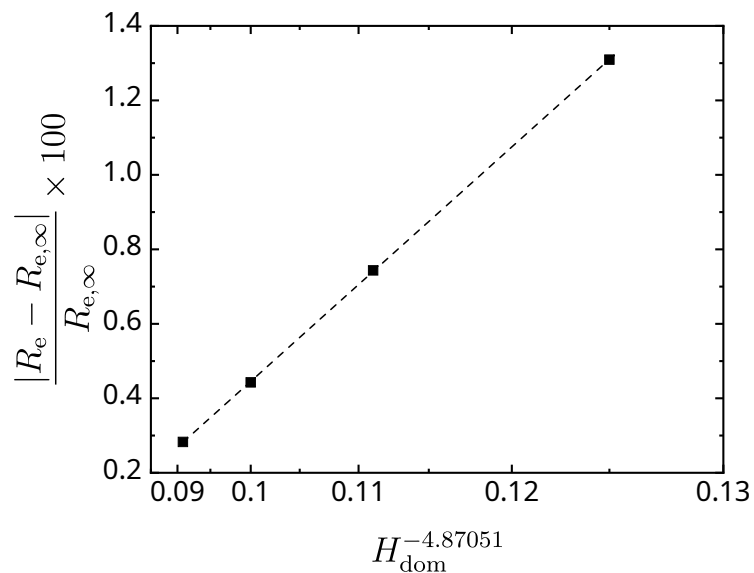
Figure 9-6. The percent error resistance as a function of the domain size. As the domain size was increased, the error decreased.
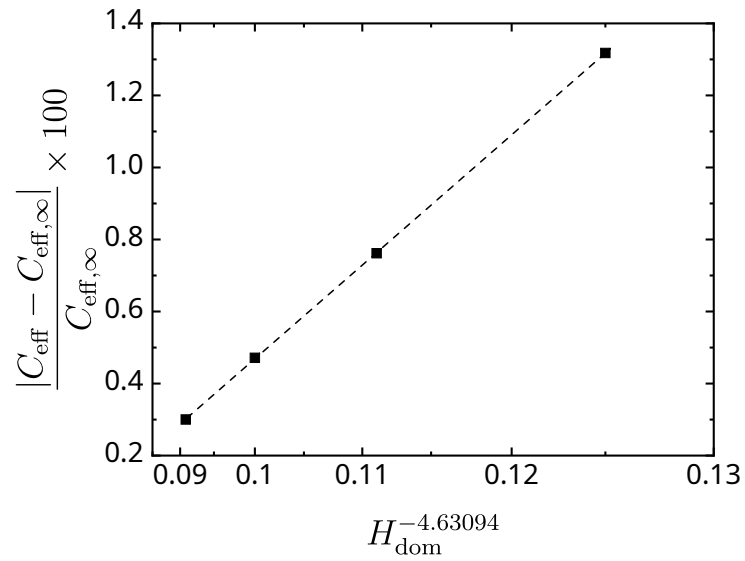
Figure 9-7. The percent error capacitance as a function of the domain size. As the domain size was increased, the error decreased.
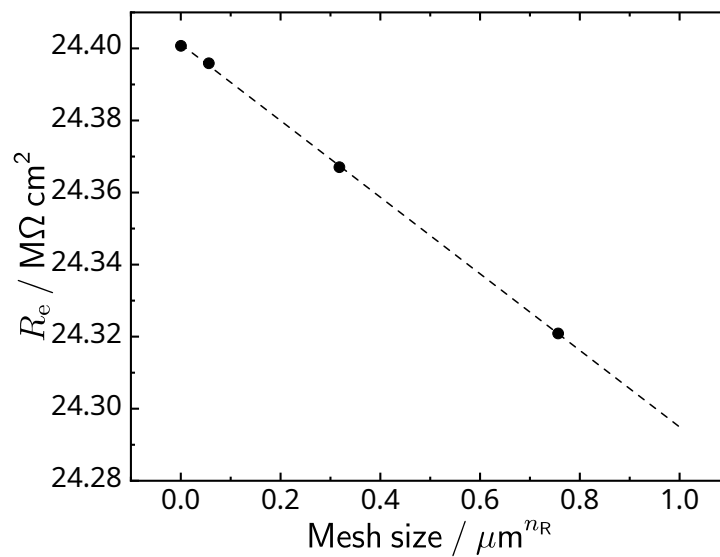
Figure 9-8. The resistance as a function of the maximum element size at the electrodes. As the mesh size was decreased, the resistance approached an asymptotic value.
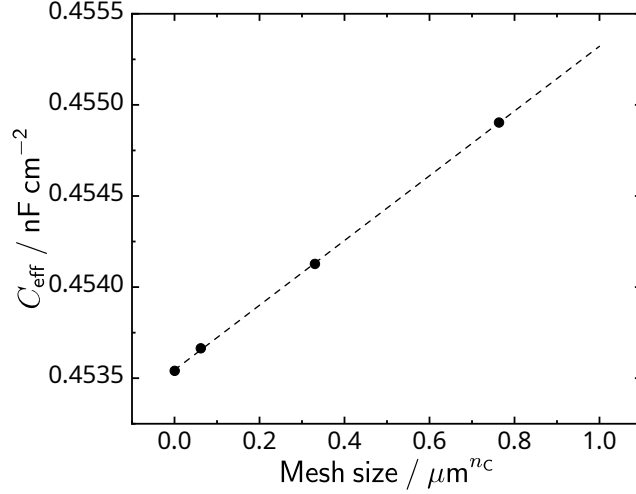
Figure 9-9. The capacitance as a function of the maximum element size at the electrodes. As the mesh size was decreased, the capacitance approached an asymptotic value.

and

$$C_{\text{eff}} = C_{\text{eff},0} + m_{\text{C}} s^{n_{\text{C}}} \tag{9-15}$$

where m_{R} and m_{C} are slopes for the error, and n_{R} and n_{C} are fitted constants. The percent error approached zero for both the effective resistance and capacitance as the mesh size was decreased, as shown in Figure 9-10. The extrapolated resistance and capacitance were 24401.2±0.77 kΩcm^2 and 0.454±0.00001 nFcm^{-2}, respectively. The resistance slope m_{R} and capacitance slope m_{C} were -106 ± 1.7 k$\Omega\mu$m$^{-\text{n}_{\text{R}}}$ and 1.78±.02 pF μm$^{-\text{n}_{\text{C}}}$, respectively. The constants n_{R} and n_{C} had values of 1.25±0.04 and 1.21±0.04, respectively. The percent error between the extrapolated value and the simulated value at a given mesh dimension is shown in Figure 9-10. Images of the meshing used for simulations are shown in Figures 9-11, 9-12, and 9-13. The final domain height of the simulations was set at 100 μm. The error due to round off was estimated from the standard deviation of the resistance and capacitance values for domain sizes greater than 40 μm. The estimated round-off error for the resistance and capacitance were 0.0002% and 0.007%, respectively. The percent error for the resistance
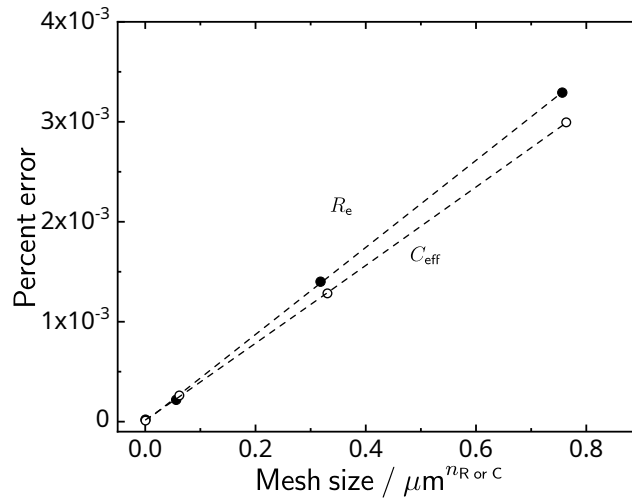
Figure 9-10. The percent error of resistance and capacitance as a function of the maximum element size at the electrodes. As the mesh size was decreased, the percent error of resistance and capacitance approached zero.
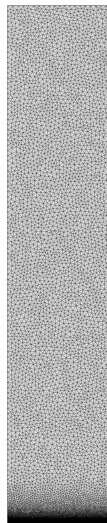
Figure 9-11. Image of the fully meshed domain used for simulation.
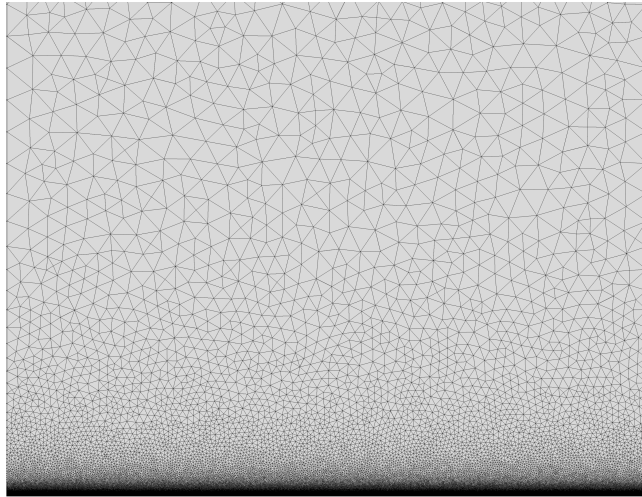
Figure 9-12. Magnified image of the fully meshed domain near the electrode used for
simulation.
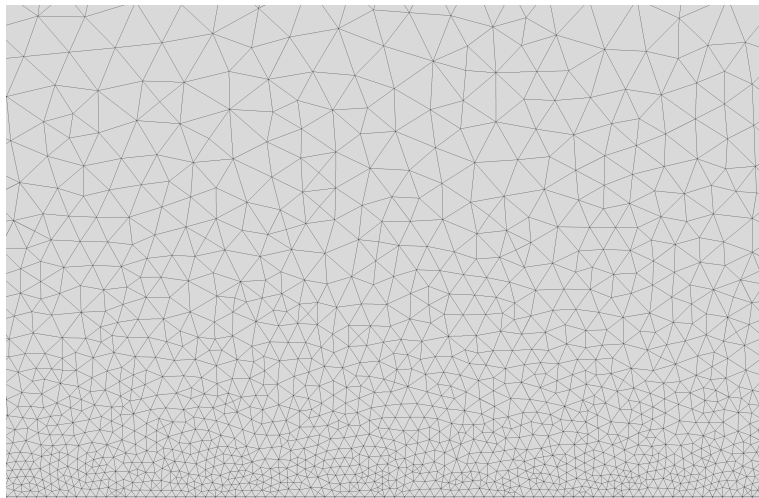
Figure 9-13. Higher magnification image of the fully meshed domain at the electrode used
for simulation.

and capacitance associated with the mesh size at the electrode were 0.0003% and 0.001%. The estimate for the total percent error for the domain size of 100 μm and a maximum mesh size of 1 nm was 0.0003% for resistance and 0.007% for capacitance.

9.4   Characteristic Dimension and Frequency

As shown in equations (8-10) and (8-11), the observed resistance and capacitance are related to the resistivity and dielectric constant by a characteristic dimension. The characteristic dimension for the geometric capacitance is a result of the geometry of the electrodes in the electrochemical cell. The method employed to determine the characteristic dimension was to simulate the effective resistance and capacitance with the solution resistivity and dielectric constant as input parameters. The characteristic dimension was then obtained using equations (8-10) and (8-11). The characteristic frequency at which the influence of geometric capacitance is apparent is dependent on the resistivity and dielectric constant of the medium, i.e..

$$f_{\mathrm{c}} = \frac{1}{2\pi\rho\epsilon_0\epsilon_{\mathrm{r}}} \tag{9-16}$$

If the frequencies at which geometric capacitance are visible were significantly greater than the reliably measurable range, then estimation of the ohmic resistance was difficult. The characteristic frequencies of geometric capacitances are shown in Figure 9-14 and were calculated using equation (8-12) at various dielectric constants.

9.4.1   Effect of Digit Height

Most of the surface area of the electrode is on the top planar surface of the digits. The finite height of the digits affects the potential and current distributions on the electrode surfaces. Simulations were performed for oil as the medium for which the resistivity was 69 GΩ cm and a dielectric constant of 4 where the height of the electrode was varied from 0 to 5 μm. The effective ohmic resistance and geometric capacitance were extracted by nonlinear regression. The characteristic dimension was then calculated for each simulation and scaled by the characteristic dimension obtained corresponding
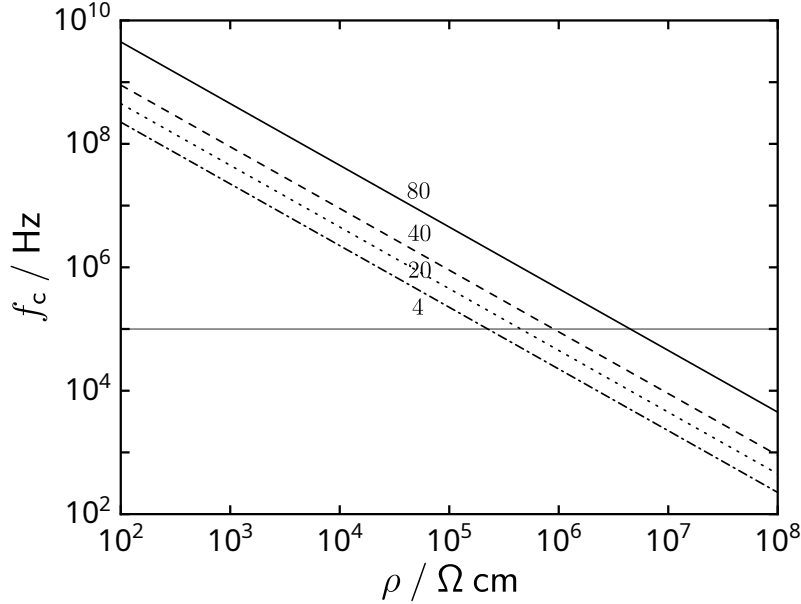
Figure 9-14. Characteristic frequency of geometric capacitance as a function of resistivity with the dielectric constant as a parameter. Characteristic frequencies greater and 10^5 Hz are often unreliable due to noise and error in measurement. The horizontal gray line marks 10^5 Hz. Geometric capacitance is most visible in media with high resistivity or low conductivity.

to H equaling zero. An IDE with a height of zero represents an IDE that is embedded in and flush with an insulating plane. The characteristic dimension for $H = 0$ was determined to be 5 μm for an IDE with 5 μm digit width and spacing and 10 μm for an IDE with 10 μm digit width and spacing. The characteristic dimension of a flat IDE is represented by δ_0. The effective characteristic dimension is represented by δ. The analysis presented in Figure 9-15 was performed with IDEs with 5 μm digit width and spacing and 10 μm digit width and spacing and is presented in Figure 9-15. The superposition of the scaled characteristic dimension of the both electrode configurations indicated that the deviation from the flat electrode (H=0 μm) produced an effective characteristic dimension that was 3.5 % smaller. The estimated height of the digits was observed in scanning transmission electron microscopy images by Shibata[118]. In the case of large values of H, the electrode digits form geometries similar to parallel plate electrodes where the characteristic dimension is the normal distance between the electrodes. This behavior
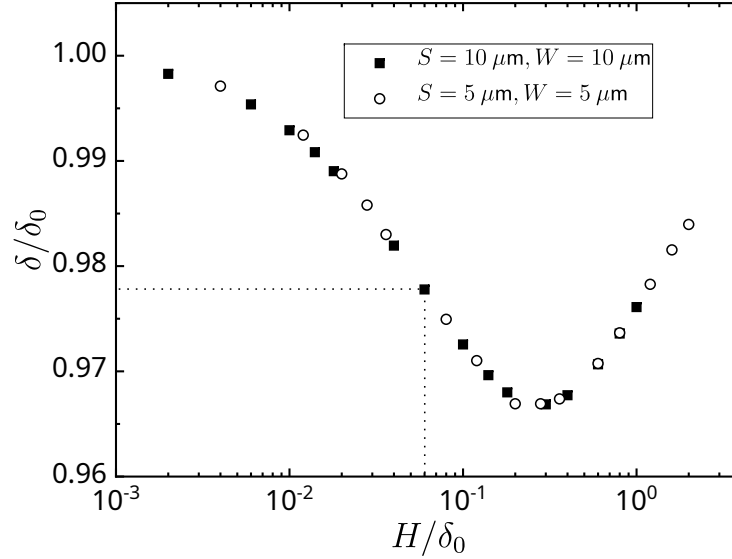
Figure 9-15. Scaled characteristic dimension as function of scaled electrode height. The superposition of the scaled characteristic dimension of the both electrode configurations indicated that the deviation from the flat electrode (H=0 μm) produced an effective characteristic dimension that was 3.5 % smaller. The dotted lines correspond to IDEs that are 120 nm in height which was observed in images published by Shibata[118].

is observed in the simulation at large H where the effective characteristic dimension approached δ_0.

9.4.2 Effect of Digit Width

The influence of electrode digit width on impedance response for a flat IDE was simulated to determine the characteristic dimension. The simulations were conducted for a 0.5 mM KCl aqueous solution, and the electrode width W was varied from 50 nm to 9.95 μm. The sun of the electrode width W and gap S was held constant at 10 μm. As a result, the electrode spacing was given by

$$S = 10\mu\text{m} - W \tag{9-17}$$

The simulated frequency range was from 1 kHz to 100 MHz. The high frequencies simulated are outside the experimentally measurable range. These simulations were performed to display fully the geometric capacitance since the characteristic frequency of

106
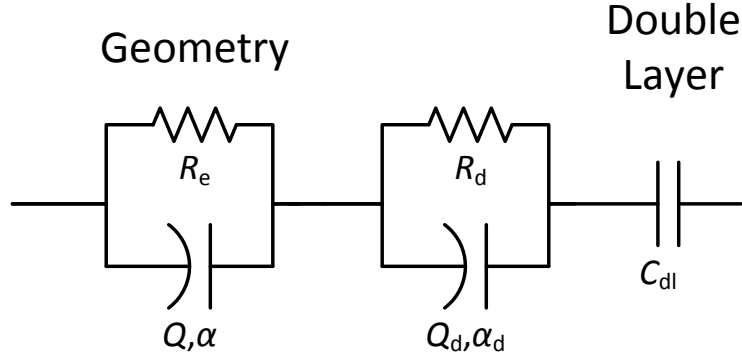
Figure 9-16. Circuit diagram for the fitting of geometric capacitance and blocking electrode behavior. The first RCPE corresponds to the geometric capacitance. The second RCPE is a bridging element used to join geometric capacitance with the double layer effects. The last capacitor represents the effects of the double layer.

a 0.5 mM KCl solution is 1.73 MHz. Parameters were extracted from the simulated data using an impedance model given by

$$Z = \frac{R_e}{1 + (j\omega)^\alpha R_e Q} + \frac{R_d}{1 + (j\omega)^{\alpha_d} R_d Q_d} + \frac{1}{j\omega C_{dl}} \tag{9-18}$$

represented as a circuit in Figure 9-16. The first RCPE in Figure 9-16 corresponds to the geometric capacitance. The second RCPE is a bridging element used to join geometric capacitance with the double layer effects. The last capacitor represents the effects of the double layer. The effective geometric capacitance can be calculated using the formula

$$C = Q^{1/\alpha} R_e^{(1-\alpha)/\alpha} \tag{9-19}$$

developed by Brug et al.[130].

Impedance responses are shown in Figure 9-17 for electrode widths of 50 nm, 5 μm, and 9.95 μm. The characteristic dimension decreased as the space between the electrodes decreased, and the simulated ohmic resistance was decreased as shown in Figure 9-18. The linear relationship at small electrode widths suggests that the characteristic dimension scales with the distance between the working and counter electrodes. At large electrode widths, the characteristic dimension approaches a small value which is indicative of the
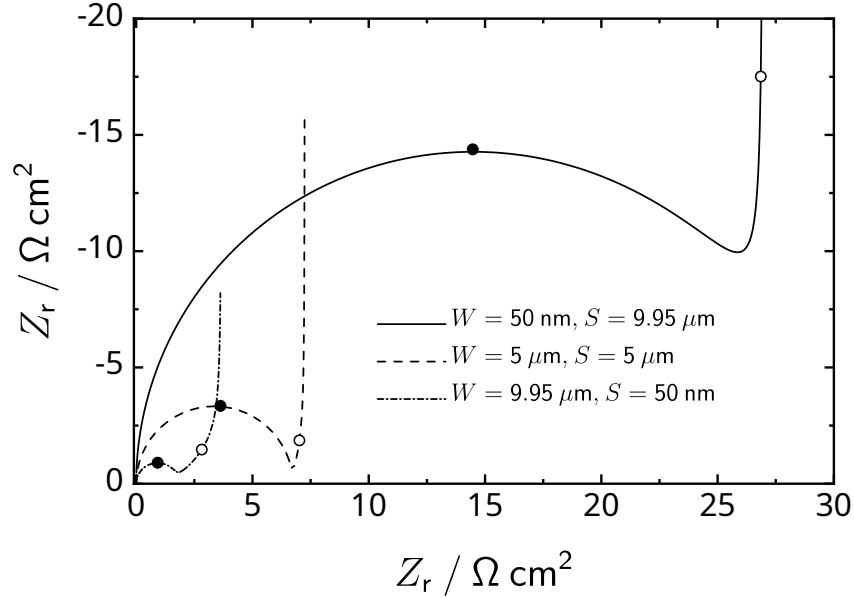
Figure 9-17. Nyquist plot of simulated impedance responses of aqueous KCl solutions using interdigitated electrodes with the electrode width as a parameter.

diminutive distance between the working and counter electrodes. When the impedance responses were scaled by the calculated resistivity and characteristic dimension, all the data superposed as shown in Figure 9-19.

9.5 Electrical Double Layer

When an electrolyte is in contact with charged surfaces, the concentrations of solvated ions are redistributed near the surface of the electrode such that the net charge of the interface is equal to zero. Near the surface, a diffuse region of charge exists that balances the charge held at the surface. The phenomenon described is called the electrical double layer. Beyond the diffuse region of charge, concentration gradients can exist in the absence of charge separation in a layer referred to as the diffusion layer. When IDEs are used in dilute electrolytes, the diffuse region of charge and diffusion layer can produce regions of higher ion concentration and can change the effective conductivity of the solution adjacent to the electrode.
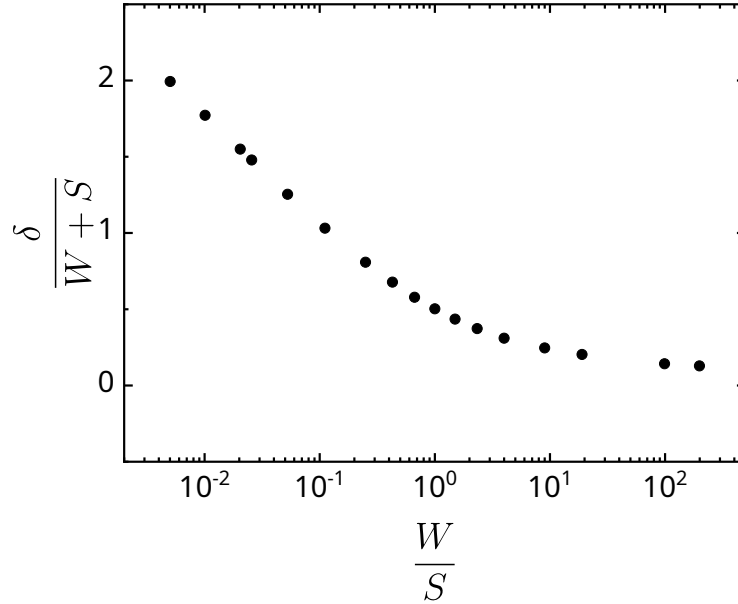
Figure 9-18. Scaled characteristic dimension as a function of the fraction of electrode surface. The linear relationship at small electrode widths suggested that the characteristic dimension scaled with the electrode width. At large electrode widths, the characteristic dimension approaches zero which is indicative of the diminutive distance between the working and counter electrodes.
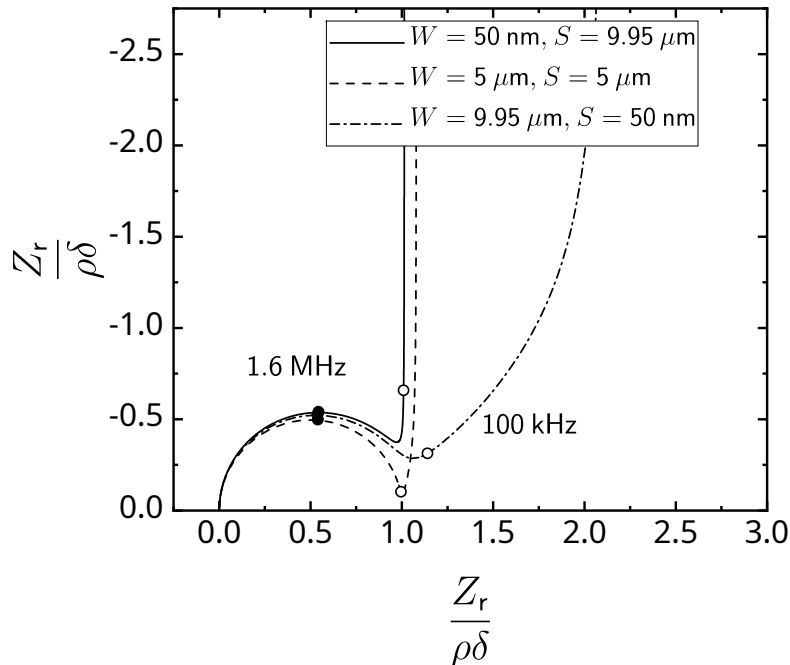
Figure 9-19. Nyquist plot of dimensionless scaled impedance of interdigitated electrodes with fraction of electrode surface as a parameter. The superposition of the high-frequency geometric features suggests that the characteristic dimension is correct.

The concentration distribution within the diffuse part of the double layer was obtained by solving Poisson's equation

$$\nabla^2 \Phi = -\frac{\rho_e}{\epsilon_r \epsilon_0} \tag{9-20}$$

where ρ_e is the charge density given by

$$\rho_e = F \sum_i z_i c_i \tag{9-21}$$

The boundary condition for the glass substrate and electrode were

$$\Phi(y = 0) = \zeta \tag{9-22}$$

where ζ the zeta potential of the surface. The boundary condition far from the electrodes at the top of the domain was

$$\Phi(y = H_{\text{dom}}) = 0 \tag{9-23}$$

The left and right boundary conditions were that the surfaces bear no charge.

The ionic species in solution adhered to the flux equation

$$\nabla \cdot \mathbf{N}_i = 0 \tag{9-24}$$

where

$$\mathbf{N}_i = -D_i \nabla c_i - z_i u_i F c_i \nabla \Phi \tag{9-25}$$

The left, right, and bottom boundary conditions were that the flux is zero due to symmetry. The boundary condition for concentration at the top boundary was

$$c_i (y = H_{\text{dom}}) = c_{i\infty} \tag{9-26}$$

The local conductivity was given by

$$\kappa = F^2 \sum_i z_i^2 u_i c_i \tag{9-27}$$

where z_i is the charge number of species i and u_i is the ionic mobility of species i.
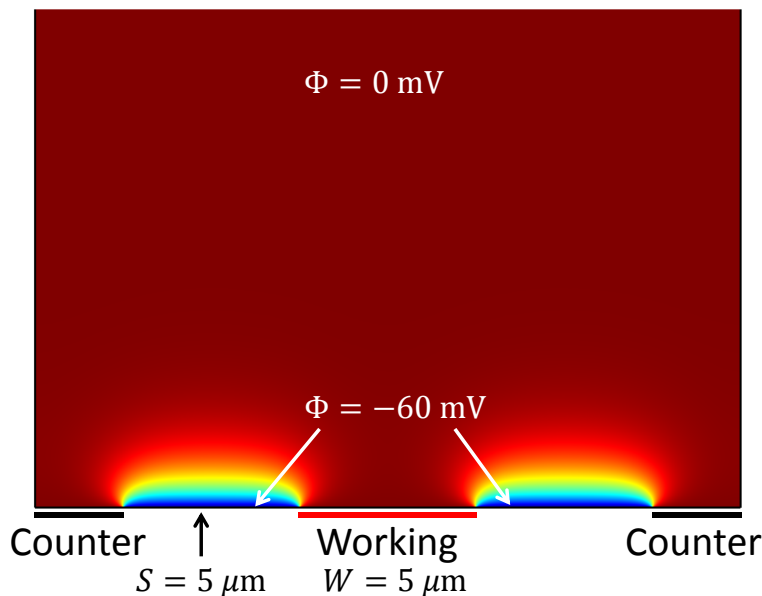
Figure 9-20. Potential distribution of an IDE due to the surface potential of -60 mV of the glass substrate.

For the IDE, the electrode and glass substrate were assumed to be charged when in contact with an electrolyte. The plane of closest approach for the counter ions in solution is called the outer Helmholtz plane and was assumed to have a zeta potential of -60 mV. Simulations with deionized water were performed to quantify the concentration profile near the electrode surface as a result of a -60 mV surface potential on the glass substrate separating the electrodes. The bulk concentration of hydronium and hydroxide was 1×10^{-7} M. The diffusion coefficients at 25°C of H^+ and OH^- have published values of 9.312×10^{-5} cm^2/s and 5.260×10^{-5} cm^2/s respectively.[82] The ionic mobility u_i for species i was estimated using the Nernst-Einstein equation

$$D_i = RTu_i \tag{9-28}$$

The potential distribution is shown in Figure 9-20. The corresponding cation and anion concentration profiles are shown in Figures 9-21 and 9-22. From the concentration distribution calculated from Figures 9-21 and 9-22, the conductivity distribution that was calculated using equation (9-27) is presented in Figure 9-23. The concentration and
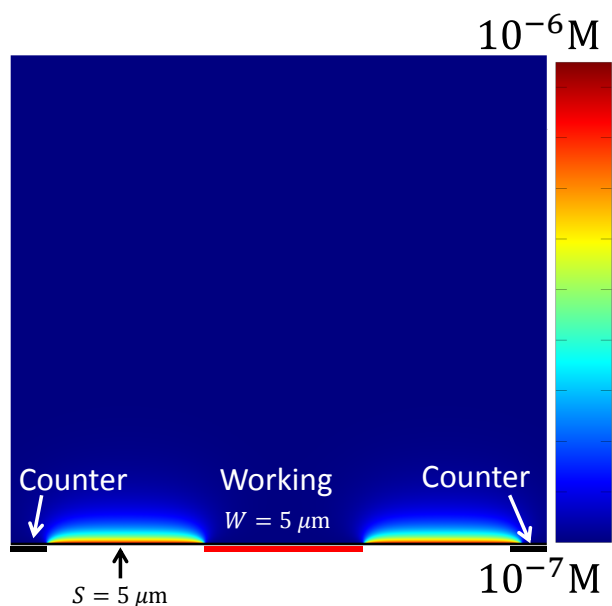
Figure 9-21. Cation concentration distribution due to the substrate surface potential. Due to the negative surface potential, there is a higher cation concentration near the surface of the glass substrate.
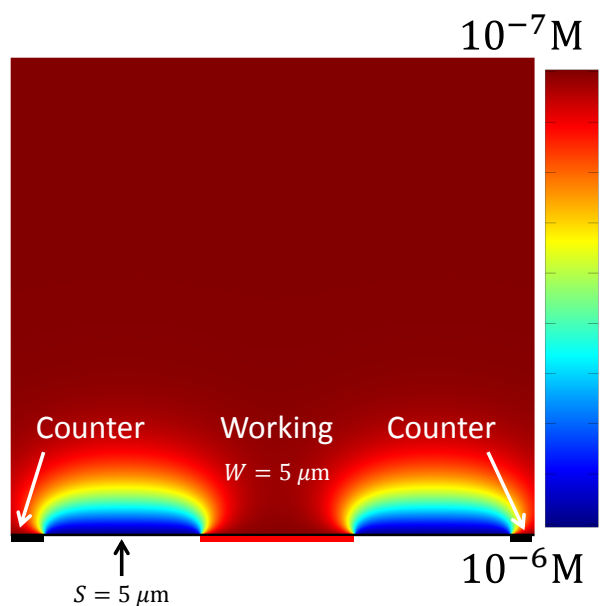
Figure 9-22. Anion concentration distribution due to the substrate surface potential. The diffuse region of charge is observed in the distribution around the glass substrate.

3.5×10^{-7} S/cm

Counter   Working   Counter

$W = 5\ \mu$m

$S = 5\ \mu$m

1.0×10^{-8} S/cm
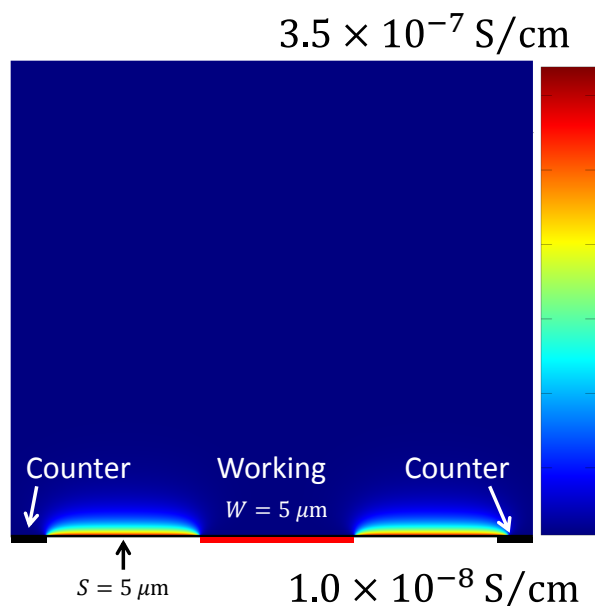
Figure 9-23. Conductivity distribution due to the substrate surface potential causing local deviation from the bulk cationic and anionic concentrations.

$2.5\ \mu$m $5\ \mu$m $2.5\ \mu$m
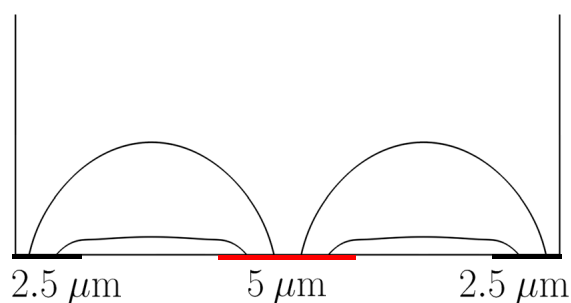
Figure 9-24. Current lines of an IDE with a surface potential on the glass substrate. The compression of the current distribution closer to the glass substrate surface is due to the increased conductivity near the surface. The bold red line is the working electrode and the bold black line is the counter electrode.

conductivity distributions affected the current distribution in the electrolyte as shown in Figure 9-24 in comparison to the current distribution in the absence of concentration gradients as shown in Figure 9-25.

9.5.1   Aqueous Potassium Chloride Solutions

The impedance response of aqueous solutions of various KCl concentrations was simulated taking account of an electrical double layer. The concentration distribution was used to calculate the local conductivity for the EIS simulations. The modulation
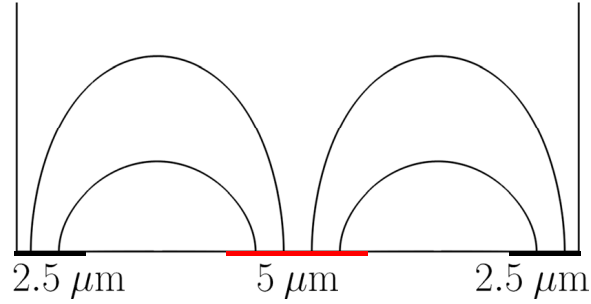
Figure 9-25. Current lines of an IDE without a surface potential on the glass substrate. The current lines are longer and extend further into the medium. The bold red line is the working electrode and the bold black line is the counter electrode.

of concentration for the current analysis was not considered in the calculation of the impedance. Simulations were performed using bulk KCl concentrations of 10 mM, 5 mM, 1 mM, 500 μM, and 100 μM. The diffusion coefficients at 25°C of K$^+$ and Cl$^-$ have published values of $1.957{\times}10^{-5}$ cm^2/s and $2.032{\times}10^{-5}$ cm^2/s respectively.[82] The ionic mobility u_i for species i was estimated using the Nernst-Einstein equation. The surface zeta potential of the electrode and glass substrate surfaces were assumed to be -60 mV. A double-layer capacitance was assumed to be $2{\times}10^{-5}$ F/cm^2. The dielectric constant for the solution was assumed to 78. The bulk concentration selected for study exhibited a large range of resistivity that spanned from 6.67 Ωcm to 66.7 kΩcm. Simulations were performed with a flat electrode geometry with a digit width and spacing of 5 μm. The simulation frequency range was from 10 mHz to 100 kHz. The frequencies were represented in terms of a dimensionless frequency K given by

$$K = 2\pi\rho\epsilon_{\mathrm{r}}\epsilon_0 f \tag{9-29}$$

which allowed for characteristic frequencies of all solutions to be unity. The impedance was scaled by the product of the bulk resistivity and the characteristic dimension.

The simulation of aqueous KCl solutions showed that the characteristic frequency of the geometric capacitance of any of the simulated concentration were not in the simulated frequency range as shown in Figure 9-26. As the bulk concentration of KCl decreased,
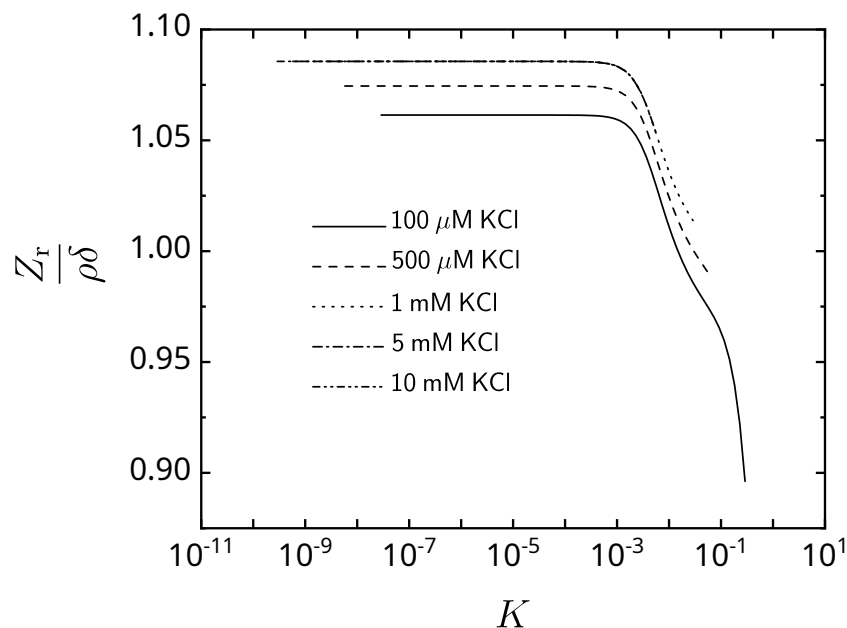
Figure 9-26. Dimensionless real impedance as function of dimensionless frequency where the concentration of the aqueous solution was a parameter. The shifting downward of the curved was due to the impedance reduction resulting from the electrical double layer. None of the simulated concentrations reached a dimensionless frequency of unity which suggests that the characteristic frequencies for the geometric capacitance of IDEs was outside the simulated frequency range.

the dimensionless impedance decreased. The increase in the effective conductivity is suggested in the scaled Nyquist plot in Figure 9-27. As the concentration is reduced, there is greater concentration of ions near the electrodes in comparison to the bulk solution. The effective resistivity of the 100 μM KCl solution was extracted by nonlinear regression with an impedance model given in equation (9-18). The values for the R_e, Q, and α were 32.5±0.020 Ωcm^2, 1.93±0.054×10^{-8} s$^\alpha$/Ωcm^2, and 0.977±0.0020, respectively. The resistivity of the bulk solution was 66.7 kΩcm and the regressed value from the impedance was 65.06±0.039k Ωcm. The reduction of the resistivity is due to higher conductivity near the electrodes. The dielectric constant used for the simulation was 78; whereas, the value obtained by regression was 77.4±3.3. The agreement of the input relative dielectric

115
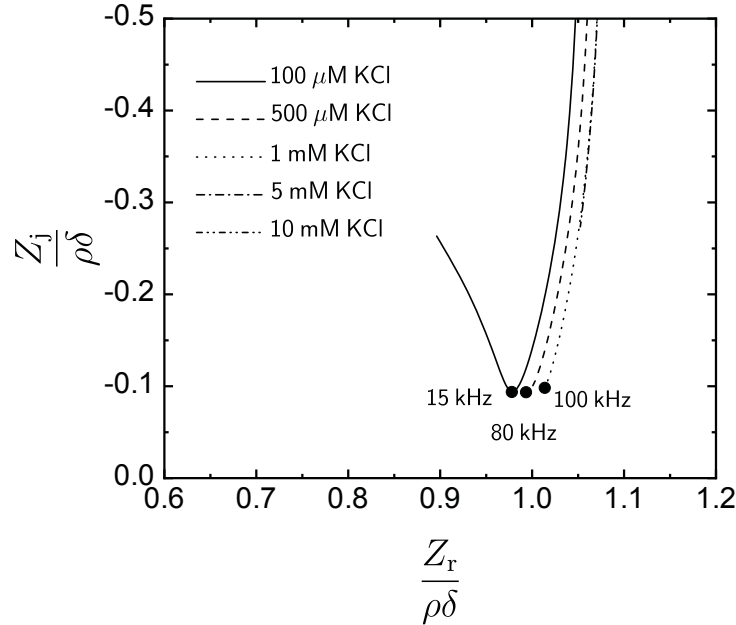
Figure 9-27. Dimensionless Nyquist plot of simulated impedance responses for aqueous KCl solutions. The geometric RC loop was only visible for the 100 μM KCl solution at a frequency of 15 kHz. The 1 μM KCl solution just reached the RC loop representing the geometric capacitance. The geometric capacitance for concentrated solutions were not visible.

constant and extracted relative dielectric constant suggest that the proper characteristic dimension was 5 μm.

9.5.2 Deionized Water

Deionized water was modeled as a low-conductivity medium for performing EIS measurements using IDE. The bulk concentration of H^+ and OH^- were both assumed to be 1×10^{-7} M. The diffusion coefficients at 25°C of H^+ and OH^- have published values of 9.312×10^{-5} cm^2/s and 5.260×10^{-5} cm^2/s, respectively.[82] The ionic mobilities were estimated using the Nernst-Einstein equation. The surface zeta potential of the electrode surfaces and glass substrate were assumed to be -60 mV. A double-layer capacitance was assumed to be 2×10^{-5} F/cm^2. The dielectric constant for the solution was assumed to 78. The bulk liquid resistivity was 17.5 MΩcm. The simulation frequencies ranged from 10 mHz to 100 kHz. The simulation results are shown in Figure 9-28. The ohmic
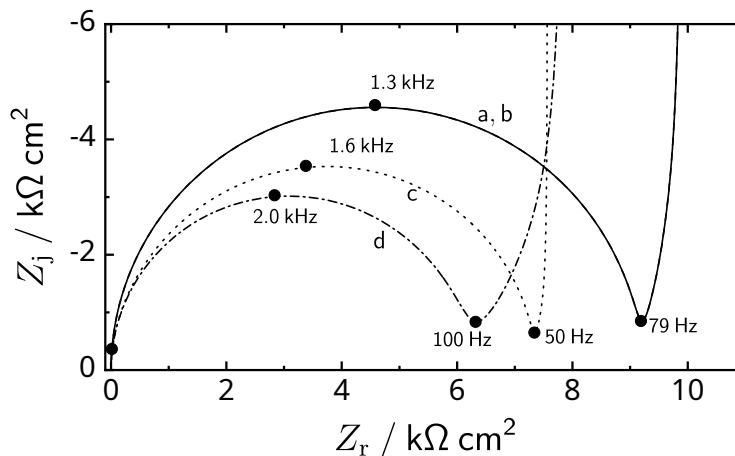
Figure 9-28. Nyquist plot of simulated impedance responses for deionized water on a flat IDE with width and spacing of 5 μm. (a) no surface zeta potential (b) surface zeta potential of -60 mV on the glass substrate (c) surface zeta potential of -60 mV on the electrodes (d) surface zeta potential of -60 mV on the glass substrate and electrodes.

Table 9-1. Ohmic resistance fit from the simulated data in Figure 9-28.

Label	Glass	Electrode	R_e	ρ
a	0 mV	0 mV	9.13 kΩcm^2	18.4 MΩcm
b	-60 mV	0 mV	7.87 kΩcm^2	15.7 MΩcm
c	0 mV	-60 mV	7.33 kΩcm^2	14.7 MΩcm
d	-60 mV	-60 mV	6.30 kΩcm^2	12.6 MΩcm

resistance extracted by nonlinear regression is presented in Table 9-1. For deionized water, the surface zeta potential of -60 mV resulted in a reduction of 31 % in ohmic resistance.

9.6 Interdigitated Electrode for High Conductivity Applications

The measurement of resistivity of electrolytes with concentrations greater than 0.5 mM is difficult because the loop associated with the geometric capacitance occurs at frequencies higher than the reliable measurement range, i.e., greater than 100 kHz. A proposed solution is the addition of a resistive film to surface of the electrode. Zinc oxide is a viable candidate since atomic layer deposition of films as small as 1 nm is possible.[131] The resistivity and dielectric constant of ZnO was estimated to be 100 MΩcm and 10 respectively.[132, 133] The characteristic frequency of ZnO is 1.8 kHz

117
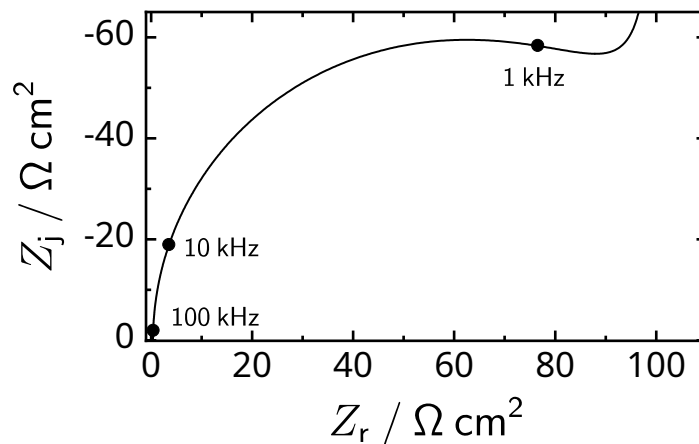
Figure 9-29. Nyquist plot of simulated impedance response of a interdigitated electrode with a 5 nm ZnO film on the electrode surface.

and within reliable experimental frequency ranges. A 5 nm film of ZnO was simulated on an IDE with an digit width and spacing of 5 μm. The electrolyte was an aqueous 10 mM KCl solution. The characteristic frequency of geometric capacitance for 10 mM KCl is 35 MHz. The simulated data is shown in Figure 9-29. Magnification of the high-frequency behavior is shown in Figure 9-30. The extracted characteristic dimension of the ZnO film was 10 nm which was in agreement with a 5 nm ZnO film on both the electrodes. EIS measurements using the ZnO-coated IDE can have the ohmic resistance regressed by using a measurement model analysis.

118
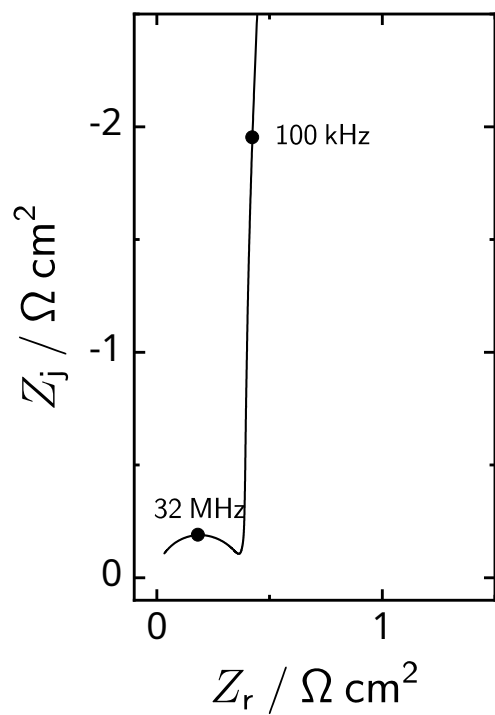
Figure 9-30. Magnified Nyquist plot of a simulated impedance response of a interdigitated electrode with a 5 nm ZnO film on the electrode surface.

CHAPTER 10

IMPEDANCE MEASUREMENTS USING INTERDIGITATED ELECTRODES

The simulations results presented in Chapter 9 were verified experimentally for organic liquids, aqueous KCl, and deionized water. EIS data obtained from experiments were compared to simulation. EIS measurements were performed using a Gamry Reference Potentiostat 3000. The software used to interface with the Gamry Reference 3000 was Gamry Instruments Framework version 6.33.

10.1 Experimental Method

The IDE used for all experiments was the DropSens IDEAU5 which is a gold electrode on a glass substrate. The digit dimensions are 5 μm in width and spacing. The length of each digit is 6760 μm. The electrodes were used with a DropSens screen-printed electrode holder (DRP-CAST) that was inserted into a hollowed rubber stopper. Each liquid used a dedicated IDE to prevent cross contamination. The working and working sense connectors from the Gamry Reference 3000 were connected to the working electrode of the IDE. The counter and reference connectors from the Gamry Reference 3000 were connected to the counter electrode. The cell was placed inside a copper screen Faraday cage. The ground connector from the Gamry Reference 3000 was connected to the Faraday cage and to a metal ground.

10.1.1 Organic Liquids

Organic liquid samples of synthetic motor oil, glycerol, and ethylene glycol were put into a 20 mL vial. The mouth of the vial was sufficiently large to allow direct insertion of the IDE into the liquid. The electrode holder and vial were secured using clamps and ring stand. The entire experimental setup shown in Figure 10-1 was placed in a Faraday cage to mitigate electrical interference from outside sources such as fluorescent lights.

10.1.2 Aqueous Solutions

The EIS measurements of aqueous solutions were performed in a jacketed Dr. Bob's Cell™. A Dr. Bob's Cell™ is a glass reservoir obtained from Gamry with a working volume
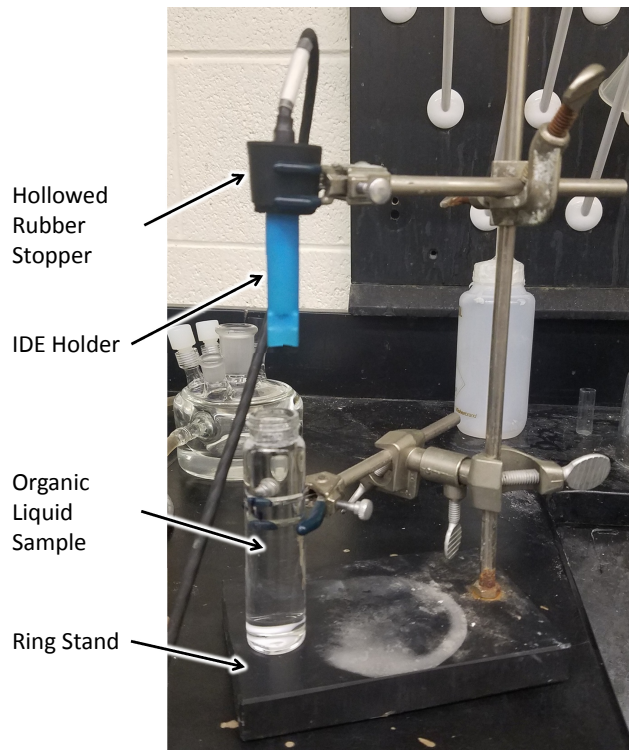
Figure 10-1. Photograph of the experimental setup used for organic liquids. Photograph is courtesy of the author.

of 200 mL with five ports for the insertion of electrodes and is shown in the experimental

setup in Figures 10-2 and 10-3. The temperature of all experiments was maintained

at $25\pm0.1^\circ$C using a Fisher Scientific Isotemp Refrigerated Circulator Model 910. The

rubber stopper and holder were inserted into the large opening of the jacketed cell. The

entire experimental setup shown in Figure 10-2 was placed in a Faraday cage to mitigate

electrical interference.

10.1.3 Deionized Water

In experiments with deionized water, the solubility of atmospheric carbon dioxide

and oxygen were a concern for experimental accuracy. The conductivity can shift from

carbon dioxide forming carbonic acid in deionized water. Oxygen reduction can occur

during measurement. The effect of atmospheric carbon dioxide and oxygen was mitigated

by bubbling nitrogen (AirGas Ni BIP300) into the water at a pressure of 5 psig using an

Ace Glass Inc. gas dispersion tube (9435-35). The ports of the jacketed cell were sealed
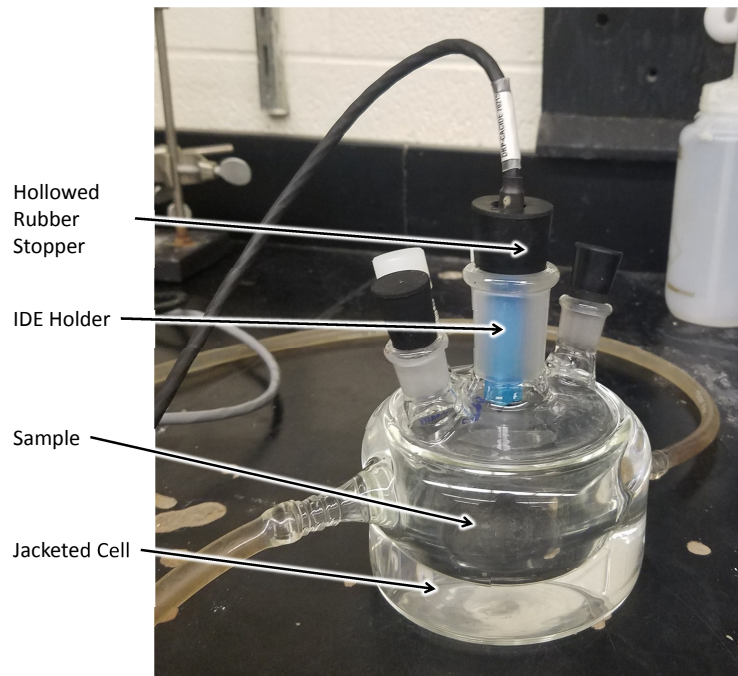
Figure 10-2. Photograph of the experimental setup used for aqueous solutions.
Photograph is courtesy of the author.

with Parafilm M®. Nitrogen was bubbled for at least 1 hour prior to any measurements.
Immediately before EIS measurements, the gas dispersion tube was pulled out of the
deionized water to a height just above the water level and nitrogen pressure was increased
to 20 psig. The positive-pressure headspace reduced diffusion of atmospheric carbon
dioxide and oxygen into the cell. After the EIS measurement was completed, the gas
pressure was reduced to 5 psig and the gas dispersion tube was re-inserted into the water.
The gas was allowed to bubble for at least 10 minutes prior to the next measurement. The
deionized water was obtained using a Barnstead e-Pure, reverse-osmosis water-purification
system. The Barnstead unit has an inline resistivity meter. Deionized water was only used
when the resistivity measured 17.4-17.5 MΩcm.

10.1.4 Rotating Disk Electrode

EIS measurements were made using a rotating disk electrode to validate data
collected with the IDE. The AutoLab RDE2 rotating disk electrode was operated at
1000 rpm using a 1.5 mm radius platinum tipped disk electrode (6.1204.310). The
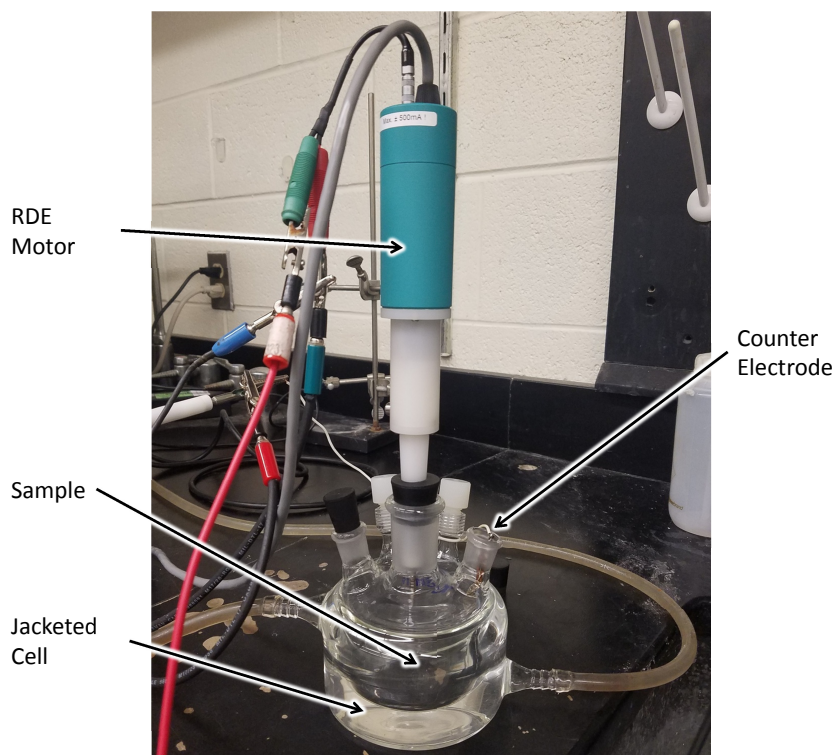
Figure 10-3. Photograph of the experimental setup used for aqueous solutions with a rotating disk electrode. Photograph is courtesy of the author.

AutoLab RDE2 has two connectors, one for the disk electrode and one for ground. The working and working sense connectors from the Gamry Reference 3000 were connected to the rotating disk electrode lead. A counterelectrode was a platinum foil with a surface area 5.71 cm^2. The counterelectrode was placed in the water in the cell and connected to the counter lead of the potentiostat. The ground connector from the Gamry Reference 3000 was connected to the AutoLab RDE2, the Faraday cage, and to steel plumbing which served as a ground. The experimental setup shown in Figure 10-3 was placed in a Faraday cage.

10.1.5   Experimental Data Analysis

A measurement model analysis of the experimental data was performed to confirm consistency with the Kramers–Kronig relations. Data found to be inconsistent with the Kramers–Kronig relations were discarded from subsequent analyses. Regression of experimental data was performed using OriginLabs Origin 2018 using circuit models that
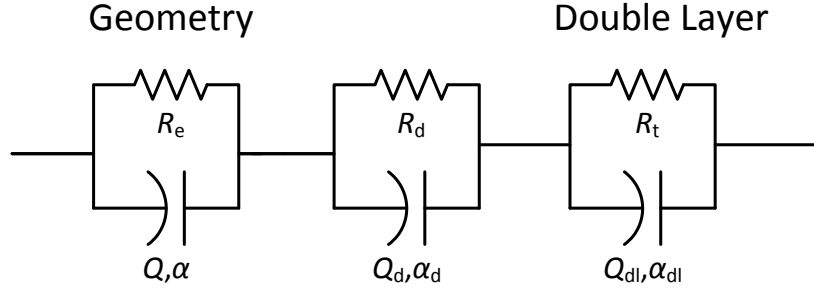
Figure 10-4. Circuit diagram for the fitting of geometric effects and low-frequency behavior. The first RCPE corresponds to the geometric effects. The second RCPE is a bridging element used to join geometric effect with the low-frequency behavior. The last RCPE represents the non-stationary low-frequency behavior.

were consistent with the data collected and the estimated characteristic frequencies of the geometric effects. The circuit model used for parameter extraction with experimental data is shown in Figure 10-4 and is given in equation (10-1). The first RCPE in the model is attributed to geometric capacitance. The third RCPE is attributed to low-frequency double layer capacitance and a faradaic reaction. The charge-transfer resistance of the faradaic reaction is represented by R_t and a double layer capacitance assumed to be affected by frequency dispersion represented by Q_dl and α_dl. The second RCPE serves a bridge to join the low-frequency and high-frequency behaviors.

$$Z = \frac{R_\text{e}}{1 + (\mathrm{j}\omega)^{\alpha} R_\text{e} Q} + \frac{R_\text{d}}{1 + (\mathrm{j}\omega)^{\alpha_\text{d}} R_\text{d} Q_\text{d}} + \frac{R_\text{t}}{1 + (\mathrm{j}\omega)^{\alpha_\text{dl}} R_\text{t} Q_\text{dl}} \qquad (10\text{-}1)$$

10.2   Experimental Results

Measurement of impedance response was performed. The data was analyzed using the measurement model to determine consistency with the Kramers–Kronig relations. Data that was consistent with Kramer-Kronig relations was regressed to the process model shown in Figure 10-4.
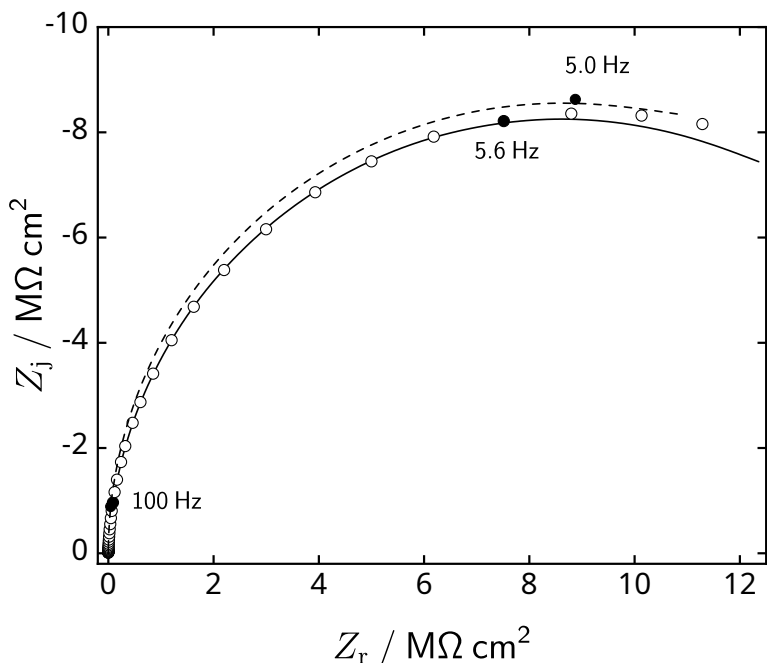
Figure 10-5. Nyquist plot of experimental and simulated impedance of Mobil 1 motor oil. The solid line and open circles are experimental data from motor oil. The dashed line is simulated data.

10.2.1 Organic Liquids

Organic liquids were measured using the DropSens IDEAU5 electrodes. The impedance response of Mobil 1 5W-30 oil was measured using a perturbation amplitude of 1 V. The measurement was found to be linear at a perturbation amplitude of 1 V by monitoring the Lissajous plot. The typical conductivity for oil is on the order of 2 nS/m. The typical dielectric constant of oil is 4. The addition of proprietary commercial additives may cause deviation from the typical values. The data collected from the oil sample is presented in Nyquist form in Figure 10-5. The characteristic frequency for oil using typical values for resistivity and dielectric constant is 5 Hz. The characteristic frequency of the oil sample was measured to be 5.6 Hz. The conductivity was determined to be 2.9 ± 0.026 nS/m and the capacitance was found to be 1.93 ± 0.016 nF/cm^2. Due to the additives, the electrical properties of motor may vary. The expected conductivity is greater than 2 nS/m. The experimental dielectric constant was 10.95 ± 0.093 which larger than

typical values for motor oil which was expected to be approximately 4.[134] The deviation of the dielectric constant from the typical values for oil was attributed to the dielectric response of the glass substrate. The electrical path through the glass is in parallel to the electrical path through the solution, therefore the capacitances are additive, given by

$$C_{\text{eff}} = C_{\text{solution}} + C_{\text{glass}} \tag{10-2}$$

The substrate domain can be represented as a flat IDE. The thickness of the glass substrate of the DropSens IDEAU5 was 0.7 mm which is larger than the simulated domain. Therefore these characteristic dimension of the glass substrate is δ_0. Since the effect of digit height on the characteristic dimension was small, the characteristic dimension in the glass was assumed to be the same as in the solution resulting in the simplification

$$\epsilon_{\text{r,eff}} = \epsilon_{\text{r,solution}} + \epsilon_{\text{r,glass}} \tag{10-3}$$

A typical value of relative dielectric constant for glass is 3.75-9.5.[135] A median value for glass was assumed to be 6.3.[135] Therefore, the dielectric constant of oil is 4.4 which is within the typical range for oil.

The influence of the substrate on conductivity was evaluated in a similar to fashion to the capacitance and yielded

$$\kappa_{\text{eff}} = \kappa_{\text{solution}} + \kappa_{\text{glass}} \tag{10-4}$$

Since the conductivity of glass, on the order of 10^{-10} S/m, was small compared to the conductivity of the liquids, the adjusted conductivities were largely unchanged.

The impedance for glycerol (Sigma G5516) was measured using a perturbation of 200 mV. A linear response was observed during the measurement by monitoring the Lissajous plot. The typical values of conductivity and dielectric constant for glycerol are 0.1 mS/m and 42.5, respectively. The characteristic frequency for glycerol is on the order of 4.2 MHz which is higher than the measured range; therefore, the high-frequency limit for the real part of the impedance was used as the ohmic resistance, which was obtained
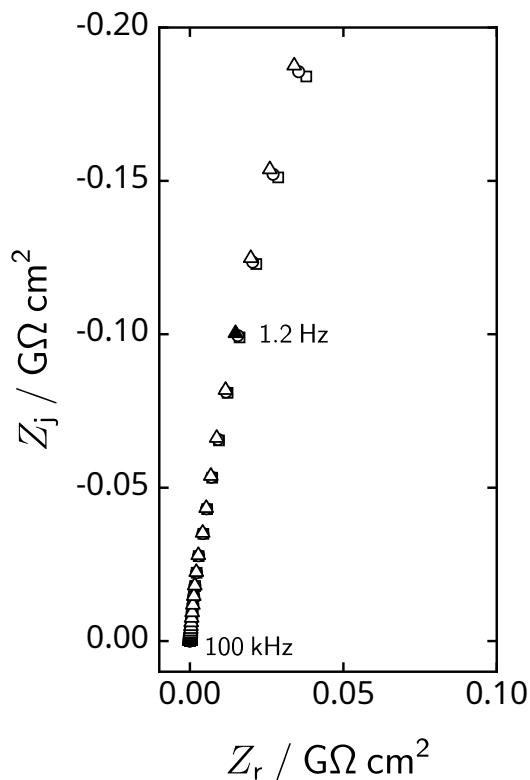
Figure 10-6. Nyquist plot of experimental impedance response of glycerol.

using a measurement model analysis. The measurements are shown in Figure 10-6. The average high-frequency limit was 87 Ωcm^2 which corresponds to an estimated conductivity of 0.57 mS/m. The measured value is close to typical values.[136, 137]

The impedance response for ethylene glycol (Sigma-Aldrich 293237) was measured using a 200 mV perturbation. Linearity was confirmed by monitoring the Lissajous plot during measurement. The typical values of conductivity and dielectric constant for glycerol are 107 μS/m and 37, respectively. The characteristic frequency for glycerol is on the order of 42.3 kHz, which is within the measured range. The results are shown in Figure 10-7. The conductivity and dielectric constant were 51.5$\pm$0.05 μS/m and 58$\pm$3.3, respectively. The dielectric constant of ethylene glycol without the influence of the glass substrate was 51.4, which is larger than the typical value for ethylene glycol.

The resistivity and substrate-adjusted dielectric constant for synthetic motor oil was in agreement with typical values for lubricating oils. The conductivity of glycerol was in

127
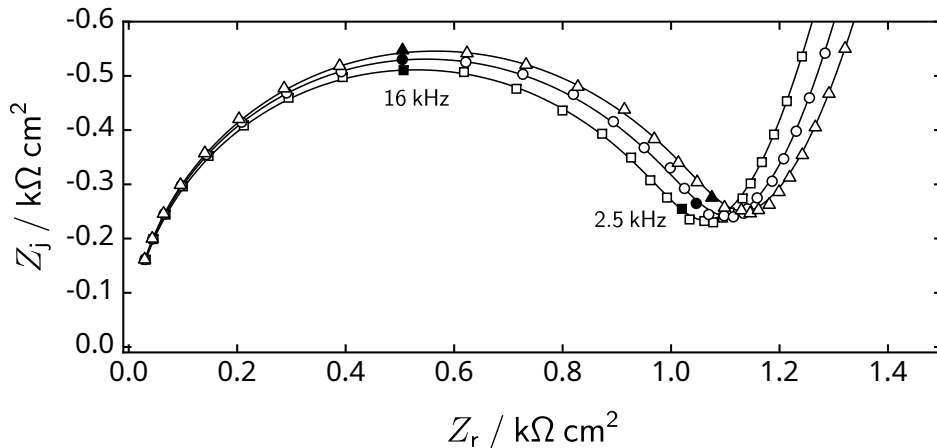
Figure 10-7. Nyquist plot of the experimental impedance response of ethylene glycol.

the range of published values. The conductivity of ethylene glycol was within the range of published values. The effective dielectric constants were larger than published values which was a result of the influence of the glass substrate. In the case of synthetic motor oil, the dielectric contribution of the substrate inflated the effective dielectric constant by 6.3. For ethylene glycol, the adjustment in dielectric constant due to the glass substrate did not yield a dielectric constant that was in agreement with published values. In order to obtain accurate measurements of the dielectric of the liquid medium, the dielectric properties of the glass must known.

10.2.2 Aqueous KCl

Aqueous solutions of KCl were prepared from KCl (Fisher Scientific P217-3) and deionized water in concentrations of 10 mM, 5 mM, 1 mM, and 0.5 mM. The prepared solutions had calculated conductivities of 1.50 mS/cm, 0.75 mS/cm, 0.15 mS/cm, and 75 μS/cm, respectively. Under the assumption that the dielectric constant of water was 78, the characteristic frequencies of the solutions respectively were 34.5 MHz, 3.45 MHz, and 1.73 MHz, which are all outside the measured frequency range. All samples were measured using a DropSens IDEAU5 interdigitated gold electrode with a perturbation amplitude of 10 mV. The amplitude of 10 mV resulted in a linear response which was confirmed by monitoring the Lissajous plot during measurement. The jacketed cell was
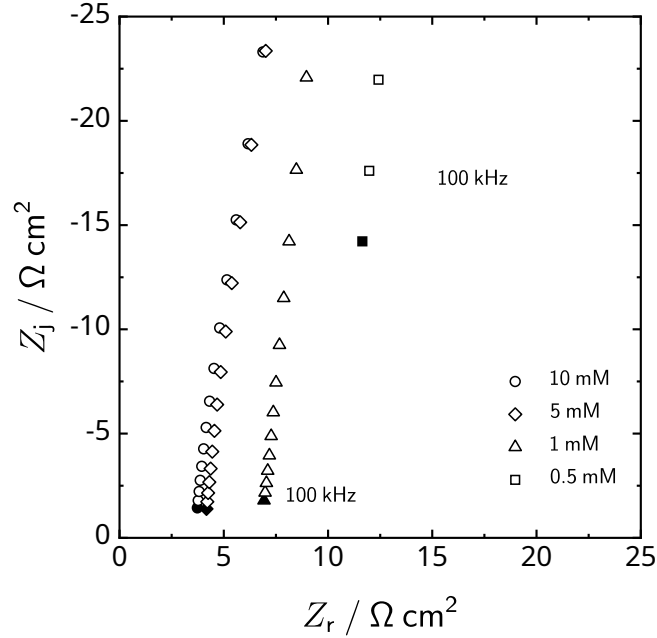
Figure 10-8. Nyquist plot of the experimental impedance of aqueous KCl at concentrations of 10 mM, 5 mM, 1 mM, and 0.5 mM.

rinsed thoroughly with deionized water. Samples were measured from lowest concentration to highest concentration in order to prevent cross contamination of residual dissolved salts. The measured data are shown in Figure 10-8.

The IDE cell constant K_{cell} can be obtained experimentally by the measurement of the ohmic resistances of solutions with known resistivities.[138]. The slope of the solution resistance in Ω as a function of the solution resistivity provides an estimate of the cell constant as

$$R_{e,eff} = \rho K_{cell} \tag{10-5}$$

The high-frequency limit is assumed to be the ohmic resistance. The ohmic resistance is plotted as a function of the known solution resistivity. The slope of the line is the cell constant. The ideal value of the cell is given by

$$K_{cell} = \frac{\delta}{A_{IDE}} \tag{10-6}$$

129
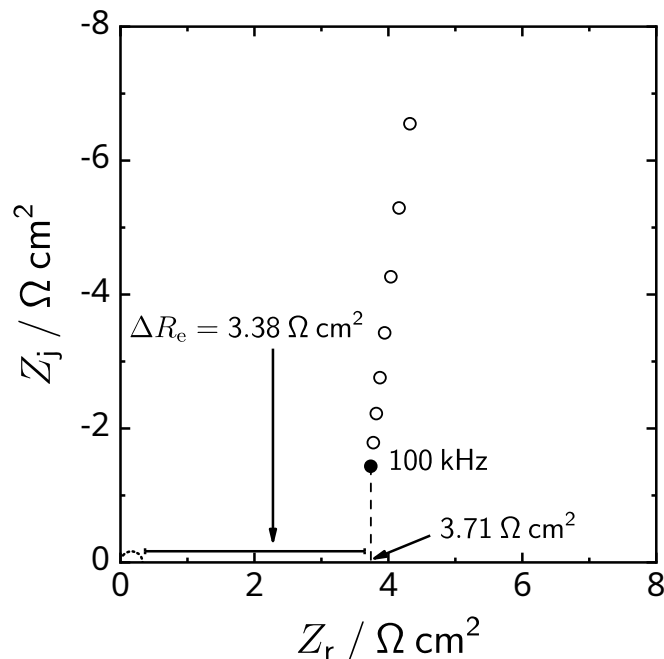
Figure 10-9. Nyquist plot of the impedance of 10 mM KCl at concentration. The dotted
semi-circle represents the predicted geometric effect of the impedance. The
vertical dashed line is the value of the real part of the impedance at 100 kHz.

which was shown in simulations and by Zaretsky et al.[96] to be 4.9 μm for a DropSens

IDEAU5 IDE.

In sufficiently high-conductivity solutions, the measured resistance was not close

to the actual ohmic resistance. Magnified views of Figure 10-8 are shown in Figures

10-9 to 10-12, which correspond to the solution concentrations of 10 mM, 5 mM,

1 mM, and 0.5 mM, respectively. The magnified plots display the disparity between

the high-frequency limit of the real part of the impedance and the predicted solution

ohmic resistance.   The effective resistance can be expressed in terms of the calculated

ohmic resistance and the difference between the calculated and measured high-frequency

real value of the impedance which is represented by ΔR_{e}.

$$R_{\mathrm{e,eff}} = R_{\mathrm{e}} + \Delta R_{\mathrm{e}} \qquad (10\text{-}7)$$
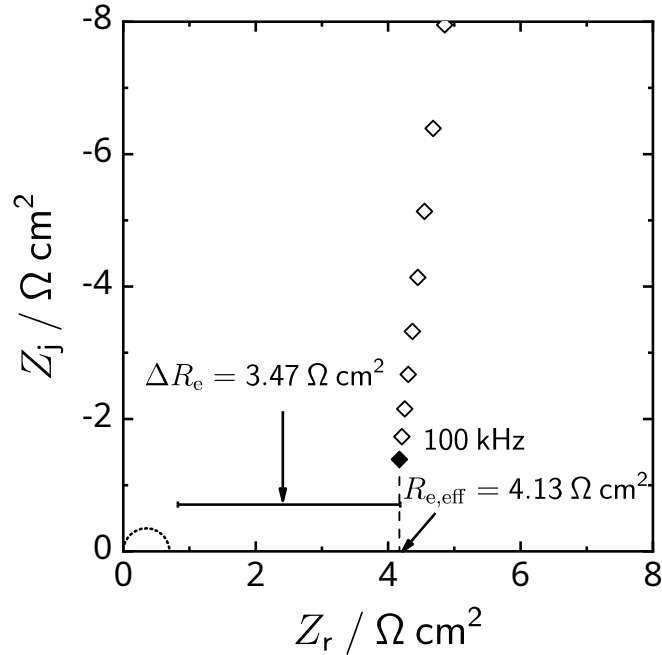
Figure 10-10. Nyquist plot of the impedance of 5 mM KCl at concentration. The dotted semi-circle represents the predicted geometric effect of the impedance. The vertical dashed line is the value of the real part of the impedance at 100 kHz.
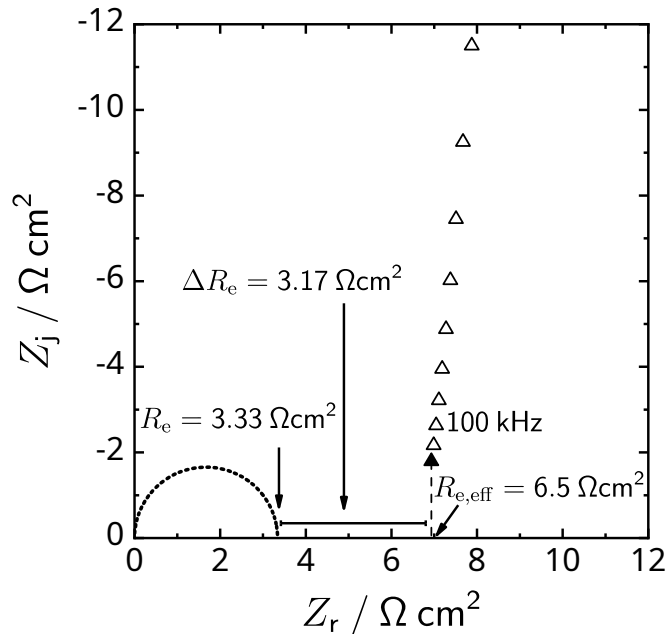
Figure 10-11. Nyquist plot of the impedance of 1 mM KCl at concentration. The dotted semi-circle represents the predicted geometric effect of the impedance. The vertical dashed line is the value of the real part of the impedance at 100 kHz.
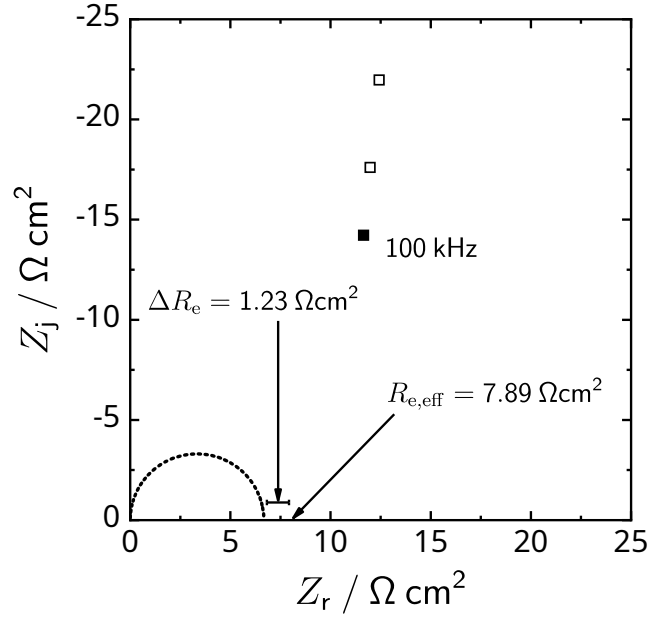
Figure 10-12. Nyquist plot of the impedance of 0.5 mM KCl at concentration. The dotted semi-circle represents the predicted geometric effect of the impedance. The vertical dashed line is the value of the real part of the impedance at 100 kHz.

According to De la Rica et al.[138], the slope of effective resistance as a function of resistivity assumes that

$$K_{\text{cell}} = \frac{\mathrm{d}R_{\text{e,eff}}}{\mathrm{d}\rho} \tag{10-8}$$

Substitution of equation (10-7) into equation (10-8) results in

$$\frac{\mathrm{d}R_{\text{e}}}{\mathrm{d}\rho} + \frac{\mathrm{d}\Delta R_{\text{e}}}{\mathrm{d}\rho} = K_{\text{cell}} \tag{10-9}$$

When ΔR_{e} is independent of ρ, equation (10-9) and equation (10-8) are equivalent. The experimental values of ρ, $R_{\text{e,eff}}$, and ΔR_{e} are shown in Table 10-1. The effective ohmic resistance error was obtained by regression using a measurement model. A linear regression of the effective resistance as a function of solution resistivity with a weighting of square inverse error was performed. The weighting strategy reduced the influence of high-error estimates for the effective ohmic resistance. The regressed effective ohmic resistance as a function solution resistivity is shown in Figure 10-13. The

Table 10-1. Effective ohmic resistance of KCl solutions.

KCl Conc. mM	Sample	ρ Ωcm	$R_{e,eff}$ Ωcm^2	ΔR_e Ωcm^2
10	1	0.667	3.69±0.006	3.36
10	2	0.667	3.75±0.014	3.42
10	3	0.667	3.69±0.007	3.36
5	1	1.33	4.16±0.025	3.49
5	2	1.33	4.12±0.008	3.45
5	3	1.33	4.12±0.007	3.45
1	1	6.67	6.53±0.041	3.20
1	2	6.67	6.50±0.047	3.17
1	3	6.67	6.49±0.044	3.16
0.5	1	13.3	7.73±0.718	1.06
0.5	2	13.3	7.95±0.591	1.28
0.5	3	13.3	7.99±0.511	1.32
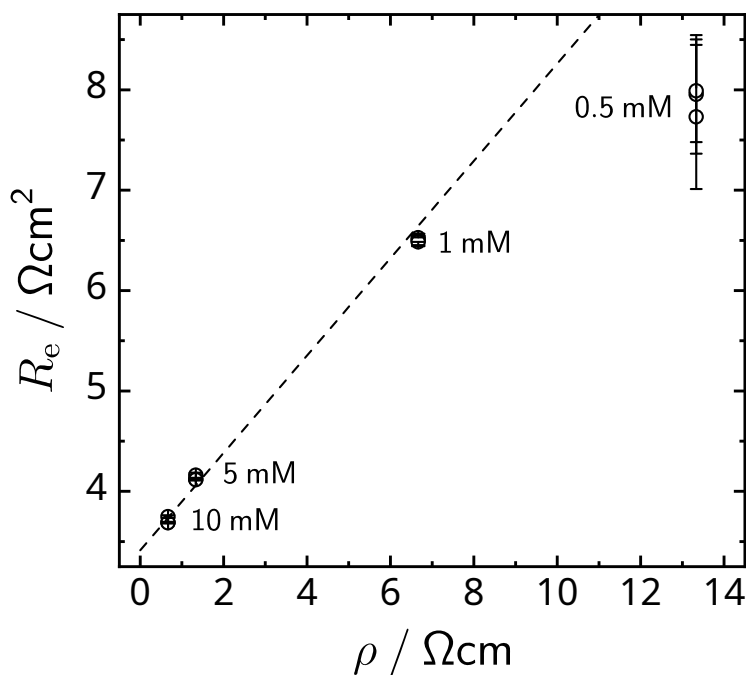
Figure 10-13. The effective resistance a function of the solution resistance. The dashed line represents a linear fit with a weighting of square inverse error. The slope of the line is 4.85±0.22 μm which close to the simulated characteristic dimension of 4.89 μm.

characteristic dimension for the DropSens IDEAU5 electrode was calculated from the data presented in Table 10-1 and found to be 4.85±0.22 μm using equation (10-8). The experimentally obtained characteristic dimension was in agreement to those obtained by simulation. Simulations in Chapter 9 predicted a characteristic dimension of 4.89 μm. The manufacturer reported a characteristic dimension of 4.90 μm using the approach developed by Zaretsky et al.[96] If the data from the 0.5 mM KCl solution is discarded since the condition that ΔR_e is independent of ρ is not valid as shown in Table 10-1, the weighted linear regression resulted in a characteristic dimension of 4.88±0.25 μm. The experimental value of the cell constant provided by the manufacturer was 0.0042±0.0001 cm^{-1} which corresponded to a characteristic dimension of 3.55±0.084 μm. If the linear regression of the recorded data was performed without weighting, a character dimension of 3.31±0.21 μm was obtained, which is in agreement with the manufacturer cell constant and characteristic dimension.

Experimental determination of the cell constant or characteristic dimension in conductive media required quantification of $R_{e,eff}$, the extrapolation of the high-frequency effective ohmic resistance using a measurement model, and ΔR_e, the deviation from the true ohmic resistance. A weighted linear regression of the effective ohmic resistance as a function of solution resistivity yielded experimental observation of the characteristic dimension as predicted by simulations. The error weighting was the square inverse of the error of the effective ohmic resistance. Experimental data indicating that ΔR_e is dependent on ρ can also be discarded in experimental determination of the characteristic dimension. Experimentally obtained cell constants without error weighting and ρ-dependent ΔR_e values can result in solution resistivity that is 137±7.7% of the true resistivity.

10.2.3 Deionized Water

Deionized water was measured using an interdigitated electrode (DropSens IDEAU5) and a rotating disk electrode. Due to the solubility of gaseous CO_2 in deionized water,

134
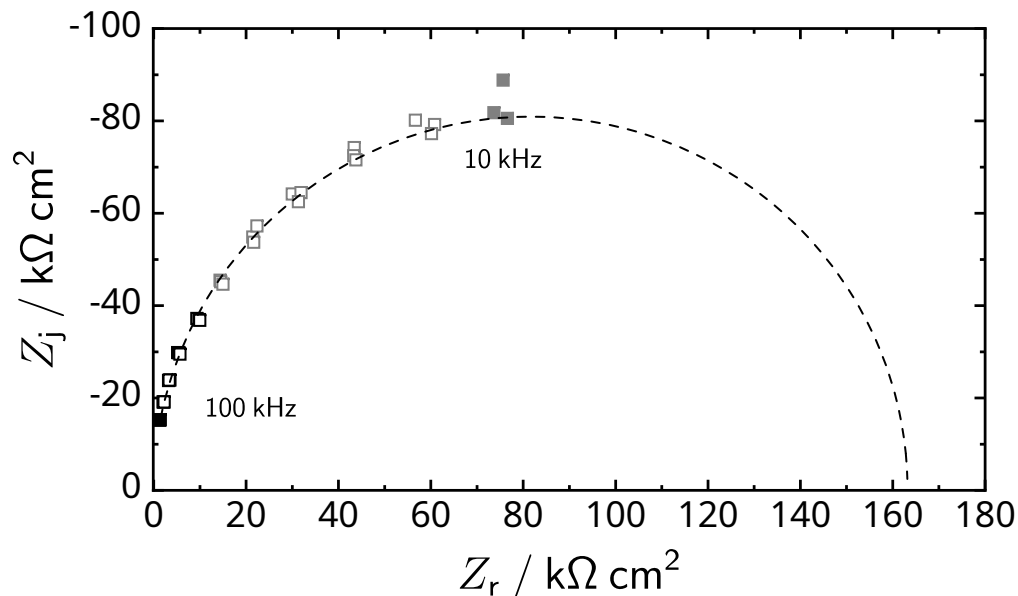
Figure 10-14. Nyquist plot of the impedance of deionized water using a rotating disk electrode rotating at 1000 rpm with perturbation amplitude of 50 mV. The gray data points were not Kramer-Kronig consistent and were not used in regression.

the actual resistivity of the deionized water was assessed through measurements with a rotating disk electrode rotating at 1000 rpm with perturbation of 50 mV over a frequency range of 0.2 Hz to 100 kHz. Linearity was confirmed through observation of Lissajous plots during measurements. The resistance of a disk electrode is given by equation (8-13).[119] The EIS data obtained from the deionized water are shown in Figure 10-14. The resistivity of the deionized water was found to be 1.35 ± 0.016 MΩ cm.

The deionized water used in the rotating disk electrode experiments was then used with an interdigitated electrode over the same frequency range and with a perturbation amplitude of 20 mV. Linearity was confirmed through observation of Lissajous plots during measurements. The average response is shown in Figure 10-15. The regressed value of the ohmic resistance of the water using an IDE was 282 ± 1.1 Ωcm^2 which corresponded to a resistivity of 563 ± 2.3 kΩcm. From simulations with deionized water, the ionic concentration near the surface of the electrode can be several times higher than bulk solution concentration. Simulations presented in Chapter 9 estimated a resistivity of

135
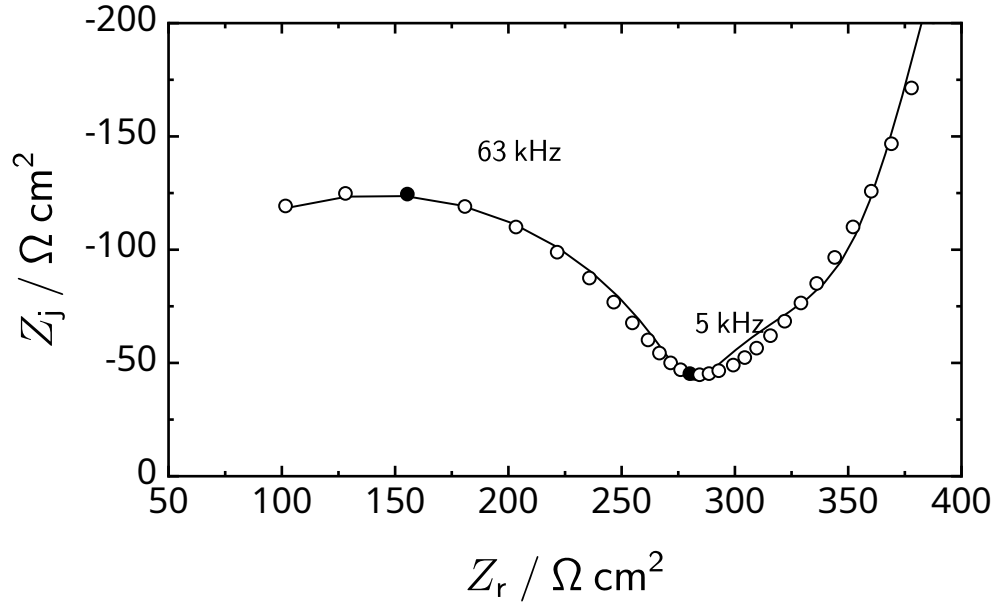
Figure 10-15. Nyquist plot of the impedance response of deionized water using an IDE. The loop on the left corresponds to geometric capacitance. The line is the fit using the circuit model shown in Figure 10-4

.

12.6±0.38 MΩcm due to the influence of the electrical double layer. Without the surface zeta potential of -60 mV, the resistivity of the deionized water was 18.39±0.01 MΩcm. The resistivity obtained from experiments with the RDE was an order of magnitude smaller than that obtained by simulations. The deviation was attributed to higher conductivity of the deionized water due to solubility of atmospheric CO_2. The resistivity obtained using an IDE was 59% less than the resistivity obtained using the RDE. The characteristic dimension of the RDE r_0 was mush larger than that of the IDE. The counterelectrode for the RDE was outside the double layer which resulted in current paths that passed through the resistive electrolyte.

CHAPTER 11
CONCLUSIONS

Fundamental chemical engineering principles were applied to two distinct problems involving electrochemistry. The first work was the design and modeling of an efficient continuous electrokinetic dewatering process. The second was the mathematical modeling and experimental verification of the characteristic dimension of the geometric capacitance of interdigitated electrodes.

11.1   Design of Efficient Continuous Electrokinetic Dewatering

The single-stage design incorporated several design changes that resulted in increased EKD efficiency. The movement of clay through the machine was facilitated by the addition of two conveyor belts. Reversed electrode polarity and the expanded-metal cathode enhanced the removal of water from the dewatered cake. The use of carbon steel as the cathode material was shown to be as effective as the more expensive iridium-oxide-coated titanium.

Rheological experiments of phosphatic clay suspensions yielded the identification of regimes of rheological behavior as functions of solids content. Phosphatic clay with solids content greater than 7.5 wt.% was projected to exhibit viscoelastic-solid behavior due to the ability of the clay fabric to support stress. Pseudoplastic behavior was observed for phosphatic clays with a solids content greater than 29 wt.% and provided a minimum target solids content for the product cake.

A substantial reduction in the total cost is projected with the single-stage design, which is a result of increased throughput at high solids content, cheaper carbon-steel cathodes, and lower power consumption due to reduced electrode area. The proposed design demonstrated an increase of more than an 8-fold in the production rate of a pseudoplastic cake, as compared to previously reported continuous EKD designs. For an assumed capital cost of \$2000/m^2 of electrode, the cost per metric ton of dry clay is projected to be on the order of \$11-12/metric ton of dry-clay, with a solids content of

38 wt.%. The estimated conversion cost of continuous electrokinetic dewatering was a 640% improvement in total cost compared to previous continuous designs.

11.2   Mathematical Modeling of Continuous EKD

The model developed in this work is fundamentally based in soil mechanics, electrokinetic phenomena, and fluid dynamics through porous media. The model accounted for electro-osmotic flow in a porous media. Rheological measurements indicated that the onset of viscoelastic behavior occurred for solids content greater than 7.5 wt.%. An electro-osmotic flow model is shown in the present work to adequately represent the experimental data collected from the operation of the lab-scale continuous EKD prototype with a feed clay of 10 wt.% solids content.

Optimal operating parameters were identified for a industrial-scale continuous EKD process. The simulation results suggested that lower total costs may be achieved with small electrode gaps and reduced residence time. Under the assumption of a maximum electric field of 15 V/cm, the optimal cost of \$9.15/metric ton of dry clay was obtained with a feed-side gap of 8.5 cm, a residence time of 1.3 hours, and a dry-clay production rate of 7.58 kg/hr m^2. The length of electrode for the simulations was fixed at 6.35 m. An estimated total electrode area of 0.17 km^2 was required to process the effluent production rate of the Mosaic Four Corners Mine. The estimated 0.17 km^2 of electrode area represents a 2000% improvement over the 3.5 km^2 area estimated for the two-zone continuous design.[80] The simulated EKD process projected a total cost of \$9/metric ton of dry solids, representing a 820% reduction from the \$74/metric ton for the two-zone prototype.[80]

11.3   Interdigitated Microelectrodes

Finite-element methods were used to simulate the electrochemical impedance response of interdigitated microelectrodes. The characteristic dimension was found to be primarily dependent on the electrode digit width and gap. A minor dependence on the electrode digit height was observed.

The influence of the characteristic dimension was experimentally observed in the measurement of synthetic motor oil, glycerol, and ethylene glycol. The resistivity and dielectric constant of synthetic motor oil obtained from the experiments were in agreement with typical values for lubricating oils. The conductivity of glycerol and ethylene glycol were in the range of published values. The effective dielectric constants were found to be larger than published values, which was shown to be a result of the influence of the glass substrate of the IDEs. Capacitance measurements using IDEs demonstrated that the effective capacitance was always larger than the capacitance of the medium due to the influence of the substrate. In order to obtain accurate measurements of the dielectric of the liquid medium, the dielectric properties of the substrate must known.

Currently, a cell constant is used to calculate electrical properties from impedance data. The cell constant is proportional to the characteristic dimension of the IDE, which was obtained from finite-element simulations. The characteristic dimension was experimentally verified using measurements with KCl solutions. The KCl solution concentrations were sufficiently high such that the geometric capacitances were outside the frequency range for reliable EIS measurements. The characteristic dimension obtained experimentally by EIS measurements was shown to be in agreement with the characteristic dimension obtained from simulations. The demonstrated agreement supports use of a cell constant based solely on the IDE characteristic dimension. Using the IDEs studied in this work, the ohmic resistance cannot be obtained for conductive aqueous solutions because measurements cannot be made at sufficiently high frequencies. An IDE with a 5 nm metal-oxide film was proposed to allow measurement of ohmic resistance of conductive media.

In low-conductivity aqueous electrolytes, the electrical double layer was shown to increase the conductivity near the surface of the electrodes and substrate in simulations and experimentally. The concentration increase was more dramatic in dilute electrolytes with less than 1 mM KCl. In experiments with deionized water, the resistivity using

an IDE was shown to be 58% smaller than the resistivity obtained using an RDE. The disparity was attributed to the influence of the electrical double layer.

CHAPTER 12
FUTURE WORK

The dissertation has shown a significant development of continuous electrokinetic dewatering technologies and developed methods to interpret the impedance response of interdigitated microelectrodes. Continued work is required to bring the technologies to full industrial application. Future work in electrokinetic watering is in expanding the breadth of the process to other suspensions and in improving the mathematical model for design and optimization. The future work with IDEs is increasing the electrochemical interpretation of data in biological sensor applications.

12.1 Continuous Electrokinetic Dewatering on Other Suspensions

Other difficult-to-dewater colloids represent opportunities to expand the breadth of continuous EKD and to advance the method to industrial implementation. Mining processes that use froth floatation generate slow-settling effluent streams that are potential candidates for EKD. Malíková et al.[139] studied the use of flocculants as a dewatering method in dewatering coal mine tailings. Waste management of tailings from lead and zinc mining present similar challenges to those faced by phosphate mining industry. The Lisheen Mine tailings management facility in Ireland stores tailings from lead and zinc mining generated at a rate of 260,000 m^3 annually.[140] Lead and zinc produced in the Stratoni Mines in Greece generate 400,000 metric tons annually of tailings with a solids content between 5 and 14 wt.%.[141] Mechanical dewatering using a geotextile sock produced 65 wt.% cake a cost of $1.2/m^3$ of wet tailings with a residence time of 10 days which corresponds to $288 per m^3/h.[141] The continuous design developed by Dizon and Orazem [93] in dewatering phosphatic clay produced a 35 wt.% cake from a 10 wt.% feed clay at a cost of $1.10 /h m^3 of wet tailings. Tailings of oil sands are also currently dewatered in settling areas. The rate of dewatering oil sands by gravity settling and consolidation decreased sharply once a top crust is formed.[142] The initial sedimentation of the oil sands occurs in a couple of years. The recovered water is recycled into the

141

process and accounts for 87% of the water required for extraction of oil.[143] The balance of oil sands at a solids content of 30 wt.% remains in the settling area for decades.[143] Investigation of continuous EKD on oil sands is important since oil sands are still fluids at a solids content of 40 wt.% and raises the question if continuous EKD is effective at the high solids content required to dewater oil sands. Sewer sludge has been the subject of significant batch electrokinetic dewatering research.[144–146] All the waste streams from sewer sludge, coal, lead, zinc, and oil sands are opportunities for continuous EKD to mitigate the environmental impacts of industry by recovering water and reducing land use in a cost effective way.

Analysis of the properties of the suspended particles in sewer sludge, oil sands, and tailings from coal, lead, and zinc. The electro-osmotic permeability and permeability are dependent on the properties of the particle (i.e. size, shape, tortuosity, and zeta potential) and the fluid (i.e. viscosity, ionic concentrations, and ionic composition).

12.2   Mathematical Modeling of Continuous EKD

Many assumptions were made to develop the current mathematical model for continuous EKD process. The permeabilities were assumed to be constant, as was assumed by Esrig[34]. The model can be improved by the addition of porosity-dependent permeabilities. The clay-fabric structure has been shown to be pH dependent by Peng et al.[73] The pH gradients resulting from the gas evolution reactions will effect the permeability of the porous clay matrix. A time-dependent model will provide insight into the required start-up procedure and process control for an industrial continuous EKD process. The treatment of the electrochemistry in the model can be improved by calculation of the potential distribution and the current resulting from the faradaic reactions. In addition to accounting for the electrochemical reactions, the resistivity of the mixture is dependent on the ionic concentrations, pH, and porosity. Joule heating can be addressed in future models which can aid in power optimization by minimizing thermal

effects. A more thorough treatment of the electrochemistry can improve the accuracy of estimated power requirements of industrial-scale continuous EKD.

The continuous EKD model accounts for electro-osmotic flow and pressure-driven flow. Sedimentation in dilute phosphatic clay suspensions, less than 8 wt.%, require a modified model where particle sedimentation and electrophoretic velocities are taken into account. The current model is limited to phosphatic clay suspensions that range from approximately 8–40 wt.%. Since Joule heating effects are not taken into account, the operating electric fields are limited to less than 20 V/cm. Future continuous EKD models can address the limitations with a more comprehensive model.

12.3   Interdigitiated Microelectrodes

Electrochemical modeling of interdigitated microelectrodes can increase the accuracy of measurements and interpretation, and subsequently increase their usefulness as a biological sensor. Future work is proposed in the modeling in addition to the presentation of preliminary work performed where commercially available IDEs were used as label-less cell sensors.

12.3.1   Applications of Interdigitiated Microelectrodes

Future electrochemical modeling of interdigitated electrodes can be performed with other microelectrode geometries and configurations. Other commercially available interdigitated electrodes have different geometries and configurations such as circular-spiral patterns and the presence of a micro-reference electrode. Finite-element models of other geometries can show advantages and disadvantages of the designs and application limitations. The accuracy of the finite-element simulations can be increased by accounting for the serpentine structure and by using a refined meshing scheme. The development of a high-conductivity variant proposed in this work can be the subject for fabrication and experimental validation. Further work can be conducted on the effect of IDE substrate. A more thorough treatment of the electrical double layer can be performed to improve the interpretation of data collected using interdigitated microelectrodes. The present
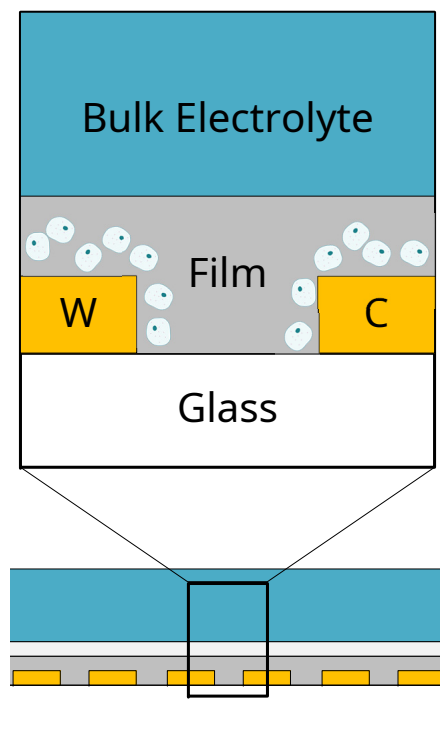
Figure 12-1. A schematic representation of cell cultures on an IDE.

work did not account for the oscillating concentrations near the electrodes during EIS simulations. The proposed future work has applicability in data interpretation and design of interdigitated microelectrodes.

12.3.2 Label-less Biological Detection

The advantage of IDEs are increased sensitivity with small sample sizes, which has led to their use in biological applications. Cells can be grown on thiol-functionalized gold IDEs.[117] Cell growth correlated to impedance is a proposed method of label-less biological detection. Functionalization promotes cellular adhesion and immobilization on the gold electrodes as depicted in Figure 12-1. Cells from the 3T3 cell line were grown on the IDE in a medium consisting of Dulbecco's Modified Eagle's Medium high glucose, bovine serum, and antibiotics (Penstrap). The proposed circuit diagram in Figure 12-2 represented the expected impedance response where the interfacial impedance was due to the influence of the electrical double layer, the film impedance was the effect of

Proposed Model   **Regression Model**
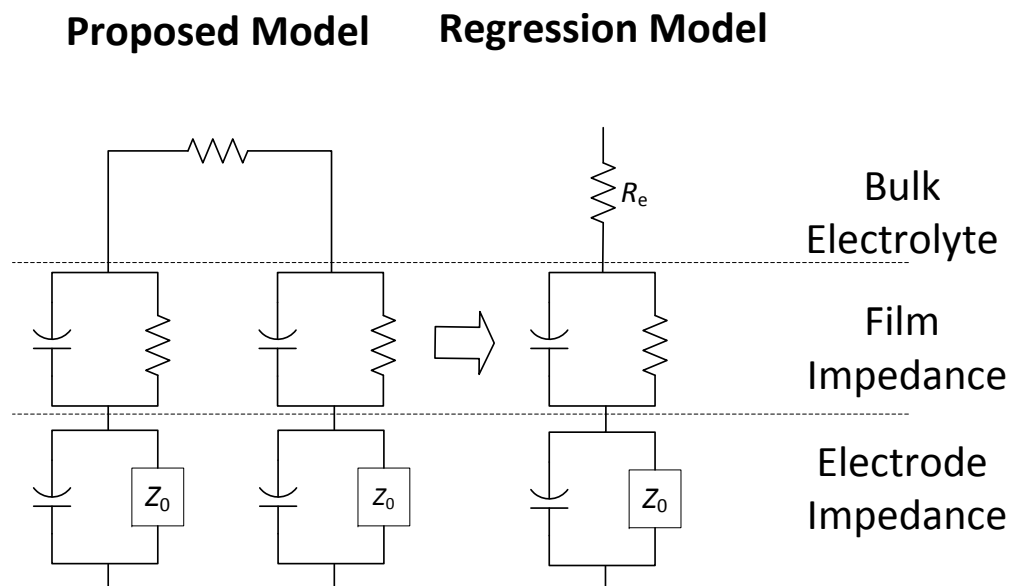
Figure 12-2. Circuit diagram representing the impedance of cell cultures on IDEs.

cellular adhesion to the gold, and the ohmic resistance was due to the bulk electrolytic media. Three biological samples were prepared on IDEs. A control sample was with the media only. Cells and media were incubated on the second IDE. Cells with media and fibronectin were incubated on the third IDE. The control and cells samples were measured with a 20 mV perturbation. The cells with fibronectin sample required a higher perturbation amplitude of 50 mV. Fibronectin in a protein that promotes cellular adhesion. Linearity at the perturbations was confirmed for all samples by monitoring of the Lissajous plot during measurements. The measured frequency range was 100 kHz to 0.2 Hz. The experimental setup was identical to the experimental setup described for organic liquids and depicted in Figure 10-1. The impedance data was shown to be consistent with the Kramer-Kronig relations using a measurement model and is shown in Figure 12-3. The cells and fibronectin sample showed an RC behavior corresponding to the film impedance. Figure 12-4 is an enlarged image of the high-frequency impedance and suggests the presence of a film. The geometric capacitance was not apparent in the

Figure 12-3. Nyquist plot of the experimental impedance response of interdigitated electrodes with media, cells, and cells and fibronectin. Control was with the media only. Cell was with the presence of cells on the electrode. Cells and fibronectin sample was with enhanced cellular adhesion through the use of fibronectin.

measured frequency range. The process model used for regression was

$$Z = R_{\mathrm{e}} + \frac{Z_{\mathrm{film}}}{1 + (j\omega)^{\alpha_{\mathrm{film}}} R_{\mathrm{film}} Q_{\mathrm{film}}} + \frac{Z_0}{1 + (j\omega)^{\alpha_0} Z_0 C_{\mathrm{dl}}} \qquad (12\text{-}1)$$

where the ohmic resistance is represented by R_{e}, the film is represented by the first RCPE term, and the interfacial impedance is represented by the second RCPE. The ohmic resistance was small compared to the film and interfacial impedance. The effective film capacitance was obtained by equation (9-19). The film resistance was the smallest for the control with a regressed value of 11.2 kΩcm². The increase in the magnitude of the film impedance suggested that cell adhesion occurred and blocked electrode area from passing current. The film resistance for the cells sample was found to be 14.1 kΩcm². The film resistance of the cell and fibronectin was found to be 1.56 MΩcm². The large RCPE loop of the cells and fibronectin sample suggested that cell adhesion increased due to the increase in impedance. The regressed capacitance of the film was 0.87±0.046 nF/cm² for
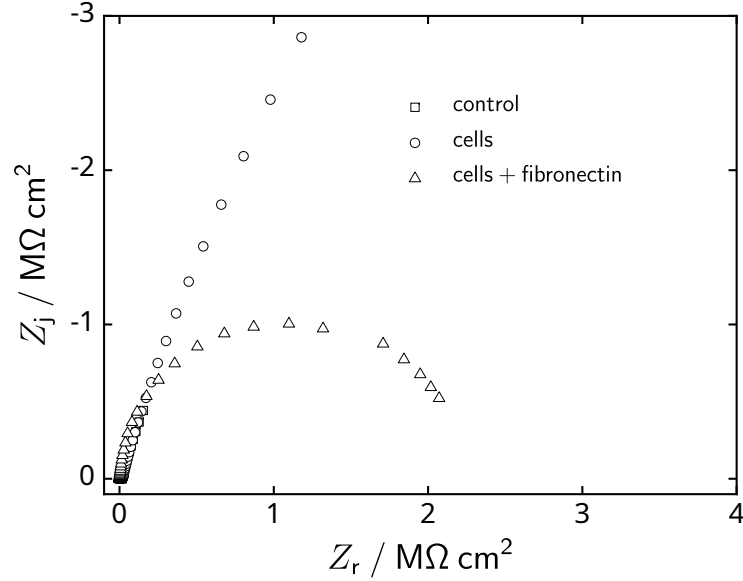
146
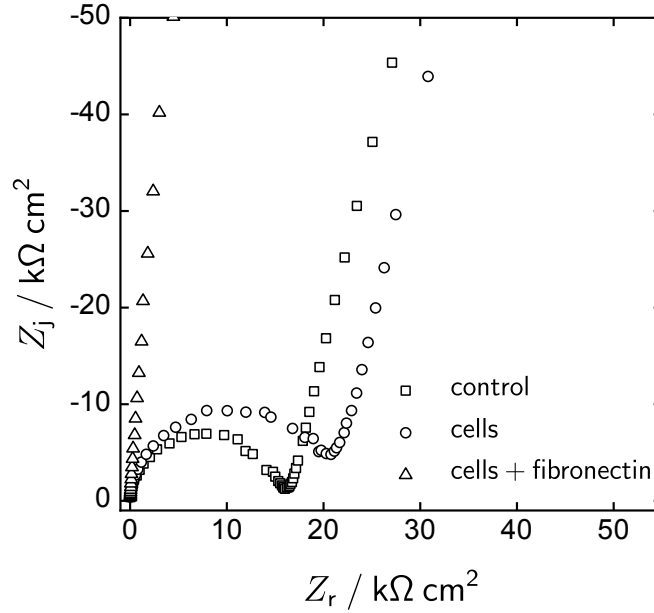
Figure 12-4. Magnified Nyquist plot of the experimental high-frequency impedance responses of interdigitated electrodes with media, cells, and cells and Fibronectin. Control was with the media only. Cell was with the presence of cells on the electrode. Cells and fibronectin sample was with cells adhesion enhanced with the use of fibronectin.

the control, 0.91±0.054 nF/cm^2 for the cell sample, and 10.11±0.008 nF/cm^2 for the cells and fibronectin sample. The exposed surface area of the bare electrode can be estimated by

$$\gamma = \frac{C_{\text{bare}}}{C_{\text{film}}} \tag{12-2}$$

The cells and fibronectin sample had an estimated bare-electrode surface area of 86%, which corresponded to a cell coverage of 14%. Optical microscopy of the electrode surface can be used to verify the electrode surface coverage by cultivate cells in future work.

REFERENCES

[1] R. Kong, Continuous electrokinetic dewatering of phosphatic clay suspensions, Ph.D. thesis, University of Florida, Gainesville, FL (May 2015).

[2] U. S. Geological Survey, Phosphate rock, in: Mineral Commodity Summaries, U.S. Geological Survey, 2017, pp. 124–125.

[3] N. Gilbert, Environment: The disappearing nutrient, Nature News 461 (7265) (2009) 716–718.

[4] U. S. Geological Survey, Phosphate rock, in: Mineral Commodity Summaries, U.S. Geological Survey, 1996, pp. 122–123.

[5] U. S. Geological Survey, Phosphate rock, in: Mineral Commodity Summaries, U.S. Geological Survey, 1997, pp. 124–125.

[6] U. S. Geological Survey, Phosphate rock, in: Mineral Commodity Summaries, U.S. Geological Survey, 1998, pp. 124–125.

[7] U. S. Geological Survey, Phosphate rock, in: Mineral Commodity Summaries, U.S. Geological Survey, 1999, pp. 126–127.

[8] U. S. Geological Survey, Phosphate rock, in: Mineral Commodity Summaries, U.S. Geological Survey, 2000, pp. 124–125.

[9] U. S. Geological Survey, Phosphate rock, in: Mineral Commodity Summaries, U.S. Geological Survey, 2001, pp. 120–121.

[10] U. S. Geological Survey, Phosphate rock, in: Mineral Commodity Summaries, U.S. Geological Survey, 2002, pp. 122–123.

[11] U. S. Geological Survey, Phosphate rock, in: Mineral Commodity Summaries, U.S. Geological Survey, 2003, pp. 124–125.

[12] U. S. Geological Survey, Phosphate rock, in: Mineral Commodity Summaries, U.S. Geological Survey, 2004, pp. 122–123.

[13] U. S. Geological Survey, Phosphate rock, in: Mineral Commodity Summaries, U.S. Geological Survey, 2005, pp. 122–123.

[14] U. S. Geological Survey, Phosphate rock, in: Mineral Commodity Summaries, U.S. Geological Survey, 2006, pp. 124–125.

[15] U. S. Geological Survey, Phosphate rock, in: Mineral Commodity Summaries, U.S. Geological Survey, 2007, pp. 120–121.

[16] U. S. Geological Survey, Phosphate rock, in: Mineral Commodity Summaries, U.S. Geological Survey, 2008, pp. 124–125.

[17] U. S. Geological Survey, Phosphate rock, in: Mineral Commodity Summaries, U.S. Geological Survey, 2009, pp. 120–121.

[18] U. S. Geological Survey, Phosphate rock, in: Mineral Commodity Summaries, U.S. Geological Survey, 2010, pp. 118–119.

[19] U. S. Geological Survey, Phosphate rock, in: Mineral Commodity Summaries, U.S. Geological Survey, 2011, pp. 118–119.

[20] U. S. Geological Survey, Phosphate rock, in: Mineral Commodity Summaries, U.S. Geological Survey, 2012, pp. 118–119.

[21] U. S. Geological Survey, Phosphate rock, in: Mineral Commodity Summaries, U.S. Geological Survey, 2013, pp. 118–119.

[22] U. S. Geological Survey, Phosphate rock, in: Mineral Commodity Summaries, U.S. Geological Survey, 2014, pp. 118–119.

[23] U. S. Geological Survey, Phosphate rock, in: Mineral Commodity Summaries, U.S. Geological Survey, 2015, pp. 118–119.

[24] U. S. Geological Survey, Phosphate rock, in: Mineral Commodity Summaries, U.S. Geological Survey, 2016, pp. 124–125.

[25] U. S. Geological Survey, Phosphate rock, Minerals Yearbook. U.S. Geological Survey (2011) 56.1–56.11.

[26] M. T. Brown, Landscape restoration following phosphate mining: 30 years of co-evolution of science, industry and regulation, Ecological Engineering 24 (4) (2005) 309–329.

[27] C. Barnett, Mine field, Florida Trend: The Magazine of Florida Business (2008) 84–90.

[28] S. J. Van Kauwenbergh, J. B. Cathcart, G. H. McClellan, Mineralogy and Alteration of the Phosphate Deposits of Florida, U.S. Geological Survey, Denver, 1990.

[29] M. Wilson, E. A. Hanlon, Florida reclaimed phosphate mine soils: Characteristics, potential uses, and management considerations, Tech. Rep. SL370, Soil and Water Science Department, Florida Cooperative Extension Service, Institute of Food and Agricultural Sciences, University of Florida. (2012).

[30] B. M. Moudgil, Enhanced recovery of coarse particles during phosphate flotation, Tech. rep., Florida Institute of Phosphate Research (1992).

[31] P. M. Tyler, W. M. H. Waggaman, Phosphatic slime, Industrial and Engineering Chemistry 46 (5) (1954) 1049–1056.

[32] K. Terzaghi, Erdbaumechanik auf bodenphysikalischer Grundlage, Franz Deuticke, Leipzig, 1925.

[33] M. E. Orazem, Theoretical analysis of solid-liquiid separation by expression, Qualifying exam, University of California, Berkeley, Berkeley, CA (1979).

[34] M. I. Esrig, Pore pressures, consolidation, and electrokinetics, Journal of the Soil Mechanics and Foundations Division 94 (4) (1968) 899–921.

[35] J. T. G. Overbeek, Thermodynamics of electrokinetic phenomena, Journal of Colloid Science 8 (4) (1953) 420–427.

[36] T. Tripathy, B. R. De, Flocculation : A new way to treat the waste water, Journal of Physical Sciences 10 (2006) 93–127.

[37] M. K. Abd-El Rahman, Dewatering of phosphatic clay waste by flocculation, Chemical Engineering & Technology 23 (5) (2000) 457–461.

[38] L. Lu, Z. Pan, N. Hao, W. Peng, A novel acrylamide-free flocculant and its application for sludge dewatering, Water Research 57 (0) (2014) 304–312.

[39] M. J. Pearse, S. Weir, S. J. Adkins, G. M. Moody, Advances in mineral flocculation, Minerals Engineering 14 (11) (2001) 1505–1511.

[40] J. Vaxelaire, P. Cézac, Moisture distribution in activated sludges: A review, Water Research 38 (9) (2004) 2215–2230.

[41] United States Environmental Protection Agency, Biosolids technology fact sheet belt filter press, Tech. Rep. EPA 832-F-00-057, United States Environmental Protection Agency (2000).

[42] J. T. Novak, Dewatering of sewage sludge, Drying Technology 24 (2006) 1257–1262.

[43] United States Environmental Protection Agency, Biosolids technology fact sheet centrifuge thickening and dewatering, Tech. Rep. EPA 832-F-00-053, United States Environmental Protection Agency (2000).

[44] H. G. Snyman, P. Forssman, A. Kafaar, M. Smollen, The feasibility of electro-osmotic belt filter dewatering technology at pilot scale, Water Science & Technology 41 (2000) 137–144.

[45] B. Peeters, Mechanical dewatering and thermal drying of sludge in a single apparatus, Drying Technology 28 (4) (2010) 454–459.

[46] A. Mahmoud, J. Olivier, J. Vaxelaire, A. F. A. Hoadley, Electro-dewatering of wastewater sludge: Influence of the operating conditions and their interactions effects, Water Research 45 (9) (2011) 2795–2810.

[47] F. F. Reuss, Notice sur un nouvel effet de l'Électricité galvanique, Mémoires de la Société Impériale des Naturalistes de Moscou 2 (1809) 327–337.

[48] W. Horwitz, The theory of electrokinetic phenomena, Journal of Chemical Education 16 (11) (1939) 519–535.

[49] S. Speil, M. R. Thompson, Electrophoretic dewatering of clay, Journal of The Electrochemical Society 81 (1942) 119–145.

[50] D.-H. Kim, B.-G. Ryu, S.-W. Park, C.-I. Seo, K. Baek, Electrokinetic remediation of Zn and Ni-contaminated soil, Journal of Hazardous Materials 165 (1) (2009) 501–505.

[51] P. R. Buchireddy, R. M. Bricka, D. B. Gent, Electrokinetic remediation of wood preservative contaminated soil containing copper, chromium, and arsenic, Journal of Hazardous Materials 162 (1) (2009) 490–497.

[52] K. Baek, D. Kim, S. Park, B. Ryu, T. Bajargal, J. Yang, Electrolyte conditioning-enhanced electrokinetic remediation of arsenic-contaminated mine tailing, Journal of Hazardous Materials 161 (1) (2009) 457–462.

[53] X. Mao, J. Wang, A. Ciblak, E. E. Cox, C. Riis, M. Terkelsen, D. B. Gent, A. N. Alshawabkeh, Electrokinetic-enhanced bioaugmentation for remediation of chlorinated solvents contaminated clay, Journal of Hazardous Materials 213 (2012) 311–317.

[54] Y. Guo, J. Q. Shang, A study on electrokinetic dewatering of oil sands tailings, Environmental Geotechnics 1 (2014) 121–134.

[55] S. Bourgès-Gastaud, G. Stoltz, P. Dolez, E. Blond, N. Touze-Foltz, A laboratory device to characterize electrokinetic geocomposites for fluid fine tailings dewatering, Canadian Geotechnical Journal 52 (4).

[56] J. Lamont-Black, C. J. F. P. Jones, S. Glendinning, D. T. Huntley, A. B. Fourie, Laboratory evaluation of the potential for electrokinetic belt filter press dewatering of kimberlite slimes, in: Paste, 2007, pp. 147–152.

[57] O. Bayat, O. Kilic, B. Bayat, M. Anil, H. Akarsu, C. Poole, Electrokinetic dewatering of turkish glass sand plant tailings, Water Research 40 (1) (2006) 61–66.

[58] A. B. Fourie, D. G. Johns, C. J. F. P. Jones, Dewatering of mine tailings using electrokinetic geosynthetics, Canadian Geotechnical Journal 44 (2007) 160–172.

[59] J. Q. Shang, E. Mohamedelhassan, Electrokinetic dewatering of Eneabba West Mine tailings: A laboratory experimental study, in: Soft Ground Technology, American Society of Civil Engineers, 2001, Ch. 26, pp. 346–357.

[60] T. J. Johnson, E. J. Davis, Experimental data and theoretical predictions for the rate of electrophoretic clarification of colloidal suspensions, Environmental Science & Technology 34 (9) (2000) 1806–1812.

[61] T. J. Johnson, E. J. Davis, An analysis of electrophoresis of concentrated suspensions of colloidal particles, Journal of Colloid and Interface Science 215 (2) (1999) 397–408.

[62] J. Q. Shang, Electrokinetic sedimentation: A theoretical and experimental study, Canadian Geotechnical Journal 34 (2) (1997) 305–314.

[63] J. Q. Shang, Electokinetic dewatering of clay slurries as engineered soil covers, Canadian Geotechnical Journal 34 (1) (1997) 78–86.

[64] J. Q. Shang, K. Y. Lo, Electrokinetic dewatering of a phosphate clay, Journal of Hazardous Materials 55 (1997) 117–133.

[65] S. Glendinning, J. Lamont-Black, C. J. F. P. Jones, Treatment of sewage sludge using electrokinetic geosynthetics, Journal of Hazardous Materials 139 (3) (2007) 491–499.

[66] M. Y. Ho, G. Chen, Enhanced electro-osmotic dewatering of fine particle suspension using a rotating anode, Industrial & Engineering Chemistry Research 40 (8) (2001) 1859–1863.

[67] S. Hwang, K.-S. Min, Improved sludge dewatering by addition of electro-osmosis to belt filter press, Journal of Environmental Engineering and Science 2 (2) (2003) 149–153.

[68] M. H. M. Raats, A. J. G. van Diemen, J. Lavén, H. N. Stein, Full scale electrokinetic dewatering of waste sludge, Colloids and Surfaces A: Physicochemical and Engineering Aspects 210 (2–3) (2002) 231–241.

[69] C. J. F. P. Jones, J. Lamont-Black, S. Glendinning, Electrokinetic geosynthetics in hydraulic applications, Geotextiles and Geomembranes 29 (4) (2011) 381–390.

[70] A. Fourie, Harnessing the power: Opportunities for electrokinetic dewatering of mine tailings, Geotechnical News June (2006) 27–32.

[71] P. A. Vesilind, The role of water in sludge dewatering, Water Environment Research 66 (1) (1994) 4–11.

[72] J. C. Santamarina, K. A. Klein, Y. H. Wang, E. Prencke, Specific surface: Determination and relevance, Canadian Geotechnical Journal 39 (1) (2002) 233–241.

[73] C. Peng, H. Lai, M. E. Orazem, S. Moghaddam, Microstructure of clay fabric in electrokinetic dewatering of phosphatic clay dispersions, Applied Clay Science 158 (2018) 94–101.

[74] N. Pashias, D. Boger, J. Summers, D. Glenister, A 50 cent rheometer for yield stress measurement, Journal of Rheology 40 (6) (1996) 1179–1189.

[75] J. P. McKinney, M. E. Orazem, A constitutive relationship for electrokinetic dewatering of phosphatic clay slurries, Minerals & Metallurgical Processing 28 (2011) 49–54.

[76] R. Kong, M. E. Orazem, Semi-continuous electrokinetic dewatering of phosphatic clay suspensions, Electrochimica Acta 140 (2014) 438–446.

[77] J. Q. Shang, Electokinetic dewatering of clay slurries as engineered soil covers, Canadian Geotechnical Journal 34 (1) (1997) 78–86.

[78] J. P. McKinney, Design of electrolytic dewatering systems for phosphatic clay suspensions, Ph.D. thesis, University of Florida (2010).

[79] R. Kong, A. Dizon, S. Moghaddam, M. E. Orazem, Development of Fully-Continuous Electrokinetic Dewatering of Phosphatic Clay Suspensions, Vol. XVIII of Advances in Electrochemical Science and Engineering, John Wiley & Sons, Hoboken, 2018.

[80] R. Kong, A. Dizon, S. Moghaddam, M. E. Orazem, Development of fully-continuous electrokinetic dewatering of phosphatic clay suspensions, in: R. Alkire (Ed.), Electrochemical Engineering: The Path from Discovery to Product, Vol. XVIII of Advances in Electrochemical Science and Engineering, John Wiley & Sons, Hoboken, 2018, in press.

[81] L. Graetz, Handbuch der Elektrizität und des Magnetismus, Vol. 4, J. A. Barth, Leipzig, 1920.

[82] J. S. Newman, K. E. Thomas-Alyea, Electrochemical Systems, 3rd Edition, John Wiley & Sons, Hoboken, 2004.

[83] I. L. Casagrande, Electro-osmosis in soils, Géotechnique 1 (3) (1949) 159–177.

[84] J. Q. Shang, Electroosmosis-enhanced preloading consolidation via vertical drains, Canadian Geotechnical Journal 35 (3) (1998) 491–499.

[85] L. Hu, W. Wu, H. Wu, Numerical model of electro-osmotic consolidation in clay, Géotechnique 62 (6) (2012) 537.

[86] J. Yuan, M. A. Hicks, Large deformation elastic electro-osmosis consolidation of clays, Computers and Geotechnics 54 (2013) 60–68.

[87] L. Hu, H. Wu, Mathematical model of electro-osmotic consolidation for soft ground improvement, Géotechnique 64 (2013) 155–164.

[88] J. Q. Shang, Zeta potential and electroosmotic permeability of clay soils, Canadian Geotechnical Journal 34 (4) (1997) 627–631.

[89] E. Mohamedelhassan, J. Shang, Feasibility assessment of electro-osmotic consolidation on marine sediment, Ground Improvement 6 (4) (2002) 145–152.

[90] K. K. R. Kambham, K. Tuncay, M. Y. Corapcioglu, A semianalytical analysis of compressible electrophoretic cake formation, Water Resources Research 31 (5) (1995) 1421–1428.

[91] J. P. McKinney, M. E. Orazem, A constitutive relationship for electrokinetic dewatering of phosphatic clay slurries, Minerals & Metallurgical Processing 28 (2011) 49–54.

[92] J. P. McKinney, M. E. Orazem, Electrokinetic dewatering of phosphatic clay settling areas: Numerical simulation and economic assessment, Minerals & Metallurgical Processing 28 (2011) 71–76.

[93] A. Dizon, M. E. Orazem, Efficient single-stage electrokinetic dewatering of phosphatic clay suspensions, In preparation.

[94] J. Knappett, R. F. Craig, Soil Mechanics, CRC Press, Boca Raton, 2013.

[95] M. E. Orazem, B. Tribollet, Electrochemical Impedance Spectroscopy, 2nd Edition, John Wiley & Sons, Hoboken, 2017.

[96] M. C. Zaretsky, L. Mouayad, J. R. Melcher, Continuum properties from interdigital electrode dielectrometry, IEEE Transactions on Electrical Insulation 23 (6) (1988) 897–917.

[97] C. E. Chidsey, B. Feldman, C. Lundgren, R. W. Murray, Micrometer-spaced platinum interdigitated array electrode: fabrication, theory, and initial use, Analytical Chemistry 58 (3) (1986) 601–607.

[98] Z. Zou, J. Kai, M. J. Rust, J. Han, C. H. Ahn, Functionalized nano interdigitated electrodes arrays on polymer with integrated microfluidics for direct bio-affinity sensing using impedimetric measurement, Sensors and Actuators A: Physical 136 (2) (2007) 518 – 526.

[99] L. Skjolding, C. Spegel, A. Ribayrol, J. Emnéus, L. Montelius, Characterisation of nano-interdigitated electrodes, in: Journal of Physics: Conference Series, Vol. 100, IOP Publishing, 2008, p. 052045.

[100] U. Pliquett, D. Frense, M. Schönfeldt, C. Frätzer, Y. Zhang, B. Cahill, M. Metzen, A. Barthel, T. Nacke, D. Beckmann, Testing miniaturized electrodes for impedance measurements within the beta-dispersion–a practical approach, Journal of Electrical Bioimpedance 1 (1) (2010) 41–55.

[101] M. Ibrahim, J. Claudel, D. Kourtiche, M. Nadi, Geometric parameters optimization of planar interdigitated electrodes for bioimpedance spectroscopy, Journal of Electrical Bioimpedance 4 (1) (2013) 13–22.

[102] D.-Y. Jeon, S. Jeong Park, Y. Kim, M.-J. Shin, P. Soo Kang, G.-T. Kim, Impedance characterization of nanogap interdigitated electrode arrays fabricated by tilted angle evaporation for electrochemical biosensor applications, Journal of Vacuum Science & Technology B 32 (2) (2014) 021803.

[103] J. Hong, D. S. Yoon, S. K. Kim, T. S. Kim, S. Kim, E. Y. Pak, K. No, AC frequency characteristics of coplanar impedance sensors as design parameters, Lab on a Chip 5 (3) (2005) 270–279.

[104] Z. Chen, A. Sepulveda, M. Ediger, R. Richert, Dielectric spectroscopy of thin films by dual channel impedance measurements on differential interdigitated electrode arrays, European Physical Journal B 85 (8).

[105] P. Tomčík, Microelectrode arrays with overlapped diffusion layers as electroanalytical detectors: theory and basic applications, Sensors 13 (10) (2013) 13659–13684.

[106] S. O. Blume, R. Ben-Mrad, P. E. Sullivan, Modelling the capacitance of multi-layer conductor-facing interdigitated electrode structures, Sensors and Actuators B: Chemical 213 (2015) 423–433.

[107] S. MacKay, P. Hermansen, D. Wishart, J. Chen, Simulations of interdigitated electrode interactions with gold nanoparticles for impedance-based biosensing applications, Sensors 15 (9) (2015) 22192–22208.

[108] L. Bueno, T. R. L. C. Paixão, A copper interdigitated electrode and chemometrical tools used for the discrimination of the adulteration of ethanol fuel with water, Talanta 87 (2011) 210–215.

[109] J. Staginus, Polydimethylsiloxane-coated interdigitated electrodes for capacitive detection of organic pollutants in water: A systematic guide, Ph.D. thesis, Delft University of Technology (2015).

[110] F. Mohamad, M. A. Sairin, N. N. A. Nizar, S. A. Aziz, D. M. Hashim, S. Misbahulmunir, F. Z. Rokhani, Investigation on interdigitated electrode design for impedance spectroscopy technique targeting lard detection application, in: 9th International Conference on Sensing Technology, Piscataway, 2015, pp. 739–744.

[111] V. Matylitskaya, S.Kasemann, G. Urban, C. Dincer, S. Partel, Electrochemical characterization of nanogap interdigitated electrode arrays for lab-on-a-chip applications, Journal of The Electrochemical Society 165 (3) (2018) B127–B134.

[112] L. Yang, Y. Li, G. F. Erf, Interdigitated array microelectrode-based electrochemical impedance immunosensor for detection of escherichia coli O157:H7, Analytical Chemistry 76 (4) (2004) 1107–1113.

[113] R. Maalouf, C. Fournier-Wirth, J. Coste, H. Chebib, Y. Saïkali, O. Vittori, A. Errachid, J.-P. Cloarec, C. Martelet, N. Jaffrezic-Renault, Label-free detection of bacteria by electrochemical impedance spectroscopy: comparison to surface plasmon resonance, Analytical Chemistry 79 (13) (2007) 4879–4886.

[114] X. Guo, A. Kulkarni, A. Doepke, H. B. Halsall, S. Iyer, W. R. Heineman, Carbohydrate-based label-free detection of escherichia coli ORN 178 using

electrochemical impedance spectroscopy, Analytical Chemistry 84 (1) (2011) 241–246.

[115] M. Labib, A. S. Zamay, O. S. Kolovskaya, I. T. Reshetneva, G. S. Zamay, R. J. Kibbee, S. A. Sattar, T. N. Zamay, M. V. Berezovski, Aptamer-based viability impedimetric sensor for bacteria, Analytical Chemistry 84 (21) (2012) 8966–8969.

[116] C. Hu, D.-P. Yang, Z. Wang, L. Yu, J. Zhang, N. Jia, Improved EIS performance of an electrochemical cytosensor using three-dimensional architecture Au@BSA as sensing layer, Analytical Chemistry 85 (10) (2013) 5200–5206.

[117] L. Han, P. Liu, V. A. Petrenko, A. Liu, A label-free electrochemical impedance cytosensor based on specific peptide-fused phage selected from landscape phage library, Scientific Reports 6 (2016) 22199.

[118] S. Shibata, Thermal atomic layer deposition of lithium phosphorus oxynitride as a thin-film solid electrolyte, Journal of The Electrochemical Society 163 (13) (2016) A2555–A2562.

[119] J. S. Newman, Resistance for flow of current to a disk, Journal of the Electrochemical Society 113 (5) (1966) 501–502.

[120] H. Fricke, The theory of electrolytic polarization, Philosophical Magazine 14 (1932) 310–318.

[121] C. L. Alexander, B. Tribollet, M. E. Orazem, Contribution of surface distributions to constant-phase-element (CPE) behavior: 1. influence of roughness, Electrochimica Acta 173 (2015) 416–424.

[122] C. L. Alexander, B. Tribollet, M. E. Orazem, Contribution of surface distributions to constant-phase-element (CPE) behavior: 3. adsorbed intermediate, Electrochimica Acta 251 (2017) 99–108.

[123] C. L. Alexander, B. Tribollet, M. E. Orazem, Contribution of surface distributions to constant-phase-element (CPE) behavior: 2. capacitance, Electrochimica Acta 188 (2016) 566–573.

[124] M. E. Orazem, B. Tribollet, V. Vivier, D. P. Riemer, E. A. White, A. L. Bunge, On the use of the power-law model for interpreting constant-phase-element parameters, Journal of the Brazilian Chemical Society 25 (2014) 532–539.

[125] M. Musiani, M. E. Orazem, N. Pébère, B. Tribollet, V. Vivier, Constant-phase-element behavior caused by coupled resistivity and permittivity distributions in films, Journal of the Electrochemical Society 158 (2011) C424–C428.

[126] B. Hirschorn, M. E. Orazem, B. Tribollet, V. Vivier, I. Frateur, M. Musiani, Constant-phase-element behavior caused by resistivity distributions in films: 1. Theory, Journal of the Electrochemical Society 157 (2010) C452–C457.

[127] B. Hirschorn, M. E. Orazem, B. Tribollet, V. Vivier, I. Frateur, M. Musiani, Constant-phase-element behavior caused by resistivity distributions in films: 2. Applications, Journal of the Electrochemical Society 157 (2010) C458–C463.

[128] B. Hirschorn, M. E. Orazem, B. Tribollet, V. Vivier, I. Frateur, M. Musiani, Constant-phase-element behavior caused by resistivity distributions in films, ECS Transactions 28 (24) (2010) 77–94.

[129] P. Agarwal, M. E. Orazem, L. H. García-Rubio, Measurement models for electrochemical impedance spectroscopy: 1. Demonstration of applicability, Journal of the Electrochemical Society 139 (1992) 1917–1927.

[130] G. J. Brug, A. L. G. van den Eeden, M. Sluyters-Rehbach, J. H. Sluyters, The analysis of electrode impedances complicated by the presence of a constant phase element, Journal of Electroanalytical Chemistry 176 (1984) 275–295.

[131] W. J. Choi, J. Jung, S. Lee, Y. J. Chung, C. Yang, Y. K. Lee, Y. Lee, J. K. Park, H. W. Ko, J. Lee, Effects of substrate conductivity on cell morphogenesis and proliferation using tailored, atomic layer deposition-grown ZnO thin films, Scientific Reports 5 (2015) 9974.

[132] D. L. Raimondi, E. Kay, High resistivity transparent ZnO thin films, Journal of Vacuum Science and Technology 7 (1) (1970) 96–99.

[133] N. H. Langton, D. Matthews, The dielectric constant of zinc oxide over a range of frequencies, British Journal of Applied Physics 9 (11) (1958) 453.

[134] A. A. Carey, The dielectric constant of lubrication oils, Tech. rep., Computational Systems Inc. Knoxville, TN (1998).

[135] W. M. Haynes, CRC Handbook of Chemistry and Physics, 98th Edition, Taylor & Francis, Boca Raton, 2018.

[136] Glycerine Producers' Association, Physical Properties of Glycerine and Its Solutions, Glycerine Producers' Association, New York, 1963.

[137] E. Jungermann, N. O. V. Sonntag, Glycerine: A Key Cosmetic Ingredient, Marcel Dekker Inc., New York, 1991.

[138] R. De La Rica, C. Fernández-Sánchez, A. Baldi, Polysilicon interdigitated electrodes as impedimetric sensors, Electrochemistry Communications 8 (8) (2006) 1239–1244.

[139] P. Malíková, J. Thomas, J. Chromíková, J. Vidlář, J. Kupka, Innovation in dewatering process of flotation tailings by study of particle interaction in colloidal environment, Perspectives in Science 7 (2016) 171–177.

[140] M. Dillon, R. White, D. Power, Tailings storage at Lisheen Mine, Ireland, Minerals Engineering 17 (2) (2004) 123–130.

[141] P. Newman, M. Hodgson, E. Rosselot, The disposal of tailings and minewater sludge using geotextile dewatering techniques, Minerals Engineering 17 (2) (2004) 115–121.

[142] M. J. Silva, M. A. Naeth, K. W. Biggar, D. S. Chanasyk, D. C. Sego, Plant selection for dewatering and reclamation of tailings, Tech. rep., American Society for Surface Mining and Reclamation (1998).

[143] M. Gray, Z. Xu, J. Masliyah, Physics in the oil sands of Alberta, Physics Today 62 (3) (2009) 31–35.

[144] M. Citeau, O. Larue, E. Vorobiev, Influence of salt, pH and polyelectrolyte on the pressure electro-dewatering of sewage sludge, Water Research 45 (6) (2011) 2167 – 2180.

[145] J. Conrardy, J. Vaxelaire, J. Olivier, Electro-dewatering of activated sludge: electrical resistance analysis, Water Research 100 (2016) 194–200.

[146] A. Mahmoud, A. F. Hoadley, M. Citeau, J. M. Sorbet, G. Olivier, J. Vaxelaire, J. Olivier, A comparative study of electro-dewatering process performance for activated and digested wastewater sludge, Water Research 129 (2018) 66 – 82.

BIOGRAPHICAL SKETCH

Arthur Dizon graduated with bachelor's degree in chemical engineering from the University of Florida in 2004. He started his career at Anheuser-Busch Inc. and eventually rose to the position of Quality Assurance Manager at Bacardi Bottling Corporation before returning to the University of Florida to continue his education. Arthur was the founding chair of the chemical engineering graduate safety council, served as president of the Graduate Association of Chemical Engineers, and served as the chair for the for the student chapter of the Electrochemical Society. Arthur received his doctoral degree in chemical engineering in 2018, working under the direction of Distinguished Professor Mark E. Orazem. The focus of his work included application of electrokinetic dewatering to phosphatic clay suspensions, mathematical modeling, and electrochemical impedance spectroscopy.